

Contribution of Candidate

Accretion Processes in AM Herculis Systems

by

Lilia Ferrario

Mount Stromlo and Siding Spring Observatories,
Institute of Advanced Studies,
The Australian National University,
Canberra

August, 1989

A thesis submitted for the degree of
Doctor of Philosophy
of The Australian National University

Contribution of Candidate

This thesis consists of seven papers, each of which has either been published or has been submitted for publication. These papers have been written in collaboration with several researchers. Their contributions are outlined below:

- Chapter 2 contains the text of a paper published in the *Astrophysical Journal* (341, 327) with Drs. D.T. Wickramasinghe and I.R. Tuohy. The construction of the radial velocity and dispersion velocity model was performed by the candidate with suggestions by Dr. Wickramasinghe. Both the candidate and Dr. Wickramasinghe contributed equally to the discussion on the radial velocity and velocity dispersion behaviour in AM Herculis systems. The model fits to the data of three AM Herculis systems were performed by the candidate. This work benefitted greatly from discussions with Dr. Tuohy.
- Chapter 3 contains the text of a paper published in the *Astrophysical Journal* (334, 412) with Dr. D.T. Wickramasinghe. The modelling was carried out with Dr. Wickramasinghe. Both the candidate and Dr. Wickramasinghe contributed equally to the discussion on the properties of cylindrically extended cyclotron emission regions.
- Chapter 4 contains the text of a paper submitted for publication in the *Astrophysical Journal* with Dr. D.T. Wickramasinghe. The arc-shaped cyclotron emission region model was constructed by the candidate, subject to suggestions from Dr. Wickramasinghe. The model fits to the data of three AM Herculis systems were performed by the candidate.
- Chapter 5 contains the text of a paper published in the *Astrophysical Journal (Letters)* (342, L35) with Drs. D.T. Wickramasinghe and J.A. Bailey. The observations were carried out by all of the authors and the

data reduction by Dr. Bailey. The data interpretation was performed by the candidate with suggestions by Dr. Wickramasinghe.

- Chapter 6 contains the text of a paper published in the *Astrophysical Journal* (337, 832) with Drs. D.T. Wickramasinghe, J.A. Bailey, I.R. Tuohy, and J.H. Hough and a section from a paper published in a conference proceedings with Dr. D.T. Wickramasinghe. The spectroscopic observations were carried out by the candidate and Drs. Wickramasinghe, Bailey and Tuohy. The data reduction was performed by the candidate. The polarimetric observations were carried out by Drs. Bailey and Hough and reduced by Dr. Bailey. The sections on the eclipse properties and the secondary star are due to Dr. Bailey. Both the candidate and Dr. Wickramasinghe contributed equally to the discussion on the cyclotron spectrum. The model fits to the cyclotron spectrum and polarization data, as well as the radial velocity analysis, were performed by the candidate.
- Chapter 7 contains the text of a paper published in the *Astrophysical Journal (Letters)* (328, L59) with Drs. I.R. Tuohy, D.T. Wickramasinghe, and M.R.S. Hawkins. The photometric observations were carried out by the candidate and Dr. Tuohy. The reduction was performed by Dr. Tuohy. The candidate and Dr. Wickramasinghe modelled the multicolour light curves. Dr. Hawkins provided the long-term monitoring of Grus V1 obtained through UK Schmidt plates.

.....
Felix Fenais.....

August, 1989

Acknowledgements

I am particularly indebted to my supervisor Dayal Wickramasinghe for his encouragement and guidance over the past three years. His enthusiasm and understanding have been of great value in helping me overcome all of the problems which I faced during the course of my thesis. His continued support has served to enhance the content of this work.

I am also very grateful to my co-supervisor Ian Tuohy for helping me to become familiar with observational techniques and data analysis.

I would like to thank the past and present Directors of Mount Stromlo and Siding Spring Observatories, Professors Don Mathewson and Alex Rodgers, for allowing me to use of the excellent facilities of the Observatories. My thanks also go to the technical and clerical staff at Mount Stromlo and Siding Spring Observatories for their excellent support.

I wish to thank the telescope time assignment committees of MSSSO and of the Anglo-Australian Telescope for their generous allocations of telescope time.

I would like to thank all of the academic staff and students at Mount Stromlo; in particular my advisor, Ken Freeman, for his support when I arrived in Australia.

This work was supported by an Australian National University Postgraduate Scholarship, for which I am grateful.

Abstract

We begin by presenting a theoretical model for the radial velocity and velocity dispersion of the broad emission line component in AM Herculis systems assuming that it originates mainly in the gas which is diverted out of the orbital plane and funneled on to the white dwarf surface along magnetic field lines. The model is used to locate the line forming region in three AM Her variables using as constraints the radial velocity and velocity dispersion data. This work shows that the material is threaded by the magnetic field in a very azimuthally extended coupling region located 0.5 – 0.75 of the way between the white dwarf and the inner Lagrange point. This implies that the cyclotron emission region on the stellar surface is extended, probably arc-shaped, and offset from the magnetic pole.

Models for cylindrically extended and arc-shaped cyclotron emission regions displaced from the magnetic poles are then generated, taking into account the effects of field spread across the shock. The properties of cylindrically extended models with density and temperature structure and geometrical extension are also investigated. These models are an improvement on previous point source models and have characteristics that are in better overall agreement with the properties of AM Herculis systems.

Phase dependent spectropolarimetric observations of VV Puppis which show, for the first time, cyclotron lines from both poles are presented. The main and secondary emission regions have fields of 30.5 MG and 56 MG respectively. The observations have been interpreted in terms of a dipole which is offset by ≈ 0.1 white dwarf radii from the center of the star in the direction of the dipole axis with the emission regions located near the foot points of closed field lines.

Spectroscopic and circular polarization observations of the soft X-ray eclipsing binary EXO 033319–2554.2 which confirm it as a member of the

AM Herculis class are presented. Broad resolvable and variable cyclotron harmonics from both poles are seen during the bright phase corresponding to magnetic fields of 56 MG (main region) and 28 MG (secondary region). As is the case for VV Puppis, the large difference in magnetic field strength of the two regions implies a more complex field structure than that of a centered dipole field distribution, if it is assumed that the regions are connected by closed field lines.

UBVRI and long term plate photometry of the faint and highly erratic cataclysmic variable discovered from a sequence of UK Schmidt measurements are presented. We show that this object (designated Grus V1) is almost certainly a new AM Herculis variable, and develop a model in which the light curves are explained as originating from two nonpolar cyclotron emission regions.

1. Introduction	13
2. Roche Lobes and White Dwarf Magnetospheres	16
2.1. A Model for the Broad Emission Line Component in AM Herculis Systems	23
2.1.1. The Accretion Funnel	24
2.1.2. Acceleration Region	25
2.2. Sensitivity of the Model to the Input Parameters	26
2.3. Application to Three AM Herculis Systems	31
2.3.1. <i>EXO 030219-2534.8</i>	31
2.3.2. <i>GW1103+854</i>	36
2.3.3. <i>EXO 030219-2534.8</i>	39
2.4. Discussion	42
2.5. Conclusions	44
2.6. References	46
3. Cyclotron Emission from Inhomogeneous Shocks in AM Herculis Systems	49
3.1. Abstract	49
3.2. Introduction	50

Contents

1	Introduction	1
1.1	References	9
2	An Emission Line Model for AM Herculis Systems	12
2.1	Abstract	12
2.2	Introduction	13
2.3	Roche Lobes and White Dwarf Magnetospheres	15
2.4	A Model for the Broad Emission Line Component in AM Herculis Systems	22
2.4.1	<i>The Accretion Funnel</i>	23
2.4.2	<i>Acceleration Region</i>	26
2.5	Sensitivity of the Model to the Input Parameters	26
2.6	Application to Three AM Herculis Systems	31
2.6.1	<i>E1405-451</i>	31
2.6.2	<i>CW1103+254</i>	36
2.6.3	<i>EXO 033319-2554.2</i>	39
2.7	Discussion	42
2.8	Conclusions	44
2.9	References	46
3	Cyclotron Emission from Inhomogeneous Shocks in AM Herculis Systems	49
3.1	Abstract	49
3.2	Introduction	50

3.3	Results and Discussion	51
3.3.1	<i>The Models</i>	51
3.3.2	<i>General Properties of Extended Emission Regions</i> . . .	54
3.3.3	<i>Phase Dependent Polarization and Light Curves</i> . . .	59
3.3.4	<i>Density and Temperature Structure</i>	63
3.4	Conclusions	69
3.5	References	70
4	Arc-Shaped Cyclotron Emission Regions in AM Herculis Systems	72
4.1	Abstract	72
4.2	Introduction	73
4.3	Why Arc-Shaped Cyclotron Emission Regions?	74
4.4	The Models	76
4.5	General Properties of Arc-Shaped Cyclotron Emission Regions	78
4.6	Application to Three AM Herculis Systems	84
4.6.1	<i>Non-Eclipsing Cyclotron Emission Region: Application to E1405-451</i>	84
4.6.2	<i>Eclipsing Cyclotron Emission Region: Application to VV Puppis</i>	91
4.6.3	<i>Eclipsing Cyclotron Emission Region: Application to CW1103+254</i>	94
4.7	Conclusions	96
4.8	References	98
5	A 56 MG Field at the Second Pole in VV Puppis	100
5.1	Abstract	100
5.2	Introduction	101
5.3	Observations	101
5.4	Discussion	106
5.5	References	110

6	EXO 033319–2554.2: An Eclipsing AM Herculis System Showing Cyclotron Emission Features	111
6.1	Abstract	111
6.2	Introduction	113
6.3	Observations	113
6.3.1	<i>Polarimetry and Photometry</i>	113
6.3.2	<i>Spectroscopy</i>	114
6.4	Results and Discussion	121
6.4.1	<i>Polarization Behaviour</i>	121
6.4.2	<i>Eclipse Properties</i>	123
6.4.3	<i>The Secondary Star</i>	125
6.4.4	<i>Radial Velocity Curves</i>	126
6.4.5	<i>The Cyclotron Spectrum</i>	128
6.5	Conclusions	136
6.6	Circular Polarisation Modelling	138
6.7	References	141
7	Evidence for Nonpolar Emission Regions in a New AM Herculis Candidate	144
7.1	Abstract	144
7.2	Introduction	146
7.3	Observations and Results	146
7.3.1	<i>UK Schmidt Plate Photometry</i>	146
7.3.2	<i>UBVRI Photometry</i>	147
7.4	Discussion	151
7.5	Summary Remarks	156
7.6	References	157

List of Figures

1.1	Schematic Diagram of an AM Herculis System	4
2.1	White Dwarf Geometry	17
2.2	White Dwarf Magnetosphere	19
2.3	Geometry of the Model	24
2.4	Effect of Change in Extent and Location	28
2.5	Effect of Change in Orbital Inclination	30
2.6	Effect of Change in Coupling Radius	31
2.7	Application of Model to E1405-451 (a)	34
2.8	Application of Model to E1405-451 (b)	35
2.9	Application of Model to CW1103+254	38
2.10	Application of Model to EXO 033319-2554.2	41
3.1	Model Geometry	52
3.2	Polarization and Intensity Behavior	55
3.3	Harmonic Visibility as a Function of Polar Cap Size	58
3.4	Phase Dependent Polarization and Light curves	60
3.5	Intensity and Polarization Curves for Structured Models	64
3.6	Intensity and Polarization Curves at different i	65
3.7	Harmonic Number Dependence on Model Parameters	67
4.1	Model Geometry	77
4.2	Theoretical Intensity Curves	79
4.3	Theoretical Linear Polarization Curves	80
4.4	Theoretical Circular Polarization Curves	81

4.5	Theoretical Position Angle Curves	82
4.6	Application of Model to E1405-451: April 1983	86
4.7	Application of Model to E1405-451: June 1985	88
4.8	Application of Model to E1405-451: May 1984	90
4.9	Application of Model to VV Puppis	93
4.10	Application of Model to CW1103+254	95
5.1	Bright Phase Spectra	102
5.2	Faint Phase Spectra	103
5.3	Faint Phase Spectra with Best Fits	104
5.4	Bright Phase Spectra with Best Fit	107
6.1	Circular Polarization Data	115
6.2	Light Curves of the Eclipse	116
6.3	<i>J</i> -band Light Curve	117
6.4	Spectra	118
6.5	Spectrum at $\phi = 0.1$	119
6.6	Broad Band Spectrum at $\phi = 0.9$	120
6.7	Radial Velocity Curves	127
6.8	Derived Viewing Geometry of EXO 033319-2554.2	129
6.9	Predicted Cyclotron Harmonic Shift	132
6.10	Circular Polarization Modelling	139
7.1	Long Term Monitoring of Grus V1	147
7.2	Calibrated <i>UBVRI</i> Light Curves	149
7.3	Average <i>UBVRI</i> Light Curves	150
7.4	A Possible Geometry	154
7.5	Theoretical Intensity and Polarization Behavior	155

Chapter 1

Introduction

Before 1977, studies of magnetic white dwarfs were restricted to a few percent of isolated objects whose field strengths were found to be in the range 10–100 MG through the study of Zeeman features in their spectra. Attempts at detecting polarization in cataclysmic variables had met with no success until Tapia (1977) discovered the presence of $\approx 10\%$ circular polarization in the optical light of AM Herculis, an object that was found only one year earlier to be the optical counterpart of the hard X-ray source 4U1814+50 (Berg and Duthie 1977). The presence of such a high percentage of polarized light indicated that the white dwarf in the system is strongly magnetic and this object became the prototype of a new class of cataclysmic variables known as the AM Herculis-type systems.

At the present time, there are 15 variables (see Table 1.1) which have been identified as AM Herculis systems through the detection of polarization and 2 which are likely candidates (see Table 1.2). It is now well established that the observations of AM Herculis systems can be explained in terms of high harmonic cyclotron emission from a hot plasma ($T \approx 10 - 20$ keV) in accretion shocks near the surface of a strongly magnetized ($B \approx 20 - 60$ MG) white dwarf primary accreting from a low mass M star. The strength of the field is sufficient to prevent the formation of the usual CV accretion disk and to synchronize the rotation of the two stars with the orbital period ($\approx 80 - 220$ minutes). Accretion occurs directly on to the magnetic white

dwarf via an accretion stream, a coupling region, and magnetically confined accretion funnel(s) (Liebert and Stockman 1985; Wickramasinghe 1988) (see Figure 1.1).

The spectra of AM Herculis systems are characterized by prominent emission lines which are highly modulated at the binary period. The most important are the Balmer lines, HeII $\lambda 4686$, HeI $\lambda 4471$, and the high excitation blend CIII/NIII $\lambda\lambda 4640 - 4650$. The line profiles are complex, indicating the presence of many components, each with its own velocity variation. There is a broad base component with a velocity amplitude $\lesssim 1000 \text{ km s}^{-1}$ and dispersion $\lesssim 900 \text{ km s}^{-1}$, and a medium velocity component with a velocity amplitude $\lesssim 600 \text{ km s}^{-1}$ and dispersion $\lesssim 500 \text{ km s}^{-1}$ (*cf.* Rosen, Mason and Córdova 1986). These values are too large to be associated with the binary motion of the white dwarf and must therefore originate in the accretion flow close to the white dwarf. At sufficiently high resolution, it is also possible to recognize a further narrow component which can be attributed to the heated surface of the M dwarf or to the stream close to the inner Lagrange point.

It is generally possible to identify the broad base component with material which is diverted out of the orbital plane at the coupling region and is funneled towards the white dwarf along field lines. In chapter 2 we discuss the flow patterns that are expected for material which is coupled on to magnetic field lines in the orbital plane, and relate these to the recent evidence for the presence of two cyclotron emission regions in most AM Herculis systems. A model for the broad emission line component is also developed and applied to E1405-451 (=V834 Cen), CW1103+254 (=ST LMi) and the recently discovered AM Her system EXO 033319-2554.2 (see chapter 6). This work has showed that it is possible to use radial velocity and velocity dispersion data to determine the location and extent of the broad line emission region in systems where the orbital inclination and dipole orientation are known from other considerations.

From this study, it became clear that the emission region in AM Herculis systems were in general extended and displaced from the magnetic pole. As

TABLE 1.1: KNOWN AM HERCULIS SYSTEMS

Object	P (min)	m_v	B (MG)
EF Eri ¹ (= 2A0311-227) ...	81.0	13-15	?
DP Leo ² (= E1114+182) ...	89.8	17-21	44 (c) ³
VV Pup ⁴	100.4	14-18	32 & 56 (c) ⁵
V834 Cen ⁶ (= E1405-451) .	101.5	15-17	20-25 (c,z) ⁷
MR Ser ⁸ (= PG1550+191) .	113.6	15-17	36 (z) ⁹ or 25 (c) ³
BL Hyi ¹⁰ (= H0139-68)	113.6	15-18	30 (z) ¹¹
ST LMi ¹² (= CW1103+254)	113.9	15-17	30 (z) ¹³
1E1048.5+5241 ¹⁴	114.5	17.5-20	?
EXO023432-5232.3 ¹⁵	114.6	17-21	?
AN UMa ¹⁶	114.8	14-19	36 (c) ³ or 35 (c) ⁹
EXO033319-2554.2 ¹⁷	126.5	17-21	28 & 56 (c) ¹⁸
AM Her ¹⁹ (= 3U1809+50) .	185.7	12-15	14 (z) ²⁰
H0538+608 ²¹	199.3 ²²	14.5-17	41 (c) ³
V1500 Cyg ²³	201.0	17	?
QQ Vul ²⁴ (= E2003+225) ..	222.5	15-17	?

Note: (c) or (z) indicate whether the field strength has been estimated on the basis of cyclotron harmonics or Zeeman absorption features.

¹ Griffiths *et al.* (1979); ² Biermann *et al.* (1985); ³ Cropper *et al.* (1989); ⁴ Liebert *et al.* (1978); ⁵ Wickramasinghe and Meggitt (1982) and Wickramasinghe, Ferrario, and Bailey (1989); ⁶ Mason *et al.* (1983); ⁷ Wickramasinghe, Tuohy, and Visvanathan (1987); ⁸ Liebert *et al.* (1982); ⁹ Schmidt, Stockman, and Grandi (1986); ¹⁰ Visvanathan and Pickles (1982); ¹¹ Wickramasinghe, Visvanathan, and Tuohy (1984); ¹² Stockman *et al.* (1983); ¹³ Schmidt, Stockman, and Grandi (1983); ¹⁴ Morris *et al.* (1987); ¹⁵ Beuermann *et al.* (1987); ¹⁶ Krzemiński and Serkowski (1977); ¹⁷ Osborne *et al.* (1988); ¹⁸ Beuermann, Thomas, and Schwöpe (1988) and Ferrario *et al.* (1989); ¹⁹ Tapia (1977); ²⁰ Wickramasinghe and Martin (1985); ²¹ Remillard *et al.* (1986); ²² Mason, Liebert, and Schmidt (1989); ²³ Stockman, Schmidt, and Lamb (1988); ²⁴ Nousek *et al.* (1984).

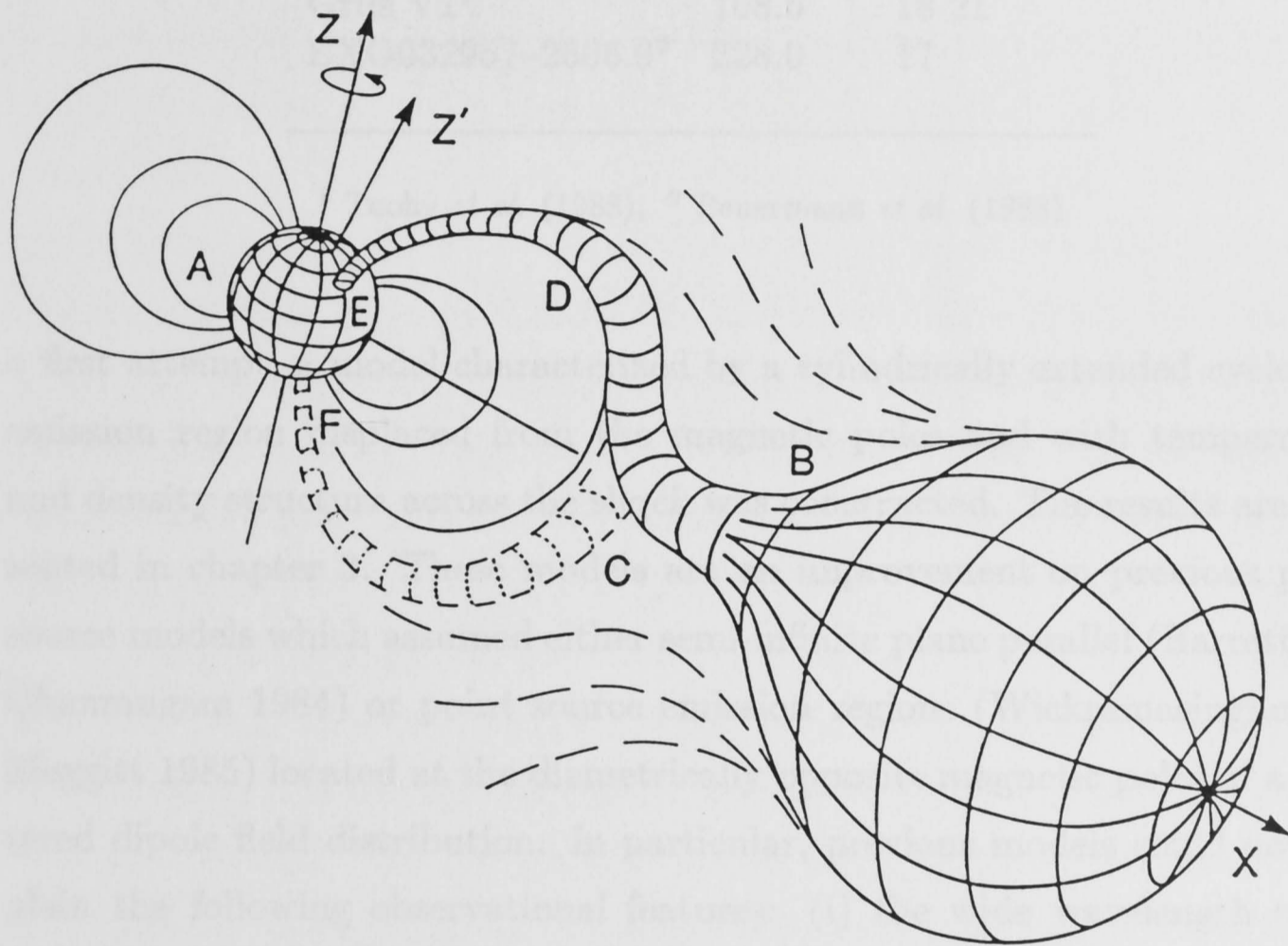


Figure 1.1: Schematic Diagram of an AM Herculis System

Z and Z' are the rotation axis and the dipole axis respectively. (A) Highly magnetic white dwarf; (B) low mass red star which is filling its Roche lobe; (C) the material leaves the inner Lagrange point; (D) the magnetic field diverts the gas out of the orbital plane and funnels it toward the white dwarf. (E) and (F) impact regions giving rise to cyclotron emission.

TABLE 1.2: AM HERCULIS SYSTEM CANDIDATES

Object	P (min)	m_v
Grus V1 ¹	108.6	18-21
EXO032957-2606.9 ²	228.0	17

¹ Tuohy *et al.* (1988); ² Beuermann *et al.* (1988).

a first attempt, a model characterized by a cylindrically extended cyclotron emission region displaced from the magnetic poles and with temperature and density structure across the shock was constructed. The results are presented in chapter 3. These models are an improvement on previous point source models which assumed either semi-infinite plane parallel (Barrett and Chanmugam 1984) or point source emission regions (Wickramasinghe and Meggitt 1985) located at the diametrically opposite magnetic poles of a centered dipole field distribution. In particular, previous models could not explain the following observational features: (i) the wide wavelength range over which circular and linear polarization are detected; (ii) flat polarized energy distributions in the optical seen in some systems; (iii) asymmetries in phase-dependent light and polarization curves and (iv) lack of clear harmonic pattern in most of the observations of AM Herculis systems.

Although models with cylindrically extended emission regions have shown that it is possible to explain most of the above characteristics, the asymmetries obtained in the phase dependent light and polarization curves were not large enough to explain observations of some systems such as E1405-451.

There is now considerable evidence suggesting that in some systems the emission regions are arc-like with a large angular extent (see Beuermann, Stella, and Patterson 1987; Cropper 1987; Schmidt 1988; Cropper 1989 and

also our radial velocity results of chapter 2). We present in chapter 4 calculations of the properties of arc-shaped cyclotron emission regions which extend over the stellar surface, taking into account the effects of field spread across the shock. The arc emission model has been applied to interpret some recent observations of E1405-451, VV Puppis and CW1103+254. We have found that it is possible to obtain large asymmetries in the polarization and intensity curves by introducing a considerable azimuthal extent and by elongating the emission region toward the magnetic equator. In the case of the observations of VV Puppis and CW1103+254, we show that we can reproduce the typical slow rise in intensity after eclipse egress and the more rapid decline into eclipse (Cropper 1986; Cropper and Warner 1986). Furthermore, it is also possible to obtain the flat-topped circular polarization curve characteristic of both VV Puppis and CW1103+254. These features were not reproducible using point source models or cylindrically symmetric emission regions.

A study of the magnetic fields of the white dwarfs in AM Herculis systems is important from several points of view. We note in particular that (i) due to their short rotation periods and the variety of field dependent phenomena that they exhibit (Zeeman lines, cyclotron lines, polarized continua, etc.), they provide an excellent opportunity for investigating field structure, perhaps in even more detail than has been possible with isolated magnetic white dwarfs. (ii) The evolution towards shorter periods is likely to be dominated by magnetic braking of the white dwarf, which in turn will depend on its magnetic moment. It is thus likely that the field holds the key to understanding the curious period distribution of the AM Hers, with 6 of the 15 known objects having periods near 114 minutes.

The magnetic field strength and structure of AM Herculis systems can be studied by two methods. During a low state, when there is little accretion, Zeeman features can be detected from the underlying white dwarf allowing the properties of the surface averaged field to be investigated. In the few cases when phase dependent data are available, it is possible to make useful

inferences about field structure (Schmidt 1988; Wickramasinghe 1988). In particular, Wickramasinghe and Martin (1985) used this method to deduce the presence of a dipole that was offset from the center of the star in AM Herculis.

The discovery of resolvable cyclotron harmonics in the bright phase optical spectra of VV Puppis (Visvanathan and Wickramasinghe 1979) opened up a new and unexpected method for studying magnetic fields. The cyclotron lines originate from accretion shocks near the white dwarf and are seen during a high state. Since the shocks cover only a small fraction ($\approx 10^{-4}$) of the white dwarf surface and are located typically about 10° from the magnetic poles (Wickramasinghe 1988), the cyclotron spectra provide a unique method of estimating polar field strengths and investigating field structure.

During this thesis work, the magnetic fields of VV Puppis and EXO033319-2554.2 were determined through the detection of cyclotron lines in their optical spectra. The discovery of prominent cyclotron lines in these two systems has been particularly exciting since new and unexpected results have arisen.

In chapter 5 we present phase dependent spectropolarimetric observations of VV Puppis which show, for the first time, cyclotron lines from both magnetic poles. The main and secondary emission regions have field strengths of 30.5 MG and 56 MG respectively. These observations have been interpreted in terms of a dipole which is offset by 10% of a white dwarf radius from the center of the star in the direction of the dipole axis with the emission regions located near the foot points of closed field lines. As in AM Herculis, the pole with the weaker field accretes more strongly and is located in the hemisphere that faces the companion star. Furthermore, our observations of VV Puppis show, again for the first time, a circularly polarized spectrum from an accretion shock when cyclotron harmonics are visible, which place strong constraints on possible shock models. The cyclotron lines are strongly polarized, as expected, and show surprisingly narrow peaks in the circular polarization data clearly pointing to the presence of an extended shock with

both low (≈ 2 keV) and high (≈ 20 keV) temperature regions.

Phase dependent spectroscopic and broad band polarimetric observations of EXO 033319–2554.2 are presented in chapter 6. These also show the presence of two cyclotron emission regions with field strengths of 56 MG (main region) and 28 MG (secondary region). Both regions appear to show cyclotron harmonics, although further observations are required to confirm the field attributed to the secondary region. If the difference in field strength in EXO 033319–2554.2 is real, the field structure of this object can also be interpreted in terms of an offset dipole.

Finally, in chapter 7 we report multicolour and photographic photometry of the faint and highly erratic cataclysmic variable V1 (to which we assign the temporary designation *Grus V1*), discovered by Hawkins (1981, 1983) from a sequence of UK Schmidt measurements. Observations of *Grus V1* show pronounced and repeatable modulation at a binary period of 108.6 minutes. Dramatic colour differences are evident in the *UBVRI* light curves: in the *U* band, a single sinusoidal peak is present, while at longer wavelengths a second red peak is dominant at a phase separation of $\Delta\phi \approx 0.5$. This behaviour is strongly suggestive of cyclotron emission from two non-polar emission regions in an AM Herculis system. The binary period and the long timescale two-state activity of the source also support this classification. We also develop a model in which the blue and red components originate from two cyclotron emission regions characterized by different electron temperatures and accretion rates.

1.1 References

- Barrett, P. E. and Chanmugam, G. 1984, *Ap. J.*, **278**, 298.
- Berg, R. and Duthie, J. 1977, *Ap. J. (Letters)*, **211**, 859.
- Beuermann, K., Stella, L., and Patterson, J. 1987, *Ap. J.*, **316**, 360.
- Beuermann, K., Thomas, H.-C., Giommi, P., and Tagliaferri, G. 1987, *Astr. Ap. (Letters)*, **175**, L9.
- Beuermann, K., Thomas, H.-C., Giommi, P., and Tagliaferri, G. 1988, *IAU Circ. No. 4671*.
- Beuermann, K., Thomas, H.-C., and Schwope, A. 1988, *Astr. Ap. (Letters)*, **195**, L15.
- Biermann, P., Schmidt, G. D., Liebert, J., Stockman, H. S., Tapia, S., Kühr, H., Strittmatter, P. A., West, S., and Lamb, D. Q. 1985, *Ap. J.*, **293**, 303.
- Cropper, M. 1986, *M. N. R. A. S.*, **222**, 853.
- Cropper, M. 1987, *M. N. R. A. S.*, **228**, 389.
- Cropper, M. 1989, *M. N. R. A. S.*, **236**, 935.
- Cropper, M., Mason, K. O., Allington-Smith, J. R., Branduardi-Raymont, G., Charles, P. A., Mittaz, J. P. D., Mukai, K., Murdin, P. G., Smale, A. P. 1989, *M. N. R. A. S.*, **236**, 29p.
- Cropper, M., and Warner, B. 1986, *M. N. R. A. S.*, **220**, 633.
- Ferrario, L., Wickramasinghe, D. T., Bailey, J. A., Tuohy, I. R., and Hough, J. H. 1989, *Ap. J.*, **337**, 832.
- Griffiths, R. E., Ward, M. J., Blades, J. C., Wilson, A. S., Chaisson, L., and Johnston, M. D. 1979, *Ap. J. (Letters)*, **232**, L27.
- Hawkins, M. R. S. 1981, *Nature*, **293**, 116.

- Hawkins, M. R. S. 1983, *Nature*, **301**, 688.
- Krzemiński, W., and Serkowski, K. 1977, *Ap. J. (Letters)*, **216**, L45.
- Lamb, D. Q., and Masters, A. R. 1979, *Ap. J. (Letters)*, **234**, L117.
- Liebert, J., and Stockman, H. S. 1985, in "Cataclysmic Variables and Low-Mass X-ray Binaries", ed. D. Q. Lamb and J. Patterson (Dordrecht: Reidel), p. 151.
- Liebert, J., Stockman, H. S., Angel, J. R. P., Woolf, N. J., Hege, K., Margon, B. 1978, *Ap. J.*, **225**, 201.
- Liebert, J., Stockman, H. S., Williams, R. E., Tapia, S., Green, R. F., Rautenkranz, D., and Ferguson, D. H. 1982, *Ap. J.*, **256**, 594.
- Mason, P. A., Liebert, J., and Schmidt, G. D. 1989, *Ap. J.*, in press.
- Mason, K. O., Middleditch, J., Córdova, F. A., Jensen, K. A., Reichert, G., Murdin, P. G., Clark, D., and Bowyer, S. 1983, *Ap. J.*, **264**, 575.
- Morris, S. L., Schmidt, G. D., Liebert, J., Stocke, J., Gioia, I., Maccacaro, T. 1987, *Ap. J.*, **314**, 641.
- Nousek, J. A., Takalo, L. O., Schmidt, G. D., Tapia, S., Hill, G. J., Bond, H. E., Grauer, A. D., Stern, R. A., Agrawal, P. C. 1984, *Ap. J.*, **277**, 682.
- Osborne, J. P., Giommi, P., Angelini, L., Tagliaferri, G., and Stella, L. 1988, *Ap. J. (Letters)*, **328**, L45.
- Remillard, R. A., Bradt, H. V., McClintock, J. E., Patterson, J., Roberts, W., Schwartz, D. A., Tapia, S. 1986, *Ap. J. (Letters)*, **302**, L11.
- Rosen, S. R., Mason, K. O., and Córdova, F. A. 1986, *M. N. R. A. S.*, **224**, 987.
- Schmidt, G. D., Stockman, H. S., and Grandi, S. A. 1983, *Ap. J.*, **271**, 735.
- Schmidt, G. D., Stockman, H. S., and Grandi, S. A. 1986, *Ap. J.*, **300**, 804.
- Schmidt, G. D. 1988, Vatican Workshop, "Polarized Radiation of Circumstellar Origin", Ed. Coyne, G. V., Magalhaes, A. M., Moffat, A. F. J.,

- Schulte-Ladbeck, R. E., Tapia, S., and Wickramasinghe, D. T., (Vatican Press), p. 85.
- Stockman, H. S., Foltz, C. B., Schmidt, G. D., and Tapia, S. 1983, *Ap. J.*, **271**, 725.
- Stockman, H. S., Schmidt, G. D., and Lamb, D. Q. 1988, *Ap. J.*, **332**, 282.
- Tapia, S. 1977, *Ap. J. (Letters)*, **212**, L125.
- Tuohy, I. R., Ferrario, L., Wickramasinghe, D. T., and Hawkins, M. R. S. 1988, *Ap. J. (Letters)*, **328**, 159.
- Visvanathan, N., and Pickles, A. 1982, *Nature*, **298**, 41.
- Visvanathan, N. and Wickramasinghe, D. T. 1979, *Nature*, **281**, 47.
- Wickramasinghe, D. T. 1988, Vatican Workshop, Vatican Workshop, "*Polarized Radiation of Circumstellar Origin*", Ed. Coyne, G. V., Magalhaes, A. M., Moffat, A. F. J., Schulte-Ladbeck, R. E., Tapia, S., and Wickramasinghe, D. T., (Vatican Press), p.1.
- Wickramasinghe, D. T., Ferrario, L., and Bailey, J. A. 1989, *Ap. J. (Letters)*, **342**, L35.
- Wickramasinghe, D. T., and Martin, B. 1985, *M. N. R. A. S.*, **212**, 353.
- Wickramasinghe, D. T. and Meggitt, S. M. A. 1982, *M. N. R. A. S.*, **198**, 975.
- Wickramasinghe, D. T. and Meggitt, S. M. A. 1985, *M. N. R. A. S.*, **214**, 605.
- Wickramasinghe, D. T., Tuohy, I. R., and Visvanathan, N. 1987, *Ap. J.*, **318**, 326.
- Wickramasinghe, D. T., Visvanathan, N., and Tuohy, I. R. 1984, *Ap. J.*, **286**, 328.

Chapter 2

An Emission Line Model for AM Herculis Systems

2.1 Abstract

The optical spectra of the AM Herculis binaries are characterized by extremely complex emission lines whose profiles can be resolved into at least three components which are formed in different regions of the accretion stream leading from the companion star towards the magnetic white dwarf. We present a theoretical model for the radial velocity and velocity dispersion of the broad emission line component assuming that it originates mainly in the gas which is diverted out of the orbital plane and funneled on to the white dwarf surface along magnetic field lines. The model is used to locate the line forming region in three AM Her variables: E1405-451, CW1103+254 and EXO 033319-2554.2, using as constraints the radial velocity and velocity dispersion data. Our analyses of these systems show that the material is threaded by the magnetic field in a very azimuthally extended coupling region located 0.5 - 0.75 of the way between the white dwarf and the inner Lagrange point.

Subject headings: stars: accretion - stars: binaries - stars: dwarf novae - stars: magnetic - stars: white dwarfs

2.2 Introduction

The AM Her systems form a subclass of cataclysmic variables (CVs) which are characterized by the presence of strong linear and circular polarization at optical and near IR wavelengths. The polarized emission is of cyclotron origin, arising from accretion shocks near the surface of the strongly magnetized white dwarf primary of polar field strength $\approx 15 - 60$ MG. The strength of the field is sufficient to prevent the formation of the usual CV accretion disk and to synchronize the rotation of the two stars with the orbital period ($\approx 80 - 220$ minutes). Accretion occurs directly on to the magnetic white dwarf via an accretion stream, a coupling region, and magnetically confined accretion funnels (Liebert and Stockman 1985; Wickramasinghe 1988).

The spectra are characterized by prominent emission lines which are highly modulated at the binary period. The most important are the Balmer lines, HeII $\lambda 4686$, HeI $\lambda 4471$, and the high excitation blend CIII/NIII $\lambda\lambda 4640 - 4650$. The line profiles are complex, indicating the presence of many components, each with its own velocity variation. There is a broad base component with a velocity amplitude $\lesssim 1000$ km s $^{-1}$ and dispersion $\lesssim 900$ km s $^{-1}$, and a medium velocity component with a velocity amplitude $\lesssim 600$ km s $^{-1}$ and dispersion $\lesssim 500$ km s $^{-1}$ (*cf.* Rosen, Mason and Córdoba 1986). These values are too large to be associated with the binary motion of the white dwarf and must therefore originate in the accretion flow close to the white dwarf. At sufficiently high resolution, it is also possible to recognize a further narrow component which can be attributed to the heated surface of the M dwarf.

It is generally possible to identify the broad base component with material which is diverted out of the orbital plane at the coupling region and funneled towards the white dwarf along field lines. This is apparent in the majority of the systems, where the broad component is observed to vary in phase with the linear and circular polarization. For example, in E1405-451 (=V834

Cen), the maximum redshift occurs at the center of the circular polarization standstill at the phase where the field vector at the accretion shock points most directly towards the observer. This could only happen if the central field lines in the accretion funnel lie in a plane which is perpendicular to the orbital plane. It follows that in systems such as E1405-451, the dipole axis must point toward the coupling region, which, for dynamical reasons, must always lead the motion of the secondary. However, there are other systems, such as E1114+182 (=DP Leo), in which the dipole axis lags behind the secondary so that accretion from the coupling region can occur only along field lines that lie in planes which are inclined at oblique angles to the orbital plane. Therefore, in these systems the phase of maximum redshift of the broad component differs from the phase where the cyclotron emission region is viewed most directly (Wickramasinghe 1988).

With the exception of Schmidt, Stockman and Grandi (1983, hereafter SSG), previous attempts at interpreting emission line behavior have been mainly of a qualitative nature and have concentrated on the interpretation of the radial velocity variations, ignoring information on the line width changes. In this paper we develop a model which can be used for interpreting both the radial velocity and the velocity dispersion data of the broad component.

In §2.3 we discuss the flow patterns that are expected for material which is coupled on to magnetic field lines in the orbital plane and relate these to the recent evidence for the presence of two cyclotron emission regions in most AM Her systems. A model for the broad emission line component is developed in §2.4 and the sensitivity of the model to input parameters is discussed in §2.5. In §2.6 the model is applied to E1405-451, CW1103+254 (=ST LMi) and the recently discovered AM Her system EXO 033319-2554.2, where we show that it is possible to use radial velocity amplitude and dispersion data to determine the location and extent of the broad line emission region in systems where the orbital inclination and dipole orientation are known from other considerations. Our main results are summarised and discussed in §2.7. We remark that a preliminary report of this work has been given by Ferrario,

Wickramasinghe and Tuohy (1987).

2.3 Roche Lobes and White Dwarf Magnetospheres

The recent evidence for the presence of two cyclotron emission regions in most AM Her systems (see Wickramasinghe 1988, for a review) suggests that the flow pattern on to the white dwarf may be more complicated than previously envisaged. Since this could have a bearing on the analysis of radial velocity data, we first discuss this problem.

In the absence of a strong magnetic field, the particles leaving the inner Lagrange point r_L will form a stream (the "incident stream" in Lubow and Shu 1975) which reaches a minimum distance r_{min} from the primary, approaches the critical Roche surface, and finally turns back to impact on itself at a distance r_h ($> r_{min}$) from the primary. For direct accretion to be possible, it is necessary that the field dominates the flow before the minimum distance r_{min} is reached. The radius at which this occurs corresponds to the point where the magnetic pressure ($B^2/8\pi$) first dominates the gas ram pressure (ρv^2) of the accretion flow. We will refer to it as the coupling radius r_c . If we can approximate the motion of the accretion stream by assuming radial infall towards the white dwarf surface, it is easy to show that for a dipole of polar field strength B_p oriented at an angle θ_d to the spin axis, we have:

$$\frac{r_c}{R_{wd}} = 13.4 \left(\frac{B_p \sqrt{1 + 3 \sin^2 \theta_d}}{3 \times 10^7 \text{G}} \right)^{\frac{4}{7}} \left(\frac{f}{10^{-3}} \right)^{\frac{2}{7}} \left(\frac{M_{wd}}{M_\odot} \right)^{-\frac{8}{21}} \left(\frac{F}{10^{16} \text{g s}^{-1}} \right)^{-\frac{2}{7}}, \quad (2.1)$$

where $4\pi f$ is the solid angle covered by the stream, F is the mass transfer rate, and M_{wd} and R_{wd} are the mass and the radius of the white dwarf respectively with $R_{wd} = 0.01 R_\odot (M_\odot / M_{wd})^{1/3}$. In addition, the accretion

luminosity L_{acc} is given by:

$$L_{acc} = 1.9 \times 10^{33} \left(\frac{M_{wd}}{M_{\odot}} \right)^{\frac{4}{3}} \left(\frac{F}{10^{16} \text{g s}^{-1}} \right) \text{erg s}^{-1}. \quad (2.2)$$

It follows that for typical values of f ($\approx 10^{-2} - 10^{-3}$) and L_{acc} ($\approx 10^{33} - 10^{34}$ erg s $^{-1}$), we expect $r_c \approx 10 - 30R_{wd}$. For a typical mass ratio, q , in the range $0.1 - 0.25$, $r_{min} \approx 10R_{wd}$ so that an accretion disk is not expected to form at the fields appropriate to the AM Her variables. The material will be channeled along field lines that connect the coupling region to the white dwarf. The resulting flow pattern will depend on the location and extent of the coupling region and the orientation of the dipole.

Consider a coordinate system $Oxyz$ where the origin O is the center of the white dwarf, the x -axis coincides with the line joining the centers of the two stars and the z -axis is parallel to the rotation axis of the binary system. Suppose that the dipole is inclined at an angle θ_d to the z -axis and has rotational longitude ϕ_d with respect to the line of centers Ox . Consider a second rectangular coordinate system $Ox'y'z'$ also centered on the white dwarf, with the z' -axis parallel to the magnetic moment and with the x' axis in the plane Ozz' (see Fig. 2.1). If θ^* is the polar angle of the point P measured with respect to Oz' (the dipole axis) and ψ^* is the azimuthal angle with respect to Ox' , then the field line passing through P will have the following equation (Alfvén and Falthämmar 1963):

$$r = r_m \sin^2 \theta^*, \quad \psi^* = \text{constant}, \quad (2.3)$$

where r_m is the distance from the origin to the point of intersection of the magnetic field line with the magnetic equatorial plane $x'y'$. If material is coupled in the orbital plane to a field line at a distance r_c from the white dwarf at rotational longitude ϕ_c (measured from the projection of the dipole axis on to the orbital plane) and magnetic longitude ψ^* , the value of r_m defined by this field line is given by:

$$r_m = \frac{r_c}{\sin^2 \gamma}, \quad (2.4)$$

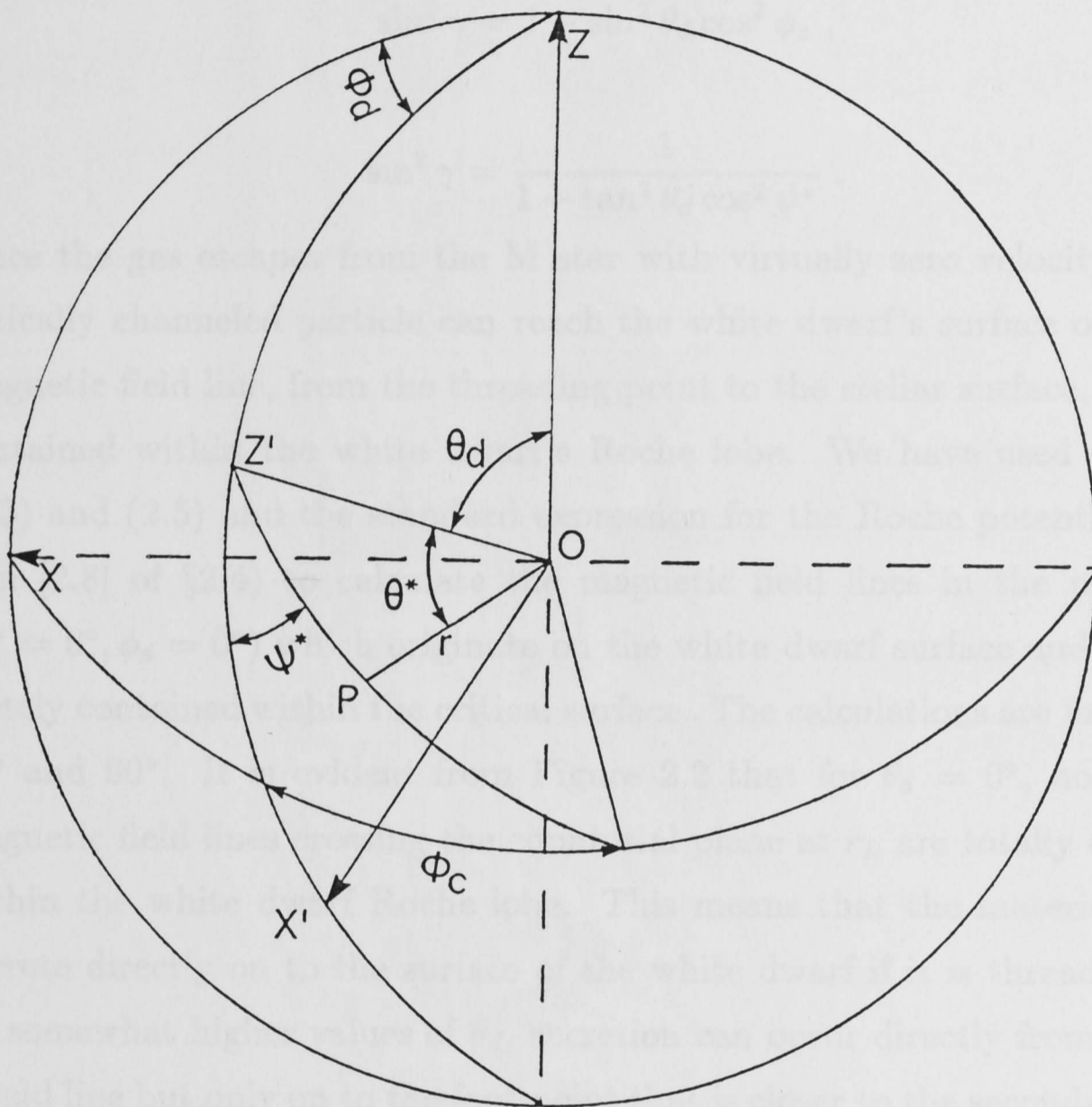


Figure 2.1: White Dwarf Geometry

The point O is the center of the white dwarf and the x -axis coincides with the line of centers. The z -axis is parallel to the rotation axis of the binary system. The z' -axis is parallel to the dipole axis and the x' -axis is in the plane Ozz' . The angle that the dipole axis forms with z is indicated by θ_d . The angle ϕ_d is the rotational longitude of the dipole axis measured from Ox . The angle θ^* is the polar angle of the point P measured with respect to Oz' and ψ^* is its azimuthal angle with respect to Ox' .

where γ is the angle between the dipole axis (Oz') and the line of intersection of the plane $\psi^* = \text{constant}$ with the orbital plane. It follows from simple geometry that:

$$\sin^2 \gamma = 1 - \sin^2 \theta_d \cos^2 \phi_c, \quad (2.5)$$

or:

$$\sin^2 \gamma = \frac{1}{1 + \tan^2 \theta_d \cos^2 \psi^*}. \quad (2.6)$$

Since the gas escapes from the M star with virtually zero velocity, a magnetically channeled particle can reach the white dwarf's surface only if the magnetic field line, from the threading point to the stellar surface, is wholly contained within the white dwarf's Roche lobe. We have used equations (2.3) and (2.5) and the standard expression for the Roche potential (equation [2.8] of §2.4) to calculate the magnetic field lines in the plane Oxz ($\psi^* = 0^\circ, \phi_d = 0^\circ$) which originate on the white dwarf surface and are completely contained within the critical surface. The calculations are for $\theta_d = 0^\circ, 45^\circ$ and 90° . It is evident from Figure 2.2 that for $\theta_d = 0^\circ$, none of the magnetic field lines crossing the equatorial plane at r_L are totally contained within the white dwarf Roche lobe. This means that the material cannot accrete directly on to the surface of the white dwarf if it is threaded at r_L . At somewhat higher values of θ_d , accretion can occur directly from r_L along a field line but only on to the foot point that is closer to the secondary. However, if the material is coupled to field lines further inside the white dwarf magnetosphere, there is a critical value r_c^{max} below which accretion can occur on to *two* regions.

We have constructed a series of diagrams similar to Figure 2.2 for a general orientation of the dipole ($\phi_d \neq 0^\circ$) and for flow along field lines with $\psi^* \neq 0^\circ$. These have been used to calculate the maximum coupling radius r_c^{max} consistent with accretion on to the foot points of closed field lines. The results are summarised in Table 2.1. It is possible to derive a simple formula which enables r_c^{max} to be estimated by noting that a closed field line will lie entirely within the critical Roche potential if the magnetospheric radius

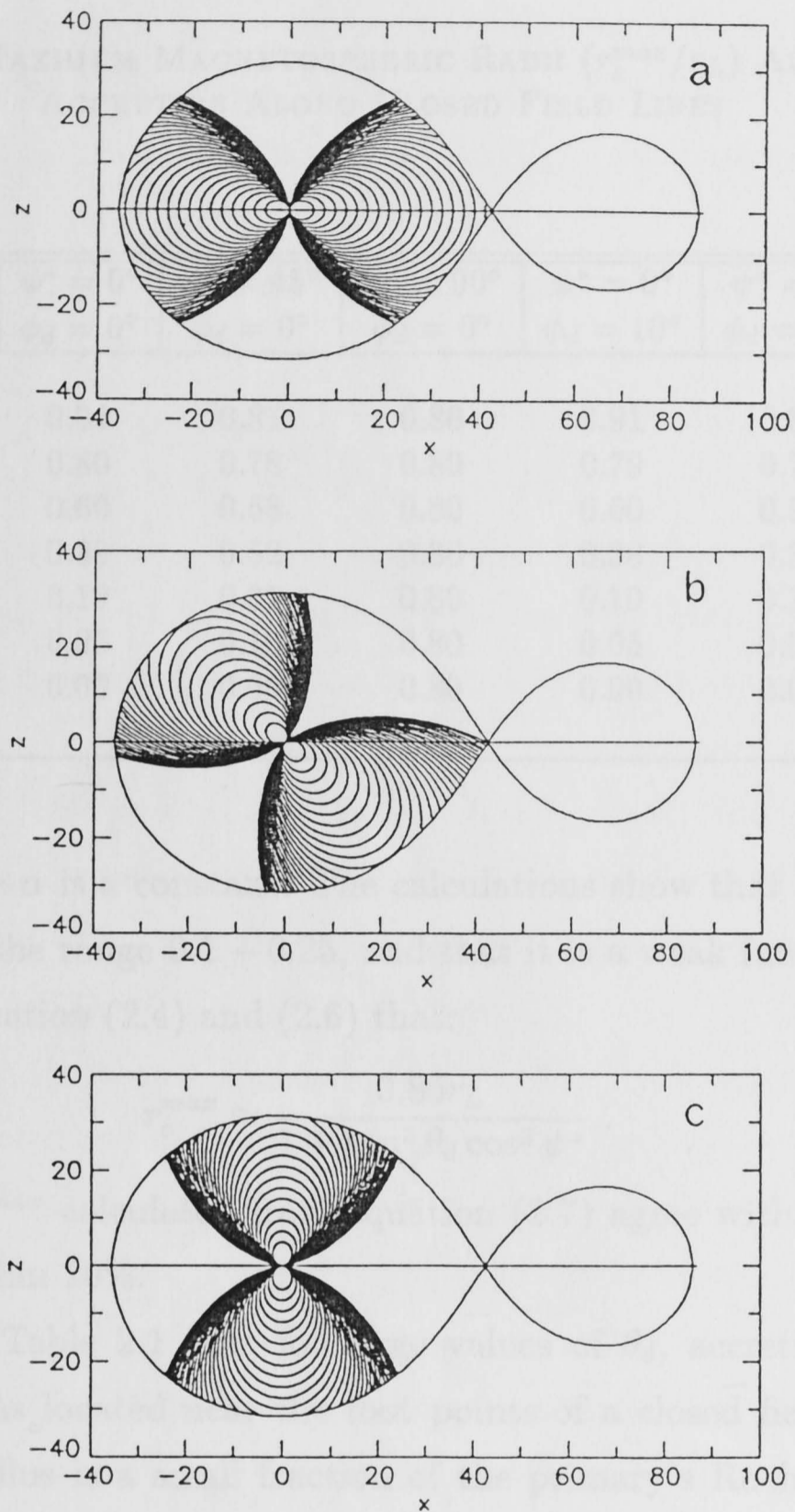


Figure 2.2: White Dwarf Magnetosphere

Part of the magnetosphere of the white dwarf which is contained within the Roche critical surface derived for different values of the magnetic colatitude θ_d . In (a), $\theta_d = 0^\circ$, in (b), $\theta_d = 45^\circ$ and in (c), $\theta_d = 90^\circ$. The case illustrated is that of a binary system with mass ratio $q = 0.25$. The figures have been obtained by cutting the Roche critical surface with a plane perpendicular to the orbital plane Oxy and passing through the line joining the centers of the two stars (x axis). The units are in white dwarf radii.

TABLE 2.1: MAXIMUM MAGNETOSPHERIC RADII (r_c^{max}/r_L) ALLOWED FOR ACCRETION ALONG CLOSED FIELD LINES

$\theta_d(^{\circ})$	$\psi^* = 0^{\circ}$ $\phi_d = 0^{\circ}$	$\psi^* = 45^{\circ}$ $\phi_d = 0^{\circ}$	$\psi^* = 90^{\circ}$ $\phi_d = 0^{\circ}$	$\psi^* = 0^{\circ}$ $\phi_d = 10^{\circ}$	$\psi^* = 0^{\circ}$ $\phi_d = 30^{\circ}$
0	0.94	0.81	0.80	0.91	0.84
15	0.80	0.78	0.80	0.79	0.76
30	0.60	0.68	0.80	0.60	0.59
45	0.39	0.52	0.80	0.38	0.38
60	0.19	0.31	0.80	0.19	0.19
75	0.05	0.10	0.80	0.05	0.05
90	0.00	0.00	0.80	0.00	0.00

$r_m < \alpha r_L$, where α is a constant. The calculations show that $\alpha \approx 0.85$ for a mass ratio q in the range 0.1 – 0.25, and that it is a weak function of ϕ_d . It follows from equation (2.4) and (2.6) that:

$$r_c^{max} \approx \frac{0.85r_L}{1 + \tan^2 \theta_d \cos^2 \psi^*} . \quad (2.7)$$

The values of r_c^{max} calculated from equation (2.7) agree with the results of Table 2.1 to within 10%.

It follows from Table 2.1 that for large values of θ_d , accretion will occur on to two regions located near the foot points of a closed field line only if the coupling radius is a small fraction of the primary's Roche lobe radius. Furthermore, accretion is expected to occur at different rates on to the two regions, with most of the material being directed on to the foot point which is closest to the orbital plane. When $r_c^{max} < r_c < r_L$, accretion can occur only on to the closer foot point, since a portion of the field line connecting the coupling region to the other foot point lies outside the critical Roche equipotential.

There is another way in which accretion can occur on to a second region. To see how this can happen, consider the line of intersection between the plane

through O perpendicular to the dipole axis (the magnetic equatorial plane) and the orbital plane. We will refer to it as the “critical line”, L_c . The foot points of each closed field line passing through L_c are symmetrically placed with respect to it. Thus, if coupling occurs at a point on L_c then accretion will occur on to both foot points with equal ease, provided the field line is wholly contained within the Roche lobe. It follows that accretion could occur at a high rate on to a second pole if the coupling region extends close to L_c . Let us assume that $\phi_d = 0^\circ$, but $\psi^* \neq 0^\circ$. As $\psi^* \rightarrow 90^\circ$, $r_c^{max} \approx 0.85r_L$, independent of the dipole orientation (*ie.* θ_d). Therefore, even if a second region is inaccessible by accretion along field lines in the plane $\psi^* \approx 0^\circ$ due to a large coupling radius, accretion may occur on to such a region from material which is coupled to field lines further upstream in the orbital plane. Given that $\langle r_c \rangle$ is likely to be large in AM Her systems, this is probably the only way in which accretion can occur on to a second region for a strongly inclined dipole. In this case, the two cyclotron emission regions would not lie near the foot points of a closed field line.

We conclude that the broad base component is likely to originate from material which is coupled to the field lines and diverted both above and below the orbital plane. The accretion funnel that feeds the main cyclotron emission region probably dominates in most systems, except for special orientations of the dipole (*eg.* $\theta_d \approx 0^\circ$) when both funnels may make similar contributions. However, the possibility exists that the viewing geometry in some systems may be such that the main cyclotron emission region is always eclipsed, so that the accretion funnel giving rise to the emission lines may not be the funnel that feeds the observed cyclotron emission region. We argue in §2.6.1 that this may be the case in E1405–451.

2.4 A Model for the Broad Emission Line Component in AM Herculis Systems

In this section we develop a model to interpret the observed radial velocity and velocity dispersion behavior in AM Her systems. We assume that a single accretion funnel dominates, although the same model can be used to consider two funnels. We also assume that the dipole points towards the red star ($\phi_d = 0^\circ$).

In order to model the accretion flow, we have divided the space between the stars into two different regions where the accreting material is subjected to a Roche potential, which per unit mass and at an arbitrary point $P(x, y, z)$, is given by Kopal (1959):

$$\Phi = \frac{GM_{wd}}{r} + \frac{GM_{rd}}{r'} + \frac{G(M_{wd} + M_{rd})}{2a^3} \left[\left(x - \frac{aM_{rd}}{M_{wd} + M_{rd}} \right)^2 + y^2 \right], \quad (2.8)$$

Here G is the gravitational constant, M_{wd} and M_{rd} are the masses of the white and red dwarfs respectively, a is the binary separation, and r and r' are the distances of P from the primary and the secondary stars respectively. We shall measure all the distances in units of white dwarf radii. A particle leaving r_L has a velocity V which satisfies:

$$V = \sqrt{2(\Phi(r) - \Phi(r_L)) + V_0^2}, \quad (2.9)$$

where $\Phi(r)$ is the potential energy at radius r from the white dwarf and $\Phi(r_L)$ and V_0 are the potential energy and the initial velocity of the material at r_L .

The first region consists of material which escapes from the M dwarf near the inner Lagrange point and is accelerated towards the white dwarf. We model this region (the "acceleration region", *cf.* Liebert and Stockman 1985) assuming radial infall towards the primary star. At the threading radius the magnetic field becomes strong enough to dominate the motion of the gas. The material is diverted out of the orbital plane and channeled towards the

white dwarf to impact on its surface in one (or two) spots. This region (the “accretion funnel”) is modeled by assuming flow along the field lines. We have introduced a density weighting factor which ensures that mass is conserved in the flow.

The vector radial velocity of a mass element is then given by the infall velocity, \vec{V}_i , of the material and the spin component, \vec{V}_s , both projected along the line of sight. Since the orbital component is much smaller than \vec{V}_i or \vec{V}_s , it has been neglected. The radial velocity is calculated as a density weighted mean of these velocities over the region where the emission lines are formed. We have assumed that the profiles of the emission lines are gaussians and calculate the full-width at half-maximum (FWHM) from $v_{\text{FWHM}} = 2.354\sigma$, where σ is the velocity dispersion obtained from the calculations.

In Figure 2.3 we have sketched the location of the two regions defining the parameters which enter our calculations. We will discuss the details of our calculations in the remainder of this section.

2.4.1 *The Accretion Funnel*

The geometry of this region has been outlined in §2.3. If ϕ is the binary phase, and i the binary inclination, the unit vector along the line of sight in the reference system $Oxyz$ is:

$$\vec{l} = (\sin i \cos 2\pi(\phi - \phi_0), -\sin i \sin 2\pi(\phi - \phi_0), \cos i). \quad (2.10)$$

The line of sight is in the xz plane at $\phi = \phi_0$. In the same reference system a particle is at position:

$$\vec{r} = r(\cos \theta^* \sin \theta_d + \sin \theta^* \cos \psi^* \cos \theta_d, \sin \theta^* \sin \psi^*, \quad (2.11)$$

$$\cos \theta_d \cos \theta^* - \sin \theta_d \sin \theta^* \cos \psi^*), \quad (2.12)$$

where r is given by equation (2.3). Let V_r and V_t be the magnitudes of the radial and tangential components of the velocity along the field lines:

$$V_r = -\frac{2V \cos \theta^*}{\sqrt{(4 \cos^2 \theta^* + \sin^2 \theta^*)}}, \quad (2.13)$$

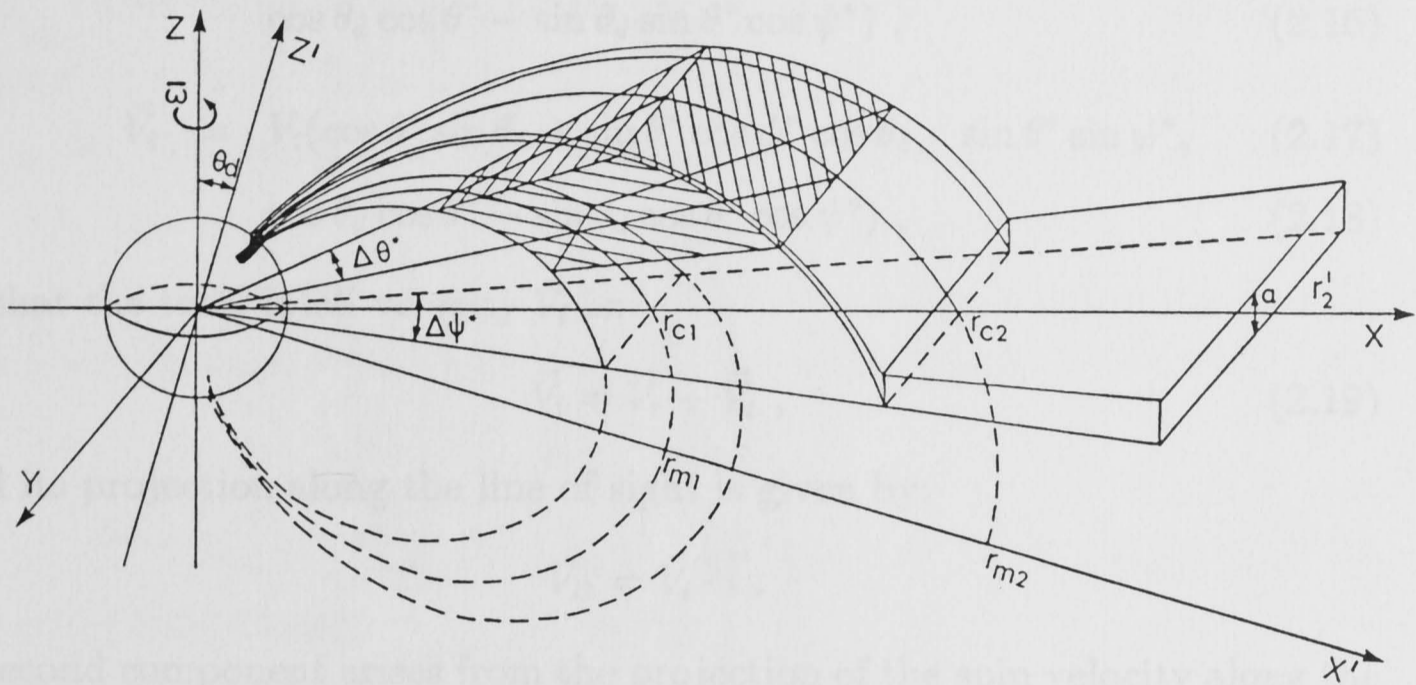


Figure 2.3: Geometry of the Model

Schematic diagram illustrating the geometry of our model. The z -axis coincides with the rotation axis while the z' -axis coincides with the dipole axis and is tilted at an angle θ_d with respect to the z -axis. Both axes lie in the plane Oxz ($\phi_d = 0^\circ$). The acceleration region is located between r_{c2} and r'_2 and has azimuthal extent $\Delta\psi^*$. Its vertical size is given by the angle α , measured at the center of the white dwarf. The material from the acceleration region feeds the accretion funnel via magnetic coupling which occurs between r_{c1} and r_{c2} . The dashed volume represents the magnetically channeled material which gives rise to the broad emission line component. This volume is delimited by r_{m1} , r_{m2} , $\Delta\psi^*$ and $\Delta\theta^*$.

$$V_t = -\frac{V \sin \theta^*}{\sqrt{(4 \cos^2 \theta^* + \sin^2 \theta^*)}} . \quad (2.14)$$

V has been defined in equation (2.9). The components of the velocity in the xyz system are then given by:

$$\vec{V}_r = V_r(\cos \theta^* \sin \theta_d + \sin \theta^* \cos \psi^* \cos \theta_d, \sin \theta^* \sin \psi^*, \quad (2.15)$$

$$\cos \theta_d \cos \theta^* - \sin \theta_d \sin \theta^* \cos \psi^*) , \quad (2.16)$$

$$\vec{V}_t = V_t(\cos \theta^* \sin \theta_d + \sin \theta^* \cos \psi^* \cos \theta_d, \sin \theta^* \sin \psi^*, \quad (2.17)$$

$$\cos \theta_d \cos \theta^* - \sin \theta_d \cos \theta^* \cos \psi^*) , \quad (2.18)$$

so that the total infall velocity \vec{V}_i is:

$$\vec{V}_i = \vec{V}_r + \vec{V}_t , \quad (2.19)$$

and its projection along the line of sight is given by:

$$V_{l1} = \vec{V}_i \cdot \vec{l} .$$

A second component arises from the projection of the spin velocity along the line of sight:

$$V_{l2} = (\vec{\omega} \wedge \vec{r}) \cdot \vec{l} , \quad (2.20)$$

where:

$$\vec{\omega} = (0, 0, \frac{2\pi}{P}) ,$$

and P is the period of the system. Consequently, the total radial velocity is given by:

$$V_r = V_{l1} + V_{l2} . \quad (2.21)$$

V_r is averaged over the volume of the accretion funnel which is defined by field lines with parameters $r_{m1} \leq r_m \leq r_{m2}$, $\theta_1^* \leq \theta^* \leq \theta_2^*$ and $\psi_1^* \leq \psi^* \leq \psi_2^*$. The foot points of the field lines which define the accretion funnel determine the extent of the cyclotron emission region on the surface. The maximum amount by which the cyclotron emission region is offset from the magnetic pole can be determined from:

$$\theta_{off}^* = \arcsin \left(\sqrt{\frac{1}{r_{m1}}} \right) . \quad (2.22)$$

2.4.2 Acceleration Region

The material in this region free falls towards the white dwarf surface and feeds the accretion funnel(s). The motion is assumed to be radial, with velocity given by equation (2.9). The spin component is calculated as in equation (2.20). The volume over which the radial velocity average is calculated is defined as follows. The azimuthal extent of the volume is given by $\psi_1^* \leq \psi^* \leq \psi_2^*$. The inner and outer radii are $r = r_{c2} = r_{m2} \cos^2 \gamma$ and $r = r'_2$ ($\leq r_L$), with γ given by equation (2.5) or (2.6), where $\psi^* = (\psi_1^* + \psi_2^*)/2$. Finally, the upper and lower boundaries are two planes passing through the origin and inclined at an angle $\pm\alpha/2$ to the orbital plane.

2.5 Sensitivity of the Model to the Input Parameters

In this section we investigate the response of the model to changes in the input parameters. We assume that the orbital inclination i and the orientation of the dipole can be determined from polarization data (Wickramasinghe 1988) and that the masses of the stars can be determined from the mass function of the system (Mukai and Charles 1987), and estimates of the mass of the M dwarf (Bailey 1985). We first neglect the acceleration region and consider only the accretion funnel. The variables of the model are then θ_1^* , θ_2^* , ψ_1^* , ψ_2^* , r_{m1} , r_{m2} and r'_2 . The constraints for the input parameters are the radial velocity and velocity dispersion curves. These are characterized by the phases and the values of the maximum and minimum of the radial velocity curves, and the phases and values of the local minima and maxima of the velocity dispersion curves.

For the simple case of accretion along a field line $r = r_m \sin^2 \theta^*$, we can calculate the component of the velocity along the line of sight (neglecting

spin) from:

$$V \approx V_{ff} \cos \beta , \quad (2.23)$$

and the dispersion from:

$$\Delta V \approx \frac{1}{2} V_{ff} \frac{\Delta r}{r} |\cos \beta| , \quad (2.24)$$

where:

$$V_{ff} = \sqrt{\frac{2GM_{wd}}{r}} ,$$

and:

$$\frac{\Delta r}{r} \approx 2 |\cot \theta^* \Delta \theta^*| . \quad (2.25)$$

Here β is the angle between the tangent to the field line (which is the velocity vector) and the line of sight. Therefore, for given $\Delta \theta^*$, the radial velocity V and the velocity dispersion ΔV increase as r becomes smaller. Furthermore, if the viewing angle is such that β crosses 90° (twice per rotation cycle) or approaches 90° , then V crosses zero and $\Delta V \rightarrow 0$ at these phases.

Let us first fix the values of the orbital inclination ($i = 45^\circ$) and colatitude of the magnetic pole ($\theta_d = 20^\circ$), and move the position of the emission region along the magnetic field lines for fixed values of r_{c1} and r_{c2} , ($23 R_{wd}$ and $24 R_{wd}$ respectively) and for $\Delta \psi^*$ constant and small ($\Delta \psi^* \approx 0.2$, $\langle \psi^* \rangle = 0^\circ$). The results are illustrated in the left hand panel of Figure 2.4. Note that from this point on, we will refer to r_{c1} and r_{c2} rather than to r_{m1} and r_{m2} (see Figure 2.3). The cases illustrated are somewhat more complicated due to the presence of a spread in Δr_c , $\Delta \theta^*$, $\Delta \psi^*$ and the inclusion of the spin term. However, the behavior is roughly as predicted by equations (2.20) and (2.21). The large positive values of the mean radial velocity for $20^\circ < \theta^* < 40^\circ$, imply that most of the gas in the emitting volume has reached the maximum height above the orbital plane and is falling in towards the white dwarf. The maximum (at $\phi \approx 1$) and the minimum (at $\phi \approx 0.5$) values of the dispersion correspond to the minimum and maximum values of $\langle \beta \rangle$. As $\langle \theta^* \rangle$ is increased, the emission region moves further away from the white dwarf and the maximum value of the velocity dispersion decreases. In addition,

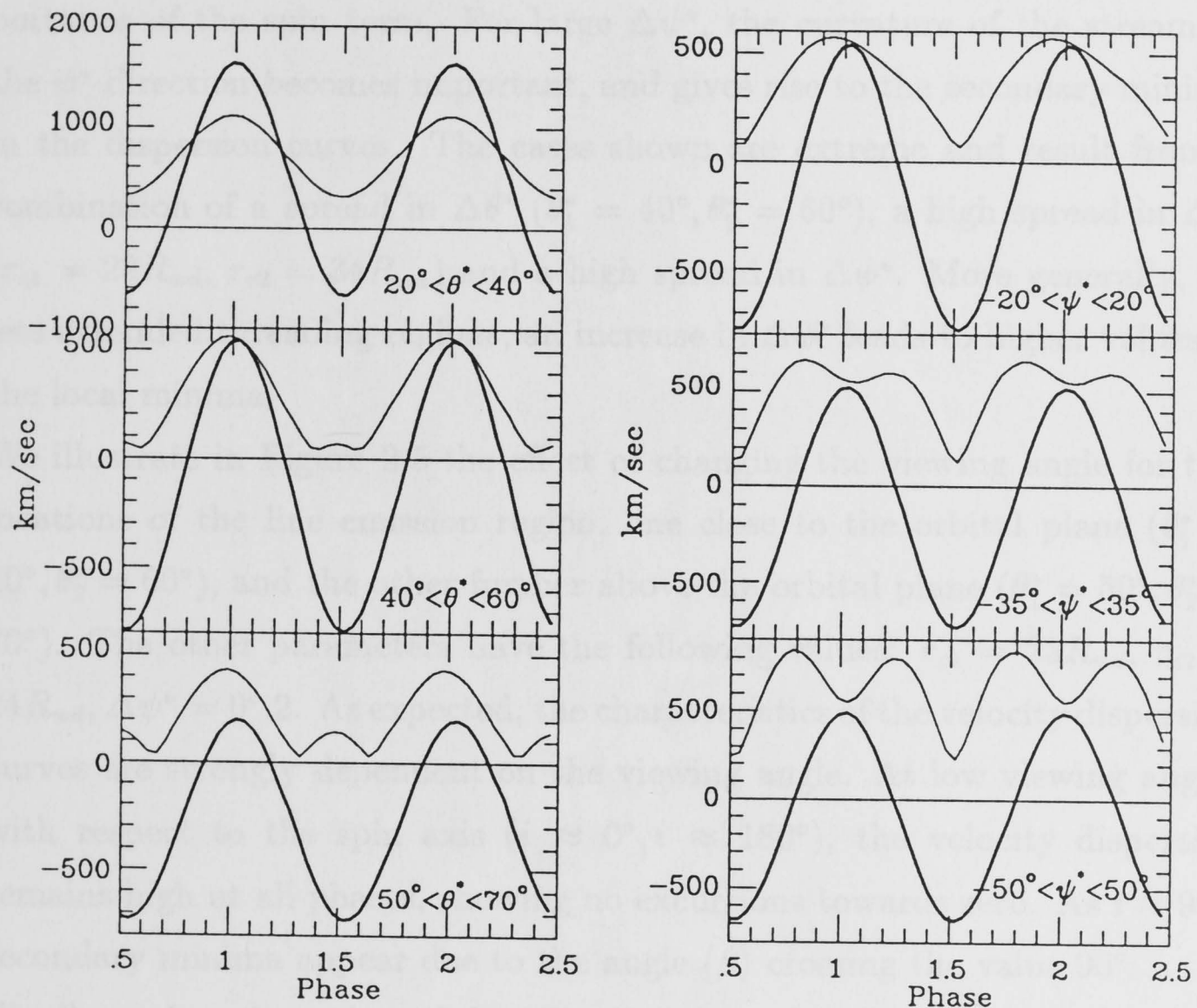


Figure 2.4: Effect of Change in Extent and Location

Left panel: theoretical curves obtained for the radial velocity (bold line) and FWHM for fixed values of $i = 45^\circ$ and $\theta_d = 20^\circ$, and a location and azimuthal extent of the threading region defined by: $23R_{wd} < r_c < 24R_{wd}$, $\Delta\psi^* = 0.2$. The three sub-panels correspond to different values of θ_1^* and θ_2^* . Right panel: theoretical curves derived for fixed values of $i = 45^\circ$, and $\theta_d = 20^\circ$ and for a fixed location of the emission region along the field lines defined by: $40^\circ < \theta^* < 60^\circ$, $23R_{wd} < r_c < 34R_{wd}$, The three sub-panels correspond to different values of ψ_1^* and ψ_2^* .

$\langle\beta\rangle$ crosses 90° twice, resulting in the appearance of two local minima in the velocity dispersion curves.

We have also calculated the effects of increasing $\Delta\psi^*$. The results are presented in the right hand panel in Figure 2.4. As $\Delta\psi^*$ is increased, the velocity dispersion curves tend to become more asymmetric due to the increasing importance of the spin term. For large $\Delta\psi^*$, the curvature of the stream in the ψ^* direction becomes important, and gives rise to the secondary minima in the dispersion curves. The cases shown are extreme and result from a combination of a spread in $\Delta\theta^*$ ($\theta_1^* = 40^\circ, \theta_2^* = 60^\circ$), a high spread in Δr_c ($r_{c1} = 23R_{wd}, r_{c2} = 34R_{wd}$) and a high spread in $\Delta\psi^*$. More generally, for less extended threading regions, an increase in $\Delta\psi^*$ leads to higher values of the local minima.

We illustrate in Figure 2.5 the effect of changing the viewing angle for two locations of the line emission region, one close to the orbital plane ($\theta_1^* = 40^\circ, \theta_2^* = 60^\circ$), and the other further above the orbital plane ($\theta_1^* = 50^\circ, \theta_2^* = 70^\circ$). The other parameters have the following values: $r_{c1} = 23R_{wd}, r_{c2} = 24R_{wd}, \Delta\psi^* = 0^\circ.2$. As expected, the characteristics of the velocity dispersion curves are strongly dependent on the viewing angle. At low viewing angles with respect to the spin axis ($i \approx 0^\circ, i \approx 180^\circ$), the velocity dispersion remains high at all phases, showing no excursions towards zero. As $i \approx 90^\circ$, secondary minima appear due to the angle $\langle\beta\rangle$ crossing the value 90° .

Finally, we have investigated the effects resulting from changes in the distance of the coupling region from the white dwarf, keeping the other parameters fixed: $i = 45^\circ, \theta_d = 20^\circ, \theta_1^* = 40^\circ, \theta_2^* = 70^\circ$ and $\Delta\psi^* = 0^\circ.2$. As expected, for threading radii further away from the white dwarf, the most evident effect (see Figure 2.6) is a decrease in the amplitude of both the radial velocity and FWHM curves. Also, the spin term becomes more important, giving rise to a phase shift between the two curves.

The gas in the acceleration region flows mainly in the orbital plane and contributes a term of small amplitude (which oscillates around zero km s^{-1}) to the radial velocity. It is possible that this region makes an important contri-

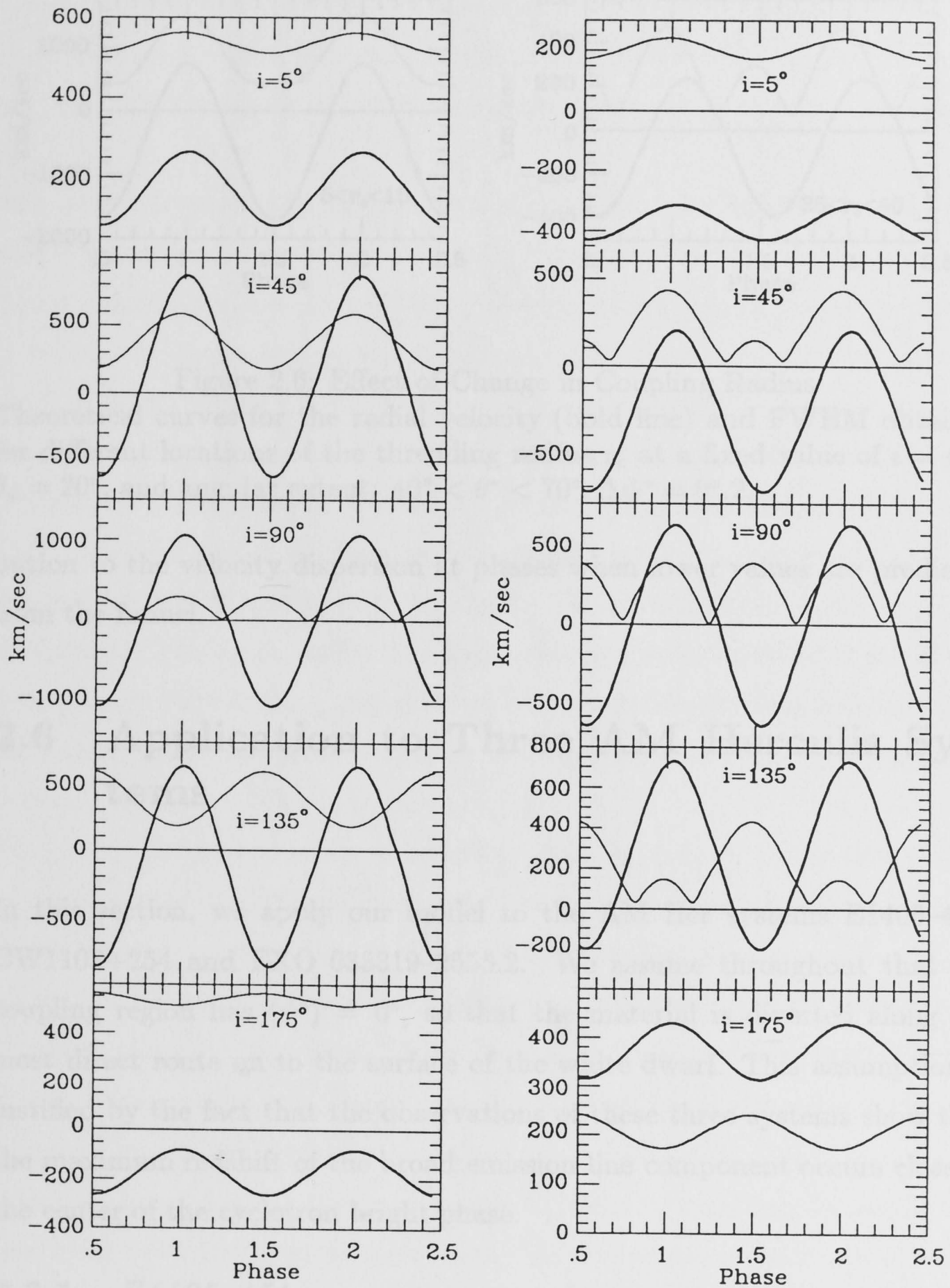


Figure 2.5: Effect of Change in Orbital Inclination

Left panel: theoretical curves for the radial velocity (bold line) and FWHM obtained for different values of i at a fixed value of $\theta_d = 0^\circ$, and for a fixed location and size of the line forming volume defined by: $40^\circ < \theta^* < 60^\circ$, $23R_{wd} < r_c < 24R_{wd}$ and $\Delta\psi^* = 0^\circ.2$. Right panel: same as left panel, but with $50^\circ < \theta^* < 70^\circ$.

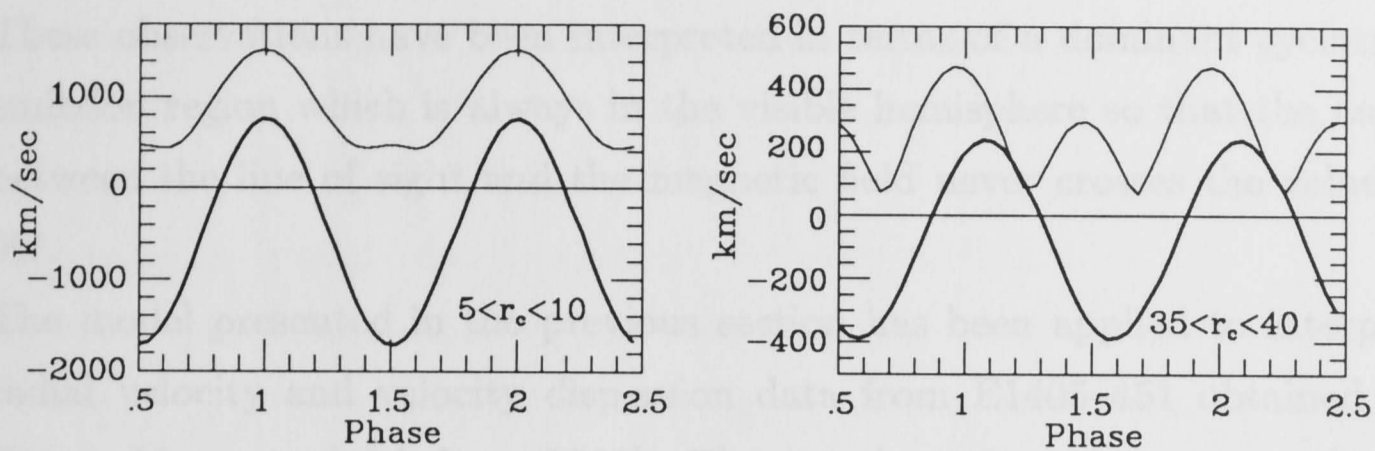


Figure 2.6: Effect of Change in Coupling Radius

Theoretical curves for the radial velocity (bold line) and FWHM obtained for different locations of the threading radius r_c at a fixed value of $i = 45^\circ$, $\theta_d = 20^\circ$, and angular extent: $40^\circ < \theta^* < 70^\circ$, $\Delta\psi^* = 0^\circ.2$.

tribution to the velocity dispersion at phases when lower values are predicted from the funnel.

2.6 Application to Three AM Herculis Systems

In this section, we apply our model to the AM Her systems E1405-451, CW1103+254 and EXO 033319-2555.2. We assume throughout that the coupling region has $\langle\psi^*\rangle = 0^\circ$, so that the material is diverted along the most direct route on to the surface of the white dwarf. This assumption is justified by the fact that the observations of these three systems show that the maximum redshift of the broad emission line component occurs close to the center of the cyclotron bright phase.

2.6.1 E1405-451

E1405-451 is an AM Her object with a period of 101.5 min (Jensen, Nousek and Nugent 1982). The light curve does not show any evidence for an eclipse and the circular polarization always shows the same sign (Bailey *et al.* 1983).

These observations have been interpreted in terms of a dominant cyclotron emission region which is always in the visible hemisphere so that the angle between the line of sight and the magnetic field never crosses the value of 90° .

The model presented in the previous section has been applied to interpret radial velocity and velocity dispersion data from E1405–451 obtained by Rosen, Mason and Córdoba (1986). These authors do not present a plot of their velocity dispersion data, but instead, quote the full width at the base of the lines at four different phases corresponding to minima and maxima in the dispersion. In order to compare their results with our model we have used a factor of 0.8 to convert between the width of the base and the FWHM of their gaussian, assuming that the line profile became indistinguishable from the continuum at a full width of $\approx 3\sigma$. We note that the minima of the FWHM are very high, indicating that a large spread in velocity is present even when we are looking at the accretion stream transversely. Furthermore, the masses of the two stars have been chosen to be consistent with the values deduced by Rosen, Mason and Córdoba (1986).

We have found two possible models to explain these data. In the first model, we assume that the emission lines arise from the accretion flow on to the cyclotron emission region that is visible at all phases and lies above the orbital plane. This follows the standard assumption made by previous investigators (Cropper, Menzies and Tapia 1986; Wickramasinghe and Meggitt 1985; and Tuohy, Visvanathan and Wickramasinghe 1985). The linear polarization angle variations indicate an orbital inclination $i \approx 45^\circ - 60^\circ$. Since the emission region is non-eclipsing, it is not possible to uniquely establish its position on the white dwarf surface from intensity or polarization observations. The presence of a linear polarization pulse detected near $\phi \approx 0.5$ (Cropper 1986 and Tuohy, Visvanathan and Wickramasinghe 1985) suggests that the field direction makes an angle $\approx 80^\circ - 90^\circ$ with the line of sight at this phase. If we assume that the emission region is near the magnetic pole with the field lines nearly radial, the dipole inclination is $\theta_d \approx 35^\circ - 20^\circ$. Given the

above constraints, the best fit that can be achieved is shown in Figure 2.7. The model has $i = 45^\circ$, $\theta_d = 20^\circ$, and the other parameters are summarised in Table 2.2. As Figure 2.7 shows, the model is only partially successful in explaining the radial velocity and FWHM observations.

If we are prepared to remove the constraints on θ_d , other models become possible. We note in particular that a significantly better fit can be obtained if we assume that the accretion flow which gives rise to the emission lines is located below the orbital plane, directing material on to a second region on the surface of the white dwarf. In fact, the best fit model for $i = 50^\circ$ has $\theta_d = -30^\circ$ and is shown in Figure 2.8. The parameters for this model (model b) are also given in Table 2.2. In model (b) most of the flow is directed on to a region of the white dwarf surface which does not make the dominant contribution to the observed polarized radiation. This model must be considered a possibility given the available data on this system. We note in this context that some observations of E1405-451 have revealed the presence of a linear pulse at visual wavelengths, even during the photometric minimum (Tapia 1982 and Visvanathan and Tuohy 1983). Very recently, Cropper (1988) has reported the detection of a strong linear polarization pulse at $\phi = 0.0$ in the I_{kc} band. These observations can be interpreted if one assumes the presence of a second emission region which comes into view near $\phi = 0.0$. Therefore, it is likely that the polarized radiation in E1405-451 arises from two different regions on the surface of the white dwarf. One of the emission regions may be visible at all phases while the other is only visible for part of the orbital cycle. In order to satisfy the circular polarization constraints, both regions have to be located on the hemisphere that faces the M dwarf. This may require an offset dipole. Until the positions of these regions can be determined from the polarization angle data, the plausibility of model (b) cannot be fully evaluated.

For model (a) we find that the gas has reached a velocity of $\approx 650 \text{ km s}^{-1}$ at r_{c2} . The cyclotron emission region on the surface of the white dwarf is offset from the dipole axis by a minimum value of $\approx 11^\circ$ and a maximum value of

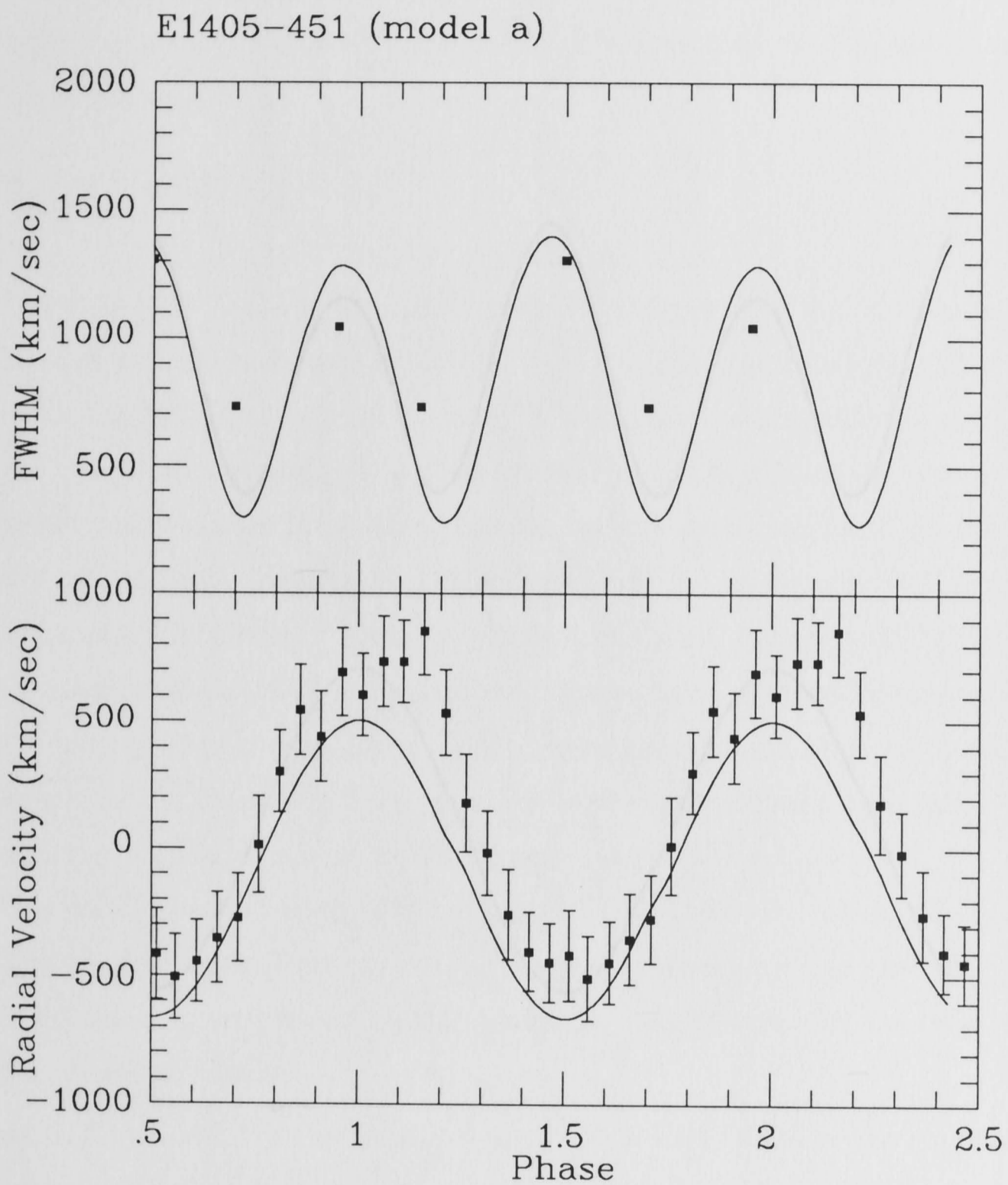


Figure 2.7: Application of Model to E1405-451 (a)
 Application of our model to the data for E1405-451 obtained by Rosen, Mason and Córdova (1986). Lower panel: comparison between the observed broad emission line radial velocity (squares) and the model. Upper panel: comparison between the observed FWHM (squares; see text) and the model.

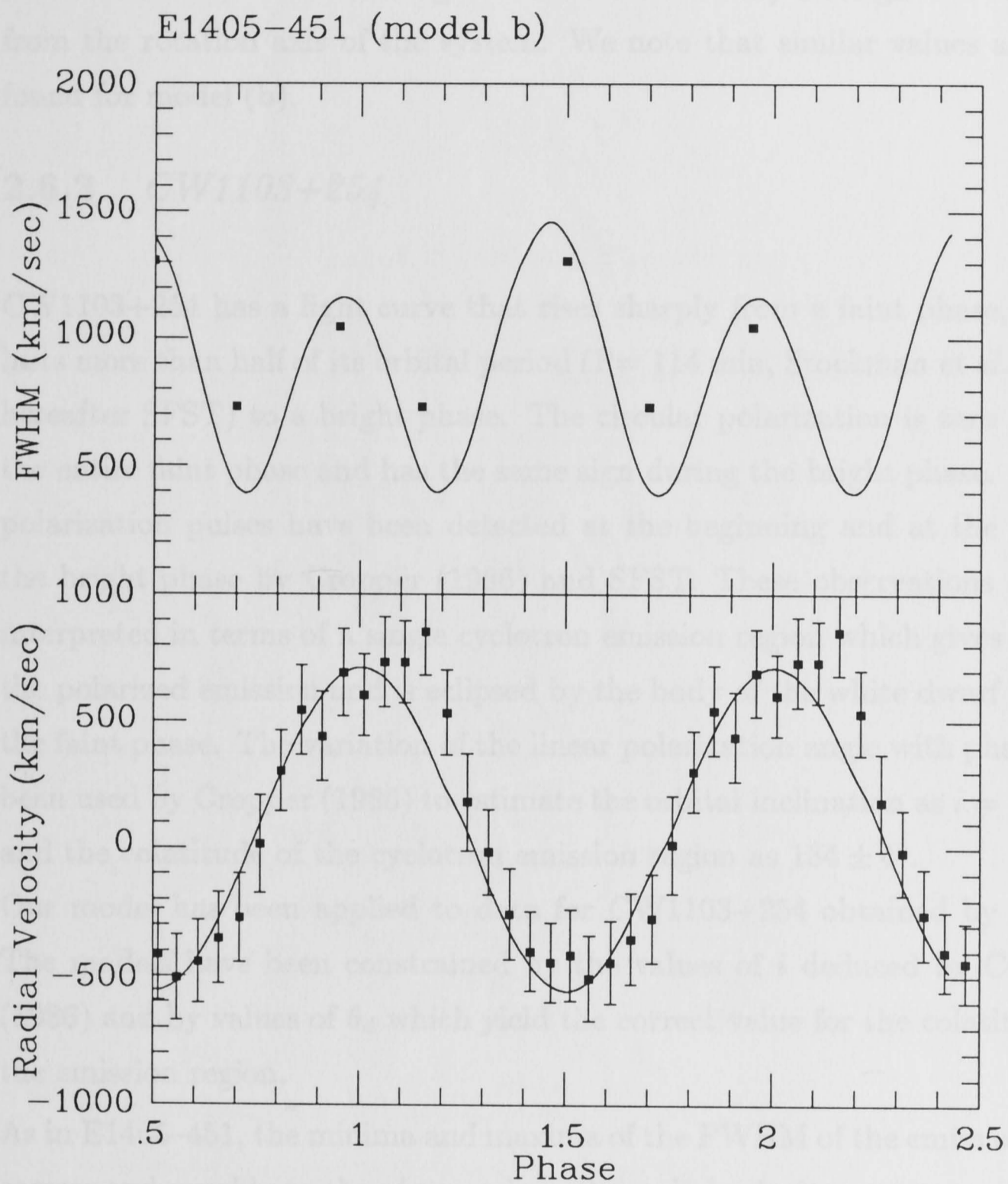


Figure 2.8: Application of Model to E1405-451 (b)
 Application of our model to the data for E1405-451 obtained by Rosen, Mason and Córdoba (1986). Lower panel: comparison between the observed broad emission line radial velocity (squares) and the model. Upper panel: comparison between the observed FWHM (squares; see text) and the model.

$\approx 12^\circ$. Therefore, the cyclotron emission region has an extent $\Delta\theta^* \approx 1^\circ$ in latitude and $\Delta\psi^* = 80^\circ$ in longitude and it is offset by an angle of about 31° from the rotation axis of the system. We note that similar values are also found for model (b).

2.6.2 CW1103+254

TABLE 2.2. MODEL PARAMETERS

CW1103+254 has a light curve that rises sharply from a faint phase, which lasts more than half of its orbital period ($P = 114$ min, Stockman *et al.*, 1983, hereafter SFST) to a bright phase. The circular polarization is zero during the entire faint phase and has the same sign during the bright phase. Linear polarization pulses have been detected at the beginning and at the end of the bright phase by Cropper (1986) and SFST. These observations can be interpreted in terms of a single cyclotron emission region which gives rise to the polarized emission and is eclipsed by the body of the white dwarf during the faint phase. The variation of the linear polarization angle with phase has been used by Cropper (1986) to estimate the orbital inclination as $i = 56 \pm 4^\circ$ and the colatitude of the cyclotron emission region as $134 \pm 4^\circ$.

Our model has been applied to data for CW1103+254 obtained by SFST. The models have been constrained by the values of i deduced by Cropper (1986) and by values of θ_d which yield the correct value for the colatitude of the emission region.

As in E1405-451, the minima and maxima of the FWHM of the emission lines correspond roughly to the phases where the radial velocity curve crosses zero and where it reaches the maximum amplitude respectively. Since the minima in FWHM are not as high as in E1405-451, the azimuthal extension of the coupling region must be smaller than in E1405-451. We have used values for the masses of the star which are consistent with those given by Bailey *et al.* (1985) and SSG ($M_{wd} = 0.6, M_{rd} = 0.15$). Figure 2.9 depicts our best fit to the data. The parameters of the model are summarised in Table 2.2. The agreement is not particularly good for the FWHM curve between $\phi = 0.32$

TABLE 2.2: MODEL PARAMETERS

Parameter	E1405 - 451		CW1103 + 254	EXO 033319 - 2554.2
	(a)	(b)		
P (min) .	101.5	101.5	113.9	126.5
B_p (MG)	25 ^a	25 ^a	30 ^b	56 ^c
$M_{wd}(M_{\odot})$	0.8	0.8	0.6	1.0
$M_{rd}(M_{\odot})$	0.2	0.2	0.15	0.1
R_{wd} (km)	7497	7497	8252	6960
$r_L(R_{wd})..$	42.5	42.5	37.9	61.5
i	+45°	+50°	+55°	+88°
θ_d	+20°	-30°	-30°	+4°
θ^*_1	+40°	+120°	+140°	+50°
θ^*_2	+60°	+150°	+160°	+86°
ψ^*_1	-40°	-40°	-20°	-40°
ψ^*_2	+40°	+40°	+20°	+40°
$r_{m1}(R_{wd})$	23	27	35	23
$r_{m2}(R_{wd})$	28	33	40	28
$r'_2(R_{wd})..$	35	35	37	37
α	2°	2°	6°	2°

^a Wickramasinghe, Tuohy and Visvanathan (1987)

^b Schmidt, Stockmann and Grandi (1983)

^c Beuermann, Thomas and Schwobe (1988); Ferrario *et al.* (1988)

CW1103+254

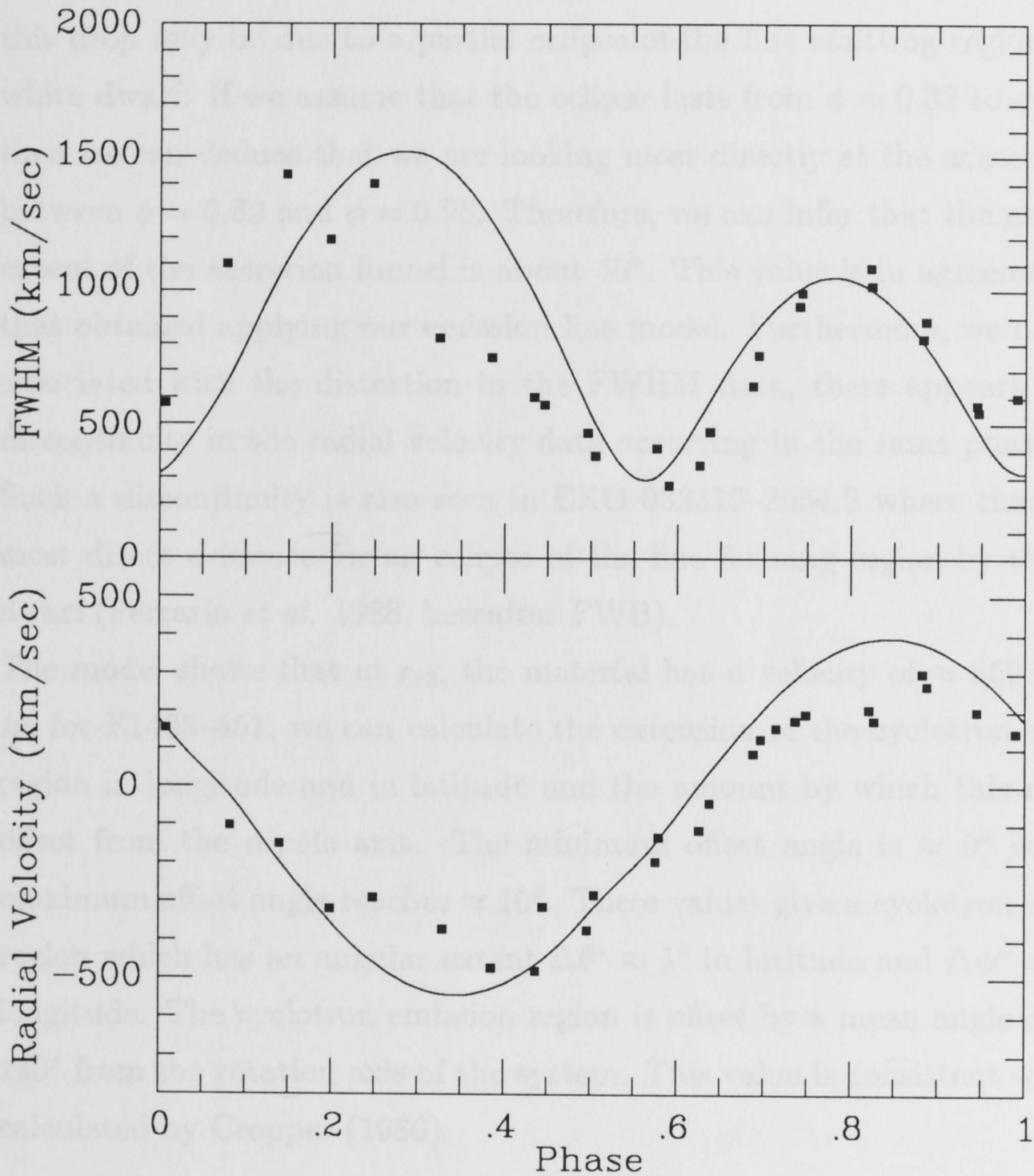


Figure 2.9: Application of Model to CW1103+254

Application of our model to the data for CW1103+254 obtained by Stockman *et al.* (1983) for which error bars were not given. Lower panel: comparison between the observed broad emission line radial velocity (squares) and the model. Upper panel: comparison between the observed FWHM (squares) and the model.

and $\phi = 0.45$, where the model predicts higher values. The distortion in the FWHM data may be related to the reduction in emission line flux (15%–30%) detected by SFST near $\phi = 0.45$. SFST and SSG have speculated that this drop may be due to a partial eclipse of the line emitting region by the white dwarf. If we assume that the eclipse lasts from $\phi = 0.32$ to $\phi = 0.45$, then we can deduce that we are looking most directly at the accretion flow between $\phi = 0.82$ and $\phi = 0.95$. Therefore, we can infer that the azimuthal extent of the accretion funnel is about 50° . This value is in agreement with that obtained applying our emission line model. Furthermore, we note that associated with the distortion in the FWHM data, there appears to be a discontinuity in the radial velocity data occurring in the same phase range. Such a discontinuity is also seen in EXO 033319–2554.2 where there is the most direct evidence for an eclipse of the line forming region by the white dwarf (Ferrario *et al.* 1988, hereafter FWB).

The model shows that at r_{c2} , the material has a velocity of $\approx 350 \text{ km s}^{-1}$. As for E1405–451, we can calculate the extension of the cyclotron emission region in longitude and in latitude and the amount by which this region is offset from the dipole axis. The minimum offset angle is $\approx 9^\circ$ while the maximum offset angle reaches $\approx 10^\circ$. These values give a cyclotron emission region which has an angular extent $\Delta\theta^* \approx 1^\circ$ in latitude and $\Delta\psi^* = 40^\circ$ in longitude. The cyclotron emission region is offset by a mean angle of about 140° from the rotation axis of the system. This value is consistent with that calculated by Cropper (1986).

2.6.3 EXO 033319–2554.2

EXO 033319–2554.2 was recently reported to be a soft X-ray source with a period of 126.7 minutes (Giommi *et al.* 1987; Osborne *et al.* 1988). Beuermann and Thomas (1987) identified EXO 033319–2554.2 with an 18th magnitude object and Bailey *et al.* (1987) confirmed its magnetic nature through the detection of circular polarization. Our model has been applied to radial

velocity data of EXO 033319–2554.2 obtained by FWB.

FWB and Berriman and Smith (1988) have indicated that two cyclotron emission regions contribute to the total light of EXO 033319–2554.2. Therefore we expect that two different accretion funnels will contribute to the emission line profiles of this system. As in E1405–451, we assume that the accretion funnel which feeds the main cyclotron emission region makes the dominant contribution to the radial velocity and velocity dispersion curves. The masses of the two stars ($M_{wd} = 1.0, M_{rd} = 0.1$) have been chosen to be consistent with the values determined by Beuermann, Thomas and Schwöpe (1988), and the mass ratio ($q = 0.1$) deduced by FWB from an analysis of the cyclotron spectrum. We have used $i = 88^\circ$ for the orbital inclination following FWB and have only considered values of θ_d which yield results that are consistent with the observed eclipse duration for the main emission region.

All the parameters employed in our calculations are displayed in Table 2.2 and the fits are illustrated in Figure 2.10. We note that the discrepancies between the theoretical curves and the data between $\phi = 0.35 - 0.55$ for both radial velocity and FWHM, are due to a partial eclipse of the line emission region by the accretion funnel itself and by the white dwarf (see FWB).

At r_{c2} , the material has reached a velocity of $\approx 900 \text{ km s}^{-1}$. The values deduced for the azimuthal extension of the cyclotron emission region are again very high ($\Delta\psi^* = 80^\circ$), close to those inferred by FWB through eclipse properties of the accretion funnel. The latitudinal extension ($\Delta\theta^* \approx 1^\circ$) and the offset angles of the cyclotron emission region from the dipole axis are near the values found for E1405–451 and CW1103+2554. The minimum offset angle is $\approx 11^\circ$ and the maximum is $\approx 12^\circ$. Therefore, the displacement of the main cyclotron emission region from the rotation axis is about 15° . This value for the location of the cyclotron emission region is in good agreement with the position deduced by FWB from the duration of the bright phase.

EXO 033319-2554.2

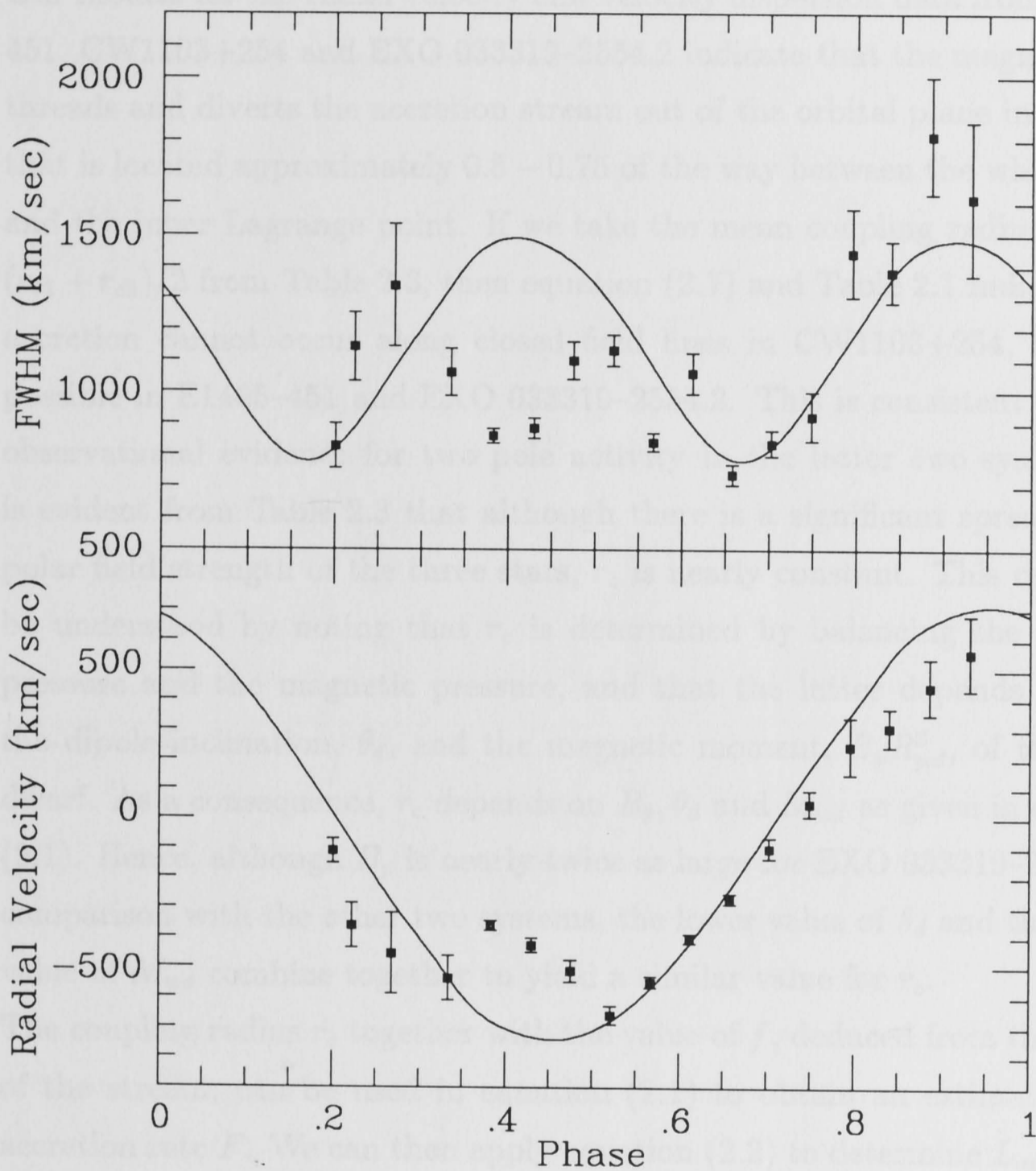


Figure 2.10: Application of Model to EXO 033319-2554.2
 Application of our model to the data for EXO 033319-2554.2 obtained by Ferrario *et al.* (1988). Lower panel: comparison between the observed broad emission line radial velocity (squares) and the model. Upper panel: comparison between the observed FWHM (squares) and the model. The discrepancy between the theoretical curves and the data between $\phi = 0.35 - 0.55$ for both the radial velocity and FWHM, is due to a partial eclipse of the line emission region (see Ferrario *et al.* 1988).

2.7 Discussion

Our models for the radial velocity and velocity dispersion data from E1405-451, CW1103+254 and EXO 033319-2554.2 indicate that the magnetic field threads and diverts the accretion stream out of the orbital plane in a region that is located approximately 0.5 – 0.75 of the way between the white dwarf and the inner Lagrange point. If we take the mean coupling radius as $r_c = (r_{c1} + r_{c2})/2$ from Table 2.3, then equation (2.7) and Table 2.1 indicate that accretion cannot occur along closed field lines in CW1103+254, but it is possible in E1405-451 and EXO 033319-2554.2. This is consistent with the observational evidence for two pole activity in the latter two systems. It is evident from Table 2.3 that although there is a significant spread in the polar field strength of the three stars, r_c is nearly constant. This result can be understood by noting that r_c is determined by balancing the gas ram pressure and the magnetic pressure, and that the latter depends on both the dipole inclination, θ_d , and the magnetic moment, $B_p R_{wd}^3$, of the white dwarf. As a consequence, r_c depends on B_p , θ_d and M_{wd} as given in equation (2.1). Hence, although B_p is nearly twice as large for EXO 033319-2554.2 in comparison with the other two systems, the lower value of θ_d and the higher value of M_{wd} combine together to yield a similar value for r_c .

The coupling radius r_c together with the value of f , deduced from the extent of the stream, can be used in equation (2.1) to obtain an estimate of the accretion rate F . We can then apply equation (2.2) to determine L_{acc} . A list of the quantities derived from our calculations is summarized in Table 2.3. For the case of CW1103+254 our estimate of the total accretion luminosity is about a factor 4 higher than that quoted, but we consider this acceptable, given the uncertainties in determining the total luminosity in AM Her systems (Beuermann, Stella and Krautter 1984).

The values of $f(R_{wd})$ deduced for the fractional area of the star over which accretion occurs are in the range $\approx 10^{-3} - 10^{-4}$, in agreement with the sizes

TABLE 2.3: DERIVED PARAMETERS

Output	E1405 - 451		CW1103 + 254	EXO 033319 - 2554.2
	(a)	(b)		
$r_{c1}(R_{wd})$	20	20	26	23
$r_{c2}(R_{wd})$	25	25	30	28
$B_{(rc)}$ (G)	1250	1450	900	1750
F ($g \cdot s^{-1}$)	5×10^{16}	6×10^{16}	2×10^{16}	8×10^{16}
L_{acc} ($erg \cdot s^{-1}$)	6×10^{33}	8×10^{33}	2×10^{33}	2×10^{34}
$f_{(rc)}$	2×10^{-2}	2×10^{-2}	7×10^{-3}	2×10^{-2}
$f_{R_{wd}}$	4×10^{-4}	4×10^{-4}	1×10^{-4}	4×10^{-4}

deduced for the optical and infrared cyclotron emission regions in the two eclipsing AM Her systems E1114+182 (Schmidt 1988), and EXO 023432-5232.3 (Bailey *et al.* 1988).

The values of r_c indicate that the material leaving the secondary star penetrates deep into the primary's magnetosphere, forcing accretion along non-polar magnetic field lines. Several investigators (Liebert and Stockman 1985; Lamb 1985; and Wickramasinghe 1988) have concluded that the broad emission line component is likely to originate from the magnetically channeled material. The model fits that we have achieved for individual systems tend to support this scenario. The optical and X-ray emission cannot be produced at the magnetic poles, but instead must originate from regions on the stellar surface that are offset by an angle which depends on the location of the threading region. Furthermore, since our calculations show that the accretion occurs over a very wide range of azimuthal angles, the cyclotron and X-ray emission regions cannot be point sources with cylindrical symmetry, but they must have the shape of an arc whose extension in longitude is much greater than in latitude. Beuermann, Stella and Patterson (1987) have been

led to the same conclusion by comparing the fluxes in the X-ray, optical and infrared for the system 2A0311 – 227 (=EF Eri). They deduce the presence of an “auroral arc” offset by about 20° – 25° from the magnetic pole with the cyclotron emission coming from a very wide region surrounding the small area where the hard X-rays are produced. The existence of an extended cyclotron emission region which is much larger than the X-ray region has been also proposed by Schmidt, Stockman and Grandi (1986), and Liebert and Stockman (1985).

There are other lines of evidence which suggest the presence of extended and structured emission regions which are displaced from the magnetic poles. The asymmetries observed in intensity and in the linear and circular polarization curves as a function of phase in most of the AM Her systems cannot be reproduced using standard point source models located at the magnetic poles. Recently, Wickramasinghe and Ferrario (1987,1988) have constructed models for extended cyclotron emission regions offset from the magnetic poles allowing for temperature and density structure. These models can explain the above asymmetries and at the same time better reproduce the observed wavelength dependence of intensity and polarization.

2.8 Conclusions

We have presented a theoretical model for the broad emission line component in AM Her systems. The model assumes that a dipolar magnetic field dominates the material flow close to the white dwarf, while at larger radii the material free falls radially towards the white dwarf surface. We have shown that with this model it is possible to locate the region where the broad emission lines are formed, using as constraints the radial velocity and velocity dispersion data for systems for which dipole and orbital inclinations can be estimated from other considerations.

The model provides an acceptable fit to the observations of the AM Her sys-

tems E1405-451, CW1103+254 and EXO 033319-2554.2. The main results of these calculations include the following. (1) The coupling region is much deeper in the magnetosphere than previously thought, with the material being threaded by field lines roughly 0.5 - 0.75 of the way between the white dwarf and the inner Lagrange point. (2) The accretion occurs over large azimuthal angles; (3) As a consequence of (1) and (2), the cyclotron emission region is expected to be extended and offset from the dipole axis.

Finally, we note that in order to better understand the accretion properties of the AM Her systems it is necessary to apply the model to other systems for which radial velocity and velocity dispersion data are available. Regretably however, observers tend not to publish dispersion data with their radial velocity measurements. Also, the separation of the different velocity components requires high resolution spectroscopy ($\Delta\lambda \lesssim 2 \text{ \AA}$) with a good signal to noise ratio. These factors limit the available database for the application of our model.

We would like to thank Mark Cropper and Gary Schmidt for helpful discussion. L.F. acknowledges support from an Australian National University postgraduate scholarship.

2.9 References

- Alfvén, H., and Falthämmar, C. 1963, "*Cosmical Electrodynamics*", (Oxford: Clarendon Press), p. 3.
- Bailey, J. 1985, Proc. ESA Workshop, "*Recent Results on Cataclysmic Variables*", Bamberg, **ESA sp-236**, 139.
- Bailey, J., Axon, D. J., Hough, J. H., Watts, D. J., Giles, A. B., Greenhill, J. G. 1983, *M.N.R.A.S.*, **205**, 1P.
- Bailey, J., Ferrario, L., Tuohy, I. R., Wickramasinghe, D. T., and Hough, J. H. 1987, *IAU Circ #* 4517.
- Bailey, J., Watts, D. J., Sherrington, M. R., Axon, D. J., Giles, A. B., Hanes, D. A., Heathcote, S. R., Hough, J. H., Hughes, S., Jameson, R. F., McLean, I. 1985, *M.N.R.A.S.*, **215**, 179.
- Bailey, J. A., Wickramasinghe, D. T., Hough, J., and Cropper, M. 1988, *M. N. R. A. S.*, submitted.
- Beuermann, K., Stella, L., and Krautter, J. 1984, *Proc. Symp. X-ray Astronomy 84*, Bologna, ed. Tanaka, p. 27.
- Beuermann, K., Stella, L., and Patterson, J. 1987, *Ap. J.*, **316**, 360.
- Beuermann, K., and Thomas, H. C. 1987, *IAU Circ #* 4486.
- Beuermann, K., Thomas, H. C., and Schwöpe, A. 1988, *Astr. Ap.*, **195**, L15.
- Berriman, G., and Smith, P. S. 1988, *Ap. J.*, **329**, L97.
- Cropper, M. 1986, *M. N. R. A. S.*, **218**, 201.
- Cropper, M. 1986, *M. N. R. A. S.*, **222**, 853.
- Cropper, M. 1988, *M. N. R. A. S.*, submitted.
- Cropper, M., Menzies, J. W., and Tapia, S. 1986, *M. N. R. A. S.*, **218**, 201.

- Ferrario, L., Wickramasinghe, D. T., Bailey, J. A., Tuohy, I. R., and Hough, J. H. 1988, *Ap. J.*, in press, (FWB).
- Ferrario, L., Wickramasinghe, D. T., and Tuohy, I. R. 1987, *Proc. Astron. Soc. of Australia*, **7**, 119.
- Giommi, P., Angelini, L., Osborne, J. P., Stella, L., and Tagliaferri, G. 1987, *IAU Circ # 4486*.
- Jensen, K.A., Nousek, J.A., and Nugent, J.J. 1982, *Ap. J.*, **261**, 625.
- Kopal, Z. 1959, "*Close Binary Systems*", (London: Chapman and Hall), p. 125.
- Lamb, D. Q. 1985, in "*Cataclysmic Variables and Low-Mass X-ray Binaries*", ed. D. Q. Lamb and J. Patterson (Dordrecht: Reidel), p. 179.
- Liebert, J., and Stockman, H. S. 1985, in "*Cataclysmic Variables and Low-Mass X-ray Binaries*", ed. D. Q. Lamb and J. Patterson (Dordrecht: Reidel), p. 151.
- Lubow, S. H., and Shu, F. H. 1975, *Ap. J.*, **198**, 383.
- Mukai, K., and Charles, P. A. 1987, *M. N. R. A. S.*, **226**, 209.
- Osborne, J. P., Giommi, P., Angelini, L., Tagliaferri, G., and Stella, L. 1988, *Ap. J. (Letters)*, in press.
- Rosen, S. R., Mason, K. O., and Córdova, F. A. 1986, *M. N. R. A. S.*, **224**, 987.
- Schmidt, G. D. 1988, Vatican Workshop, "*Polarized Radiation of Circumstellar Origin*", Ed. Coyne, G. V., Magalhaes, A. M., Moffat, A. F. J., Schulte-Ladbeck, R. E., Tapia, S., and Wickramasinghe, D. T., (Vatican Press), in press.
- Schmidt, G. D., Stockman, H. S., and Grandi, S. A. 1983, *Ap. J.*, **271**, 735, (SSG).
- Schmidt, G. D., Stockman, H. S., and Grandi, S. A. 1986, *Ap. J.*, **300**, 804.

- Stockman, H.S., Foltz, C.B., Schmidt, G.D., and Tapia, S. 1983, **271**, 725, (SFST).
- Tapia, S. 1982, *IAU Circ.*, # 3685.
- Tuohy, I. R., Visvanathan, N., and Wickramasinghe, D. T. 1985, *Ap. J.*, **289**, 721.
- Visvanathan, N., and Tuohy, I. R. 1983, *Ap. J.*, **275**, 709.
- Wickramasinghe, D. T. 1988, Vatican Workshop, Vatican Workshop, "*Polarized Radiation of Circumstellar Origin*", Ed. Coyne, G. V., Magalhaes, A. M., Moffat, A. F. J., Schulte-Ladbeck, R. E., Tapia, S., and Wickramasinghe, D. T., (Vatican Press), in press.
- Wickramasinghe, D.T., and Ferrario, L. 1987, *Proc. Astron. Soc. Aust.*, **7**, 123.
- Wickramasinghe, D.T., and Ferrario, L. 1988, *Ap. J.*, In press.
- Wickramasinghe, D. T., and Meggitt, S. M. A. 1985, *M. N. R. A. S.*, **216**, 857.
- Wickramasinghe, D.T., Tuohy, I.R., and Visvanathan, N. 1987, *Ap. J.*, **318**, 326.

Chapter 3

Cyclotron Emission from Inhomogeneous Shocks in AM Herculis Systems

3.1 Abstract

We discuss the properties of cyclotron radiation from accretion shocks located above the atmospheres of magnetic white dwarfs taking into account the effects of field spread, density and temperature structure and geometrical extension. The models are an improvement on previous point source models and have characteristics that are in better overall agreement with the properties of AM Herculis systems. The flat energy distributions seen in some AM Herculis systems are readily explained in terms of a model in which the optical depth parameter varies across the emission region in response to differences in the accretion rate. The lack of harmonic structure in the intensity spectra of most AM Herculis systems is probably a consequence of field spread in an extended emission region. We also show that the asymmetries seen in phase dependent polarization curves can be explained when allowance is made for the displacement of emission regions from the poles.

Subject headings: radiation mechanisms – shock waves – stars: binaries – stars: magnetic.

3.2 Introduction

It is now well established that the observations of AM Herculis systems can be explained at least qualitatively in terms of the properties of high harmonic cyclotron emission from a hot plasma ($T \approx 10 - 20$ keV) in a magnetic field of $2 - 3 \times 10^7$ G (Chanmugam and Dulk 1981; Meggitt and Wickramasinghe 1982, hereafter MW; Wickramasinghe and Meggitt 1985a, hereafter WM), Barrett and Chanmugam 1984, hereafter BC). However, attempts at detailed analysis of individual systems have in general met with limited success. We note in particular the failure of these models in explaining the wavelength dependence of intensity and polarization in AM Herculis itself and in explaining the asymmetries seen in broad band phase dependent intensity and polarization curves of most systems. With the exception of the analysis of V843 Cen (=E1405-451) by Wickramasinghe and Meggitt (1985b), previous attempts at modelling the observations have assumed either semi-infinite plane parallel (BC) or point source (WM) emission regions located at the diametrically opposite magnetic poles of a centred dipole field distribution. There is now considerable evidence which suggests that the emission regions are more extended and in general displaced from the magnetic poles (Cropper 1987; Beuermann, Stella and Patterson 1987; Ferrario, Wickramasinghe and Tuohy 1987; Piirola 1988; Schmidt 1988; Wickramasinghe 1988). In this paper we present results of new calculations on the properties of cyclotron emission regions which extend across and above the stellar surface allowing for field spread, density and temperature structure, and for displacement from the poles. We use our new models to discuss properties of AM Herculis systems which were previously inexplicable in terms of point source models.

3.3 Results and Discussion

3.3.1 The Models

The models have been constructed as follows.

(1.) We assume that the emission region has a variable height above the stellar surface and extends over a spherical cap which subtends an angle 2α at the centre of the star. The direction \vec{l}_p of the centre of the polar cap with respect to the centre of the star makes an angle Δ with respect to the direction of the spin axis \vec{l}_s (Figure 3.1a).

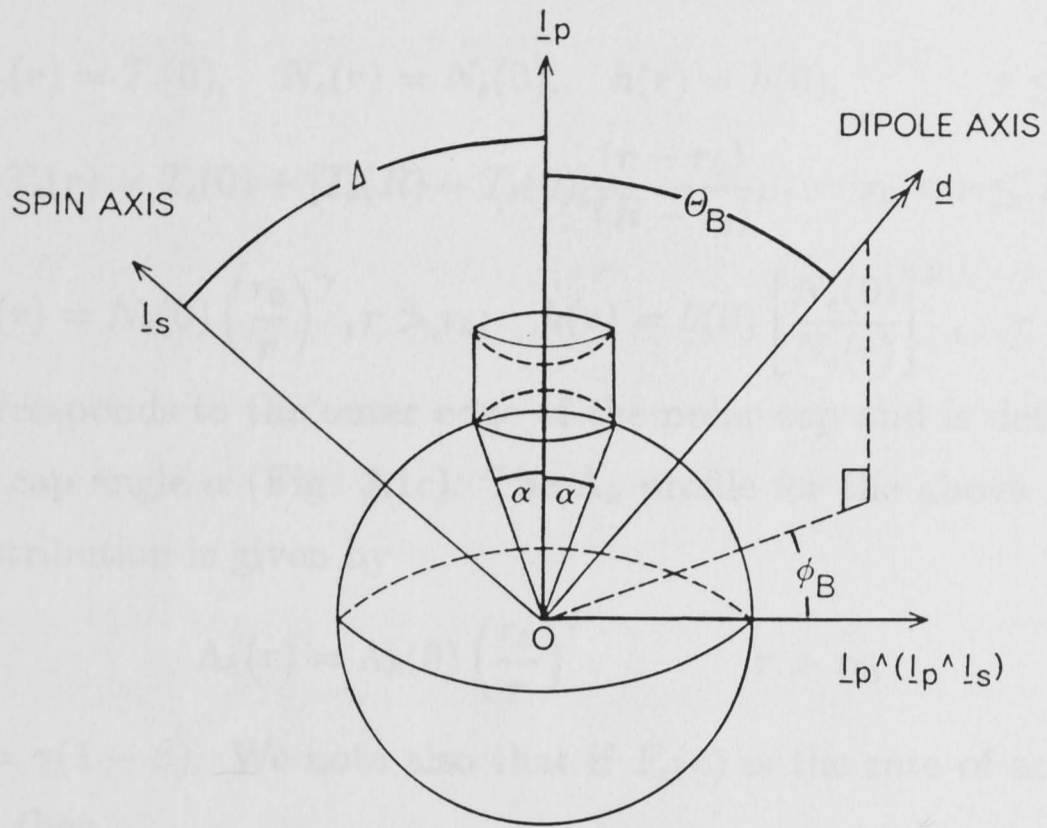
(2.) The field geometry is that of a centred dipole. The direction of the dipole axis \vec{d} has polar angle θ_B with respect to \vec{l}_p and azimuthal angle ϕ_B with respect to a line perpendicular to \vec{l}_p in the same plane as \vec{l}_p and \vec{l}_s ; that is, in the direction $\vec{l} \wedge (\vec{l}_p \wedge \vec{l}_s)$ (Figure 3.1a).

The models are divided into two groups. In the first group, we examine the effects of field variations and geometrical extent (§3.3.2 - §3.3.3) and construct models assuming uniform electron temperature T_e and electron number density N_e . The emission regions in these models have a constant radial thickness H (Figure 3.1b) and are characterized by the optical depth parameter (MW),

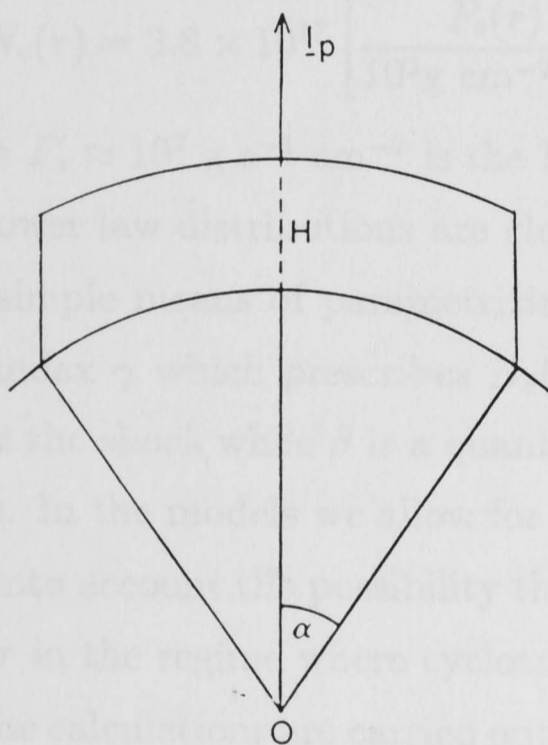
$$\Lambda_H = 2.01 \times 10^8 \left(\frac{H}{10^8 \text{cm}} \right) \left(\frac{N_e}{10^{16} \text{cm}^{-3}} \right) \left(\frac{3 \times 10^7 \text{G}}{B} \right),$$

in the radial direction. Clearly Λ_H varies over the emission region due to changes in B . For the purposes of labelling the models we evaluate Λ_H by using the polar field strength B_p .

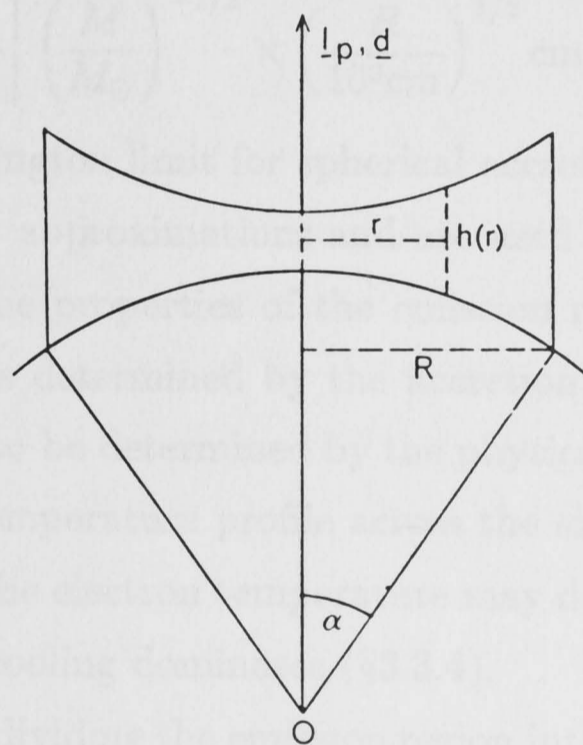
In the second group we examine the effects of temperature and density structure (§3.3.4). The emission region is assumed to be centred at the magnetic pole ($\theta_B = \phi_B = 0^\circ$). The electron temperature T_e , electron number density N_e , and shock height h above the surface parallel to \vec{l}_p are prescribed as functions of r , the perpendicular distance from the central axis \vec{l}_p of the



(a)



(b)



(c)

Figure 3.1: Model Geometry

(a) The orientation of the dipole axis \vec{d} and spin axis \vec{l}_s relative to the symmetry axis \vec{l}_p of the emission region. (b)–(c) are the cross-sections of the emission regions through the axis of symmetry \vec{l}_p for the two geometries described in the text.

polar cap, as follows

$$T_e(r) = T_e(0), \quad N_e(r) = N_e(0), \quad h(r) = h(0), \quad r \leq r_0;$$

$$T_e(r) = T_e(0) + [T_e(R) - T_e(0)] \frac{(r - r_0)}{(R - r_0)}, \quad r_0 < r \leq R;$$

$$N_e(r) = N_e(0) \left(\frac{r_0}{r}\right)^\gamma, \quad r > r_0; \quad h(r) = h(0) \left[\frac{N_e(0)}{N_e(r)}\right]^\beta, \quad r > r_0;$$

$r = R$ corresponds to the outer edge of the polar cap and is determined by the polar cap angle α (Fig. 3.1c). The Λ_h profile for the above density and height distribution is given by

$$\Lambda_h(r) = \Lambda_h(0) \left(\frac{r_0}{r}\right)^\delta, \quad r > r_0,$$

where $\delta = \gamma(1 - \beta)$. We note also that if $F_s(r)$ is the rate of accretion per unit area, then

$$N_e(r) = 3.8 \times 10^{17} \left[\frac{F_s(r)}{10^{22} \text{ g cm}^{-2} \text{ s}^{-1}} \right] \left(\frac{M}{M_\odot} \right)^{-1/2} \times \left(\frac{R}{10^9 \text{ cm}} \right)^{1/2} \text{ cm}^{-3},$$

where $F_s \approx 10^{22} \text{ g s}^{-1} \text{ cm}^{-2}$ is the Eddington limit for spherical accretion.

Power law distributions are clearly approximations and are used merely as a simple means of parametrizing the properties of the emission regions. The index γ which prescribes $N_e(r)$ is determined by the accretion profile across the shock while β is a quantity to be determined by the physics of the shock. In the models we allow for a temperature profile across the shock to take into account the possibility that the electron temperature may decrease with r in the regime where cyclotron cooling dominates (§3.3.4).

The calculations are carried out by dividing the emission region into plane parallel slabs, which are parallel to the line of sight \vec{l} , and solving the polarized transfer equations by following individual rays through each slab allowing for field, temperature and density variations. The solution along each ray is obtained by dividing the total path length into sufficiently small subintervals to allow B , T and N_e to be taken as constant in each interval. The transfer equations in the Stokes formulation are then solved for each elementary path length using the analytical solutions to the transfer equations given

by MW for constant conditions, taking care to rotate to the appropriate field direction dependent coordinate system at each step. Cyclotron and free-free opacities are included in the calculations as in MW and WM respectively.

The first group of models are somewhat similar to the extended polar cap models for DQ Her systems published recently by Chanmugam and Frank (1987), but the basic assumptions and parameter range considered are different. We note in particular that they do not allow for extension above the stellar surface and have not included free-free emission, which could be dominant at high harmonics and at low angles to the magnetic field (WM). Furthermore, their calculations have been restricted to conditions appropriate to DQ Herculis variables (large polar caps). In the region of overlap we find good agreement between the two sets of calculations.

3.3.2 *General Properties of Extended Emission Regions*

We consider a uniform temperature and density model with $B_p = 3.2 \times 10^7$ G, $T_e = 20$ keV, $N_e = 1.0 \times 10^{16}$ cm⁻³ corresponding to a size parameter $\Lambda_H = 2.0 \times 10^6$ in the radial direction. We have chosen these parameters to correspond to the values of Λ that have previously been determined from high temperature fits of point source models to the optical data of AM Herculis systems. The calculations are for viewing angles $i = 80^\circ$ and 40° (Fig. 3.2) with respect to the direction \vec{l}_p and for polar cap sizes $\alpha = 0.1^\circ, 10^\circ$, and 40° . The harmonic numbers ω/ω_c are calculated for the polar field strength B_p . For $i = 80^\circ$, the emission region is partially eclipsed by the body of the white dwarf for $\alpha > 10^\circ$, while for $i = 40^\circ$, most of the emission region is visible for all polar cap sizes that have been considered.

We consider the models with $i = 80^\circ$ but the results for $i = 40^\circ$ can be similarly interpreted. For $\alpha < 10^\circ$ the intensity and polarization spectra are insensitive to polar cap size. Major differences occur in the intensity and polarization spectra as α is increased above 10° . We note in particular (1) the shift of the frequency ω^* corresponding to maximum I_ω to lower

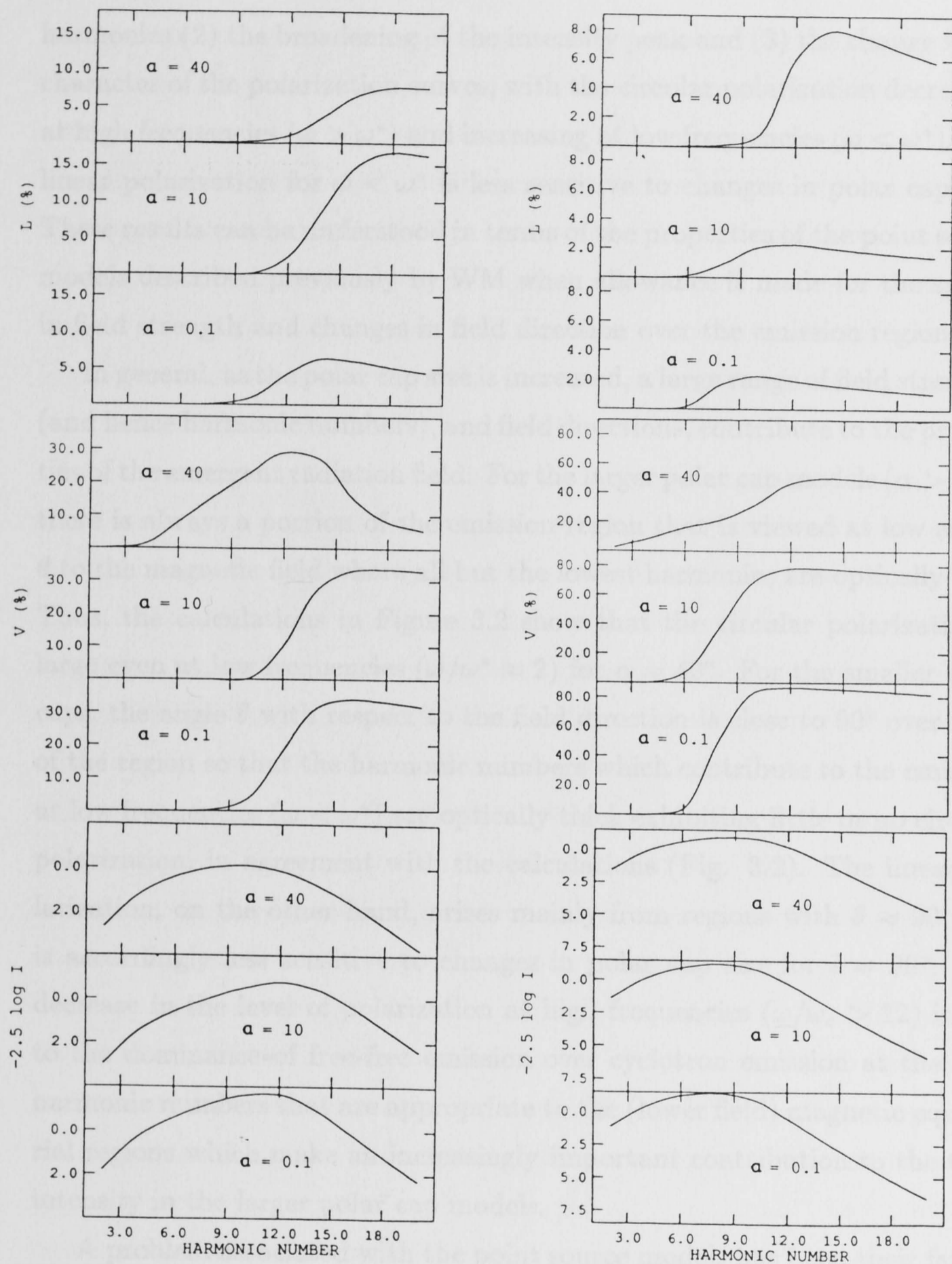


Figure 3.2: Polarization and Intensity Behavior

Left panel: The intensity ($-2.5 \log I_\omega$), circular and linear polarization spectra for models with uniform temperature and density with parameters $B_p = 3.2 \times 10^7$ G, $T_e = 20$ keV, $N_e = 1.0 \times 10^{16}$ cm $^{-3}$, $\Lambda_H = 2.0 \times 10^6$. The viewing angle $i = 80^\circ$ is measured with respect to the symmetry axis \vec{l}_p and the spot is centred at a magnetic pole. The models correspond to different polar cap sizes α . Right panel: Same as left panel but for $i = 40^\circ$.

harmonics (2) the broadening of the intensity peak and (3) the change in the character of the polarization curves, with the circular polarization decreasing at high frequencies ($\omega > \omega^*$) and increasing at low frequencies ($\omega < \omega^*$). The linear polarization for $\omega < \omega^*$ is less sensitive to changes in polar cap size. These results can be understood in terms of the properties of the point source models described previously by WM when allowance is made for the spread in field strength and changes in field direction over the emission region.

In general, as the polar cap size is increased, a large range of field strengths (and hence harmonic numbers), and field directions, contribute to the properties of the emergent radiation field. For the larger polar cap models ($\alpha > 10^\circ$), there is always a portion of the emission region that is viewed at low angles θ to the magnetic field where all but the lowest harmonics are optically thin. Thus, the calculations in Figure 3.2 show that the circular polarization is large even at low frequencies ($\omega/\omega^* \approx 2$) for $\alpha = 40^\circ$. For the smaller polar caps, the angle θ with respect to the field direction is close to 90° over most of the region so that the harmonic numbers which contribute to the emission at low frequencies ($\omega < \omega^*$) are optically thick exhibiting little or no circular polarization, in agreement with the calculations (Fig. 3.2). The linear polarization, on the other hand, arises mainly from regions with $\theta \approx 90^\circ$ and is accordingly less sensitive to changes in polar cap size for $i = 80^\circ$. The decrease in the level of polarization at high frequencies ($\omega/\omega_c > 12$) is due to the dominance of free-free emission over cyclotron emission at the high harmonic numbers that are appropriate to the (lower field) magnetic equatorial regions which make an increasingly important contribution to the total intensity in the larger polar cap models.

A problem associated with the point source models has been their failure in predicting significant polarization at low harmonics in the spectral region where I_ω increases with ω (The "optically thick region" in point source models). The point source models predict an unpolarized Rayleigh Jeans-type black body spectrum ($I_\omega \propto \omega^2$) at optically thick frequencies and a strongly polarized and steeply declining spectrum ($I_\omega \omega^{-p}, p \gg 1$) at the higher, op-

tically thin frequencies similar to the small polar cap models in Figure 3.2. Simultaneous optical and IR observations by Bailey *et al.* (1983) of systems such as E1405-451 have, on the other hand, shown significant polarization in the blue (V) and the red (H) bands corresponding to high and low harmonics numbers. We note in this context that extended polar cap models have the interesting property of predicting significant polarization at low harmonics, but only for sufficiently large polar cap sizes ($\alpha > 20^\circ$). We will show in §3.3.4 that under suitable conditions, models with temperature and density structure also predict polarization at low harmonics.

Cyclotron features have been seen in VV Puppis during the bright phase when the system is in an intermediate state of activity [$m_v(\text{max}) \approx 16 - 16.5$] with only one pole dominating in the optical (Visvanathan and Wickramasinghe 1979). Although special conditions are required for the visibility of cyclotron harmonics (large viewing angles $\theta \approx 70^\circ - 90^\circ$ with respect to magnetic field, low temperatures $T_e \approx 10$ keV, low optical depths $\Lambda \approx 10^5$ at 10 keV), the absence of these features in the optical in other systems with similar viewing geometry and in VV Puppis during its active state is not easy to explain. One possibility, which has so far not been investigated, is that magnetic field broadening renders the features undetectable. We have calculated extended polar cap models with uniform temperature and density for the parameters $B_p = 3.2 \times 10^7$ G, $T_e = 10$ keV, $\Lambda_H = 1.0 \times 10^5$ deduced previously by Wickramasinghe and Meggitt (1982) using point source models and the cyclotron spectrum of VV Puppis. The results are shown in Figure 3.3. It follows that polar caps with $\alpha \geq 20^\circ$ are required before the cyclotron features can be washed out by field spread at $T_e = 10$ keV and that even larger polar caps will be required at lower temperatures. We note that the lowest harmonics remain detectable even at $\alpha = 20^\circ$.

The cyclotron harmonics can also be rendered undetectable by an increase in optical depth (increase in Λ_H) at $T_e = 10$ keV or by an increase in temperature ($T_e > 10$ keV) in response to an increase in accretion rate which causes the shock to change from being mainly cyclotron cooling dominated

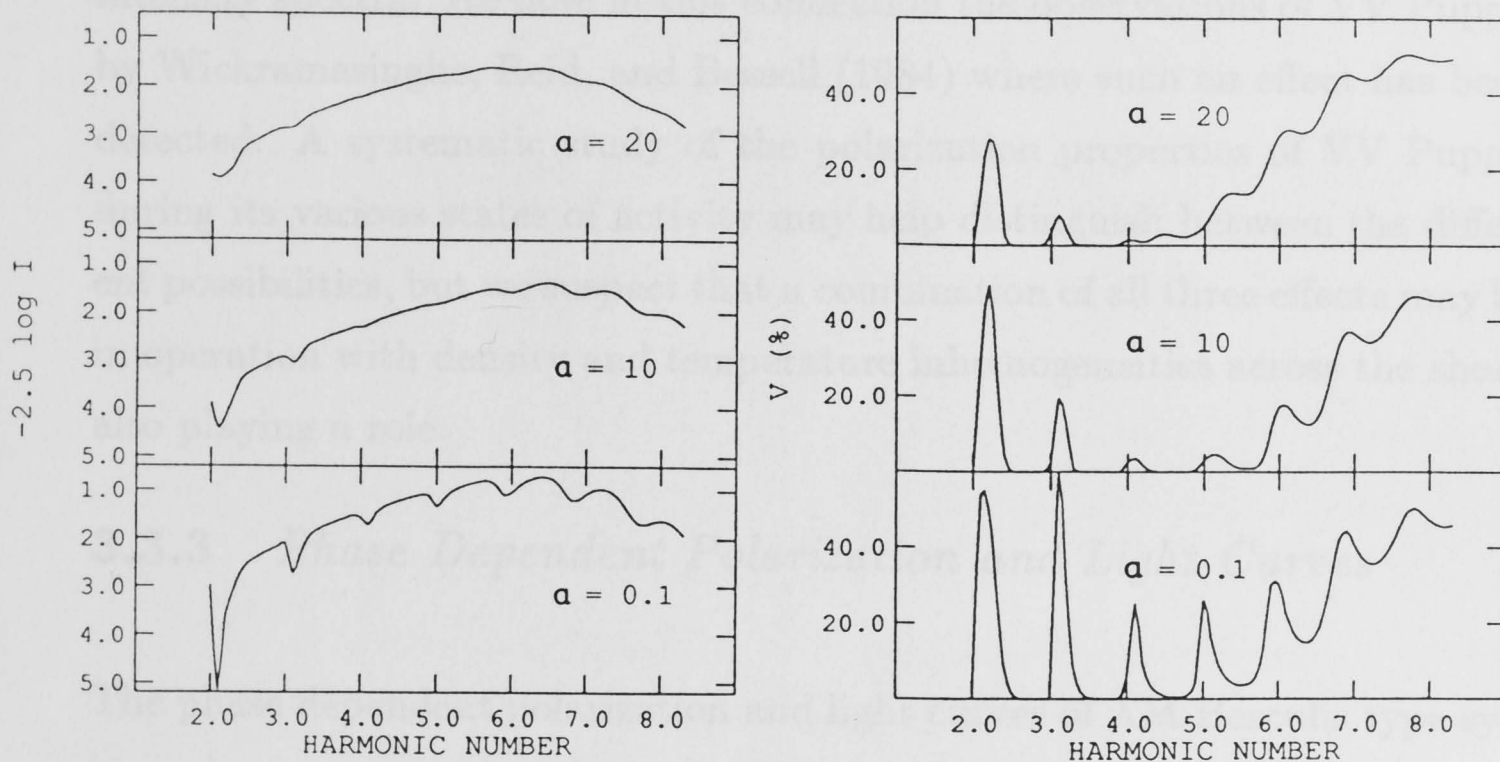


Figure 3.3: Harmonic Visibility as a Function of Polar Cap Size
 The intensity ($-2.5 \log I_\omega$) (left panel) and the circular polarization (right panel) spectra for models with uniform temperature and density with parameters $B_p = 3.2 \times 10^7$ G, $T_e = 10$ keV, $N_e = 1.0 \times 10^{15}$ cm $^{-3}$, $\Lambda_H = 1.0 \times 10^5$. The viewing angle $i = 80^\circ$ is measured with respect to the symmetry axis \vec{l}_p and the spot is centred at a magnetic pole. The models correspond to different polar cap sizes α .

to free-free cooling dominated. In the former case, we expect the degree of circular polarization to significantly decrease during a high state when the harmonics are not seen, which appears to be contrary to observations. On the other hand, the polar cap model predicts significant circular polarization even when the features have been washed out due to field spread (Fig. 3.3). They also show that cyclotron harmonics may be detectable in the circular polarization spectra even when the features are not apparent in the intensity spectra. We note in this connection the observations of VV Puppis by Wickramasinghe, Reid, and Bessell (1984) where such an effect has been detected. A systematic study of the polarization properties of VV Puppis during its various states of activity may help distinguish between the different possibilities, but we suspect that a combination of all three effects may be in operation with density and temperature inhomogeneities across the shock also playing a role.

3.3.3 *Phase Dependent Polarization and Light Curves*

The phase dependent polarization and light curves of AM Herculis type systems show asymmetries which are inconsistent with the standard assumption that the emission regions are point sources located at the magnetic poles of a centred dipole field distribution. Large asymmetries have been noted even in cases where the radiation is known to originate from a single emission region.

Our polar cap models provide a possible interpretation of some of the asymmetries seen in these systems if we assume that the emission region is displaced from the position of the magnetic pole. Consider the properties of a system such as VV Puppis or ST Leo Mi (=CW1103+254) which has an eclipsing cyclotron emission region. We have constructed models for such a system by assuming an inclination $i = 75^\circ$, colatitude $\Delta = 150^\circ$ for the position of the centre of the spot, and shock parameters $B_p = 3.2 \times 10^7$ G, $T_e = 10$ keV, $\Lambda_H = 1.0 \times 10^5$ consistent with the previous analysis of VV

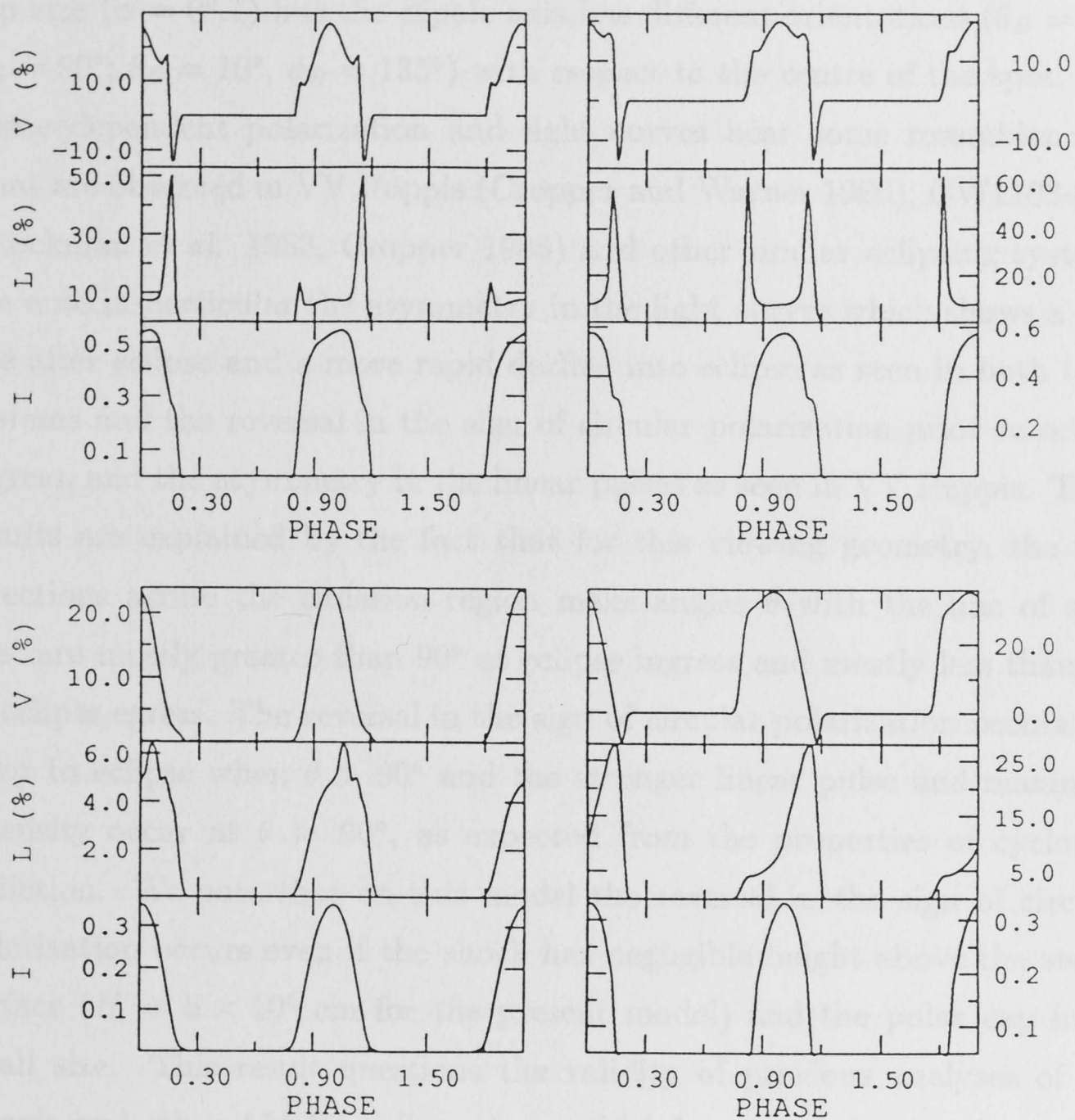


Figure 3.4: Phase Dependent Polarization and Light curves
Phase dependent intensity and polarization curves for emission regions which are centred at latitude $\Delta = 150^\circ$ and which are displaced from the magnetic pole. The orbital inclination $i_{orb} = 75^\circ$ and $\omega/\omega_c = 6.2$. The emission region has the same physical parameters as in Figure 3.3. The models correspond to different polar cap sizes (α) and displacements (θ_B, ϕ_B) of the dipolar axis; (a) (top left) $\alpha = 0.1^\circ, \theta_B = 10^\circ, \phi_B = 90^\circ$, (b) (top right) $\alpha = 0.1^\circ, \theta_B = 10^\circ, \phi_B = 135^\circ$, (c) (bottom left) $\alpha = 10^\circ, \theta_B = 10^\circ, \phi_B = 90^\circ$, and (d) (bottom right) $\alpha = 10^\circ, \theta_B = 30^\circ, \phi_B = 90^\circ$.

Puppis (Fig. 3.4). The models in Figures 3.4*a* and 3.4*b* have the same polar cap size ($\alpha = 0^\circ.1$) but the dipole axis has different orientations ($\theta_B = 10^\circ$, $\phi_B = 90^\circ$; $\theta_B = 10^\circ$, $\phi_B = 135^\circ$) with respect to the centre of the spot. The phase dependent polarization and light curves bear some resemblance to what are observed in VV Puppis (Cropper and Warner 1986), CW1103+254 (Stockman *et al.* 1983, Cropper 1985) and other similar eclipsing systems. We note in particular the asymmetry in the light curves which shows a slow rise after eclipse and a more rapid decline into eclipse as seen in both these systems and the reversal in the sign of circular polarization prior to eclipse ingress, and the asymmetry in the linear pulses as seen in VV Puppis. These results are explained by the fact that for this viewing geometry, the field directions across the emission region make angles θ with the line of sight that are mostly greater than 90° at eclipse ingress and mostly less than 90° at eclipse egress. The reversal in the sign of circular polarization occurs just prior to eclipse when $\theta > 90^\circ$ and the stronger linear pulse and maximum intensity occur at $\theta \approx 90^\circ$, as expected from the properties of cyclotron radiation. We note that on this model the reversal in the sign of circular polarization occurs even if the shock has negligible height above the stellar surface ($H = 5 \times 10^5$ cm for the present model) and the polar cap has a small size. This result questions the validity of previous analyses of VV Puppis and other AM Herculis systems which have used the duration of the polarization reversal to estimate the height of the shock above the stellar surface. We emphasize that the characteristics of the polarization curves depend critically on ϕ_B for a given α and θ_B . For instance, for $\phi_B = 0^\circ$ there are no polarization reversals (as in CW1103+254) while for $\phi_B = 180^\circ$ there are two symmetrical reversals at eclipse ingress and egress (not shown).

A closer comparison with the observations of VV Puppis and CW1103+254 shows that the rise in intensity after eclipse egress is more gradual and the secondary pulse broader than predicted by the theory. Models with larger values of α show that the basic flat topped character of the circular polarization curves is lost for $\alpha \geq \phi_B$. This is illustrated by the

models in Figure 3.4c ($\theta_B = 10^\circ, \phi_B = 90^\circ, \alpha = 10^\circ$) which predict circular polarization and intensity curves which are sinusoidal in character, contrary to what is observed. Large asymmetries can occur in the polarization curves with large polar caps, but only if the angular displacement θ_B from the pole is considerably larger than the angular extent of the emission region ($\theta_B \gg \alpha$). This is illustrated in Figure 3.4d ($\theta_B = 30^\circ, \phi_B = 90^\circ, \alpha = 10^\circ$). Although the pulse shape and circular polarization curves are similar to what are observed in VV Puppis, the light curve is too sinusoidal.

Our models have shown that the observed polarization characteristics of eclipsing cyclotron emission regions are similar to what is expected from emission regions that are extended and displaced from the magnetic poles. However, it appears that models with cylindrical symmetry may not be capable of reproducing the intensity and polarization observations in detail. Preliminary estimates indicate that an arc-like emission region which has considerable angular extent ($\approx 20^\circ$) over the surface and with an angular width of $\approx 1^\circ - 2^\circ$ will have spectropolarimetric properties that are qualitatively similar to those of large polar caps ($\alpha = 20^\circ$) and at the same time produce large asymmetries in both the intensity and polarization curves as required by observations. Observational evidence for arc-like emission regions has been presented by Beuermann, Stella, and Patterson (1987) and Cropper (1987).

The recent evidence for two pole emission in AM Herculis systems (Pirolo 1988; Ferrario, Wickramasinghe and Tuohy 1988; Wickramasinghe 1988; Meggitt and Wickramasinghe 1988) has introduced a further complication which must be considered in interpreting the polarization data. Thus, in VV Puppis, the reversal in the sign of circular polarization which lasts for the entire faint phase and which is present only when the system is in an active state, can be attributed to a second emission region on the white dwarf surface. In this system, the two emission regions are simultaneously visible for only a small fraction of the rotational phase although in other systems (*e.g.* AM Herculis) there could be considerable phase overlap (Meggitt and

Wickramasinghe 1988, Wickramasinghe 1988). The simultaneous visibility of more than one emission region could introduce additional asymmetries into the light and polarization curves.

3.3.4 *Density and Temperature Structure*

The possible importance of temperature structure within the shock front in a direction perpendicular to the shock was discussed by Meggitt and Wickramasinghe (1984). Liebert and Stockman (1985), Schmidt, Stockman, and Grandi (1986), and Stockman and Lubenow (1987) have considered the effects of density structure across the stellar surface in the post shock region which could result from varying rates of accretion along different field lines but no detailed models have been constructed. We have modeled this possibility in the framework of a polar cap emission region allowing also for temperature variations (§3.3.1). Results of a typical set of calculations for a polar cap with $\alpha = 1^\circ$ are presented in Figures 3.5 and 3.6. The models have a central high density region with radius $r_0 = 0.1R$ and uniform conditions specified by $T_e(0) = 20$ keV, $N_e(0) = 10^{18}$ cm $^{-3}$ and $\Lambda_h(0) = 2.0 \times 10^8$ and an outer region with a Λ profile defined by the indices β and γ . The value adopted for $\Lambda_h(0)$ is consistent with what is expected for the standard model of a free-free dominated shock (Lamb and Masters 1979). The solid curves correspond to models with a uniform temperature [$T_e(R) = T_e(0) = 20$ keV]. The dashed curves correspond to a model with a temperature distribution that declines linearly with radius in the outer region [$T_e(R) = 10$ keV; Fig. 3.5]. For fixed $\Lambda_h(0)$, r_0/R and temperature structure, the characteristics of the spectra depend only on the index $\delta = \gamma(1 - \beta)$ and not on the individual values of β or γ [$\Lambda_h(r) \propto r^{-\delta}$].

We note that flat energy distributions which show polarization over a significant range of harmonics occur in models with $\delta \approx 4 - 6$. For fixed δ , the model with the declining temperature distribution gives an even flatter energy distribution. The effect of changing the viewing angle i in the constant

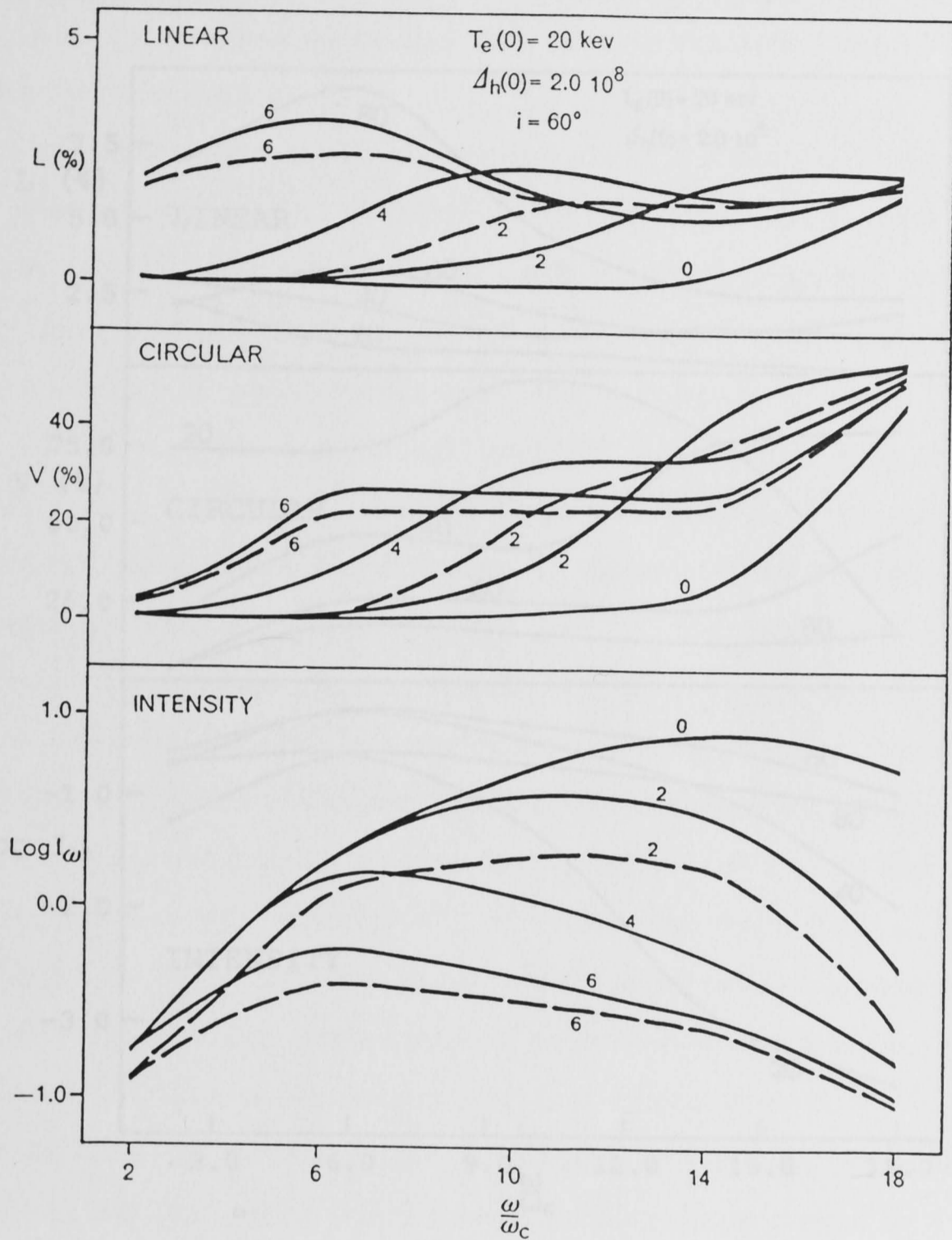


Figure 3.5: Intensity and Polarization Curves for Structured Models
 The intensity ($\log I_\omega$) and polarization curves for models with temperature and density structure. The viewing angle $i = 60^\circ$ is measured with respect to the symmetry axis \vec{l}_p and the spot is centred at a magnetic pole. The model parameters are described in the text. The curves are labelled by the index δ [$\Lambda_h(r) \propto r^\delta(r - r_0)$]. The dashed curves have temperature structure in addition to density structure.

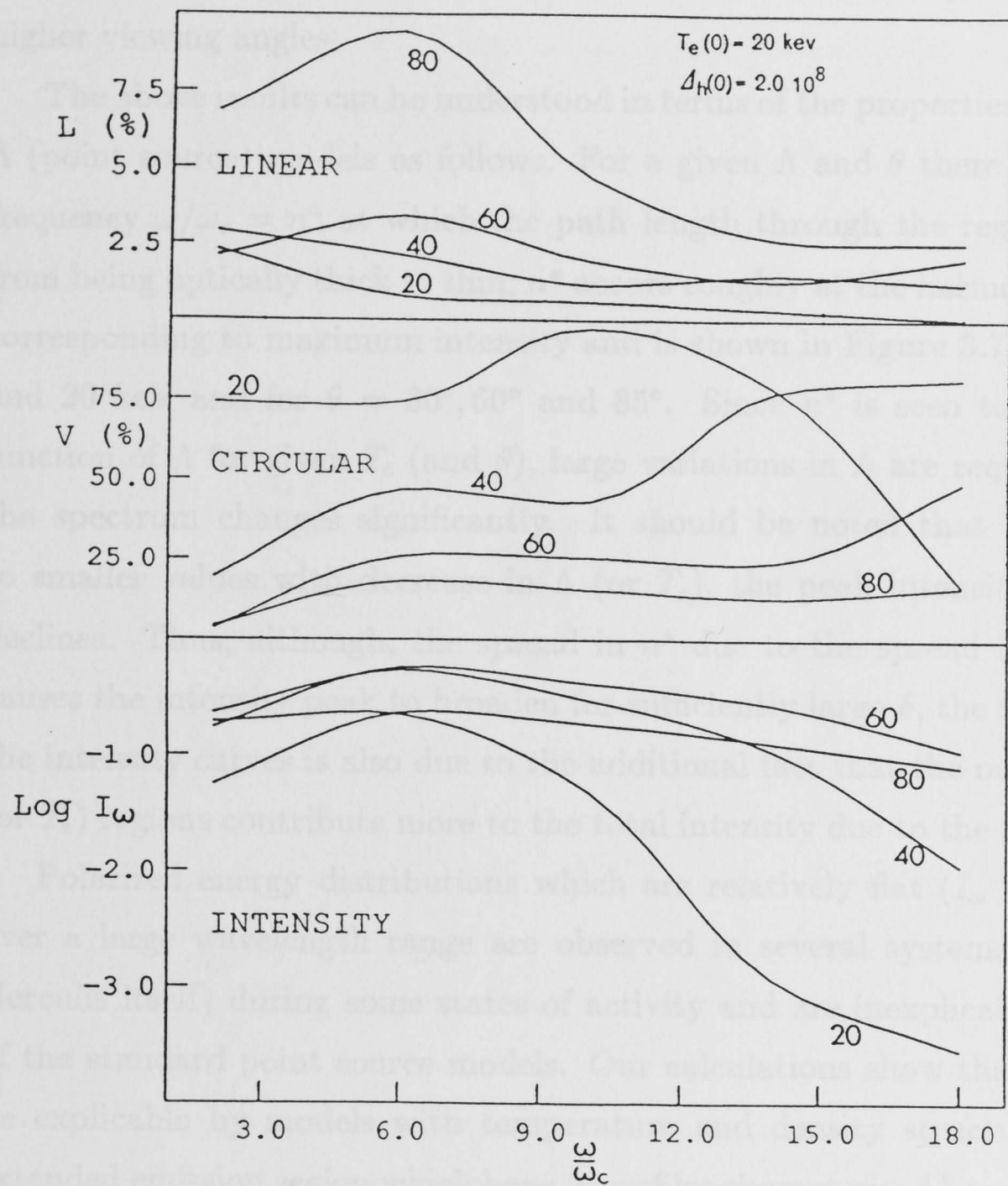


Figure 3.6: Intensity and Polarization Curves at different i . The intensity ($\log I_\omega$) and polarization curves for the uniform temperature model with $\delta = 6$ in Fig. 3.5 at different viewing angles i with respect to the dipolar axis.

temperature model with $\delta = 6$ is illustrated in Figure 3.6. The energy distributions are seen to be flat over a more extended frequency range at higher viewing angles.

The above results can be understood in terms of the properties of constant Λ (point source) models as follows. For a given Λ and θ there is a critical frequency $\omega/\omega_c = n^*$ at which the path length through the region changes from being optically thick to thin; n^* occurs roughly at the harmonic number corresponding to maximum intensity and is shown in Figure 3.7 for $T_e = 10$ and 20 keV and for $\theta = 30^\circ, 60^\circ$ and 85° . Since n^* is seen to be a weak function of Λ for given T_e (and θ), large variations in Λ are required before the spectrum changes significantly. It should be noted that as n^* shifts to smaller values with decrease in Λ (or T_e), the peak intensity $I_{n^*\omega_c}$ also declines. Thus, although, the spread in n^* due to the spread in Λ (or T_e) causes the intensity peak to broaden for sufficiently large δ , the flattening of the intensity curves is also due to the additional fact that the outer lower Λ (or T_e) regions contribute more to the total intensity due to the area effect.

Polarized energy distributions which are relatively flat ($I_\omega \approx \omega^0 - \omega^1$) over a large wavelength range are observed in several systems (*e.g.* AM Herculis itself) during some states of activity and are inexplicable in terms of the standard point source models. Our calculations show that they may be explicable by models with temperature and density structure over an extended emission region which have Λ profiles characterised by a large value of δ .

It is interesting to note that structured models tend to show a lower level of circular polarization in comparison to uniform (point source) models. This results from the fact that the emission from the optically thicker weakly polarized central regions dilutes the radiation from the optically thinner outer regions resulting in a net decrease in the degree of polarization in the flat part of the spectrum. The low value of circular polarization at high harmonics in the model with $i = 20^\circ$ is due to the dominance of free-free emission. The possibility that polarization may be reduced due to structure within

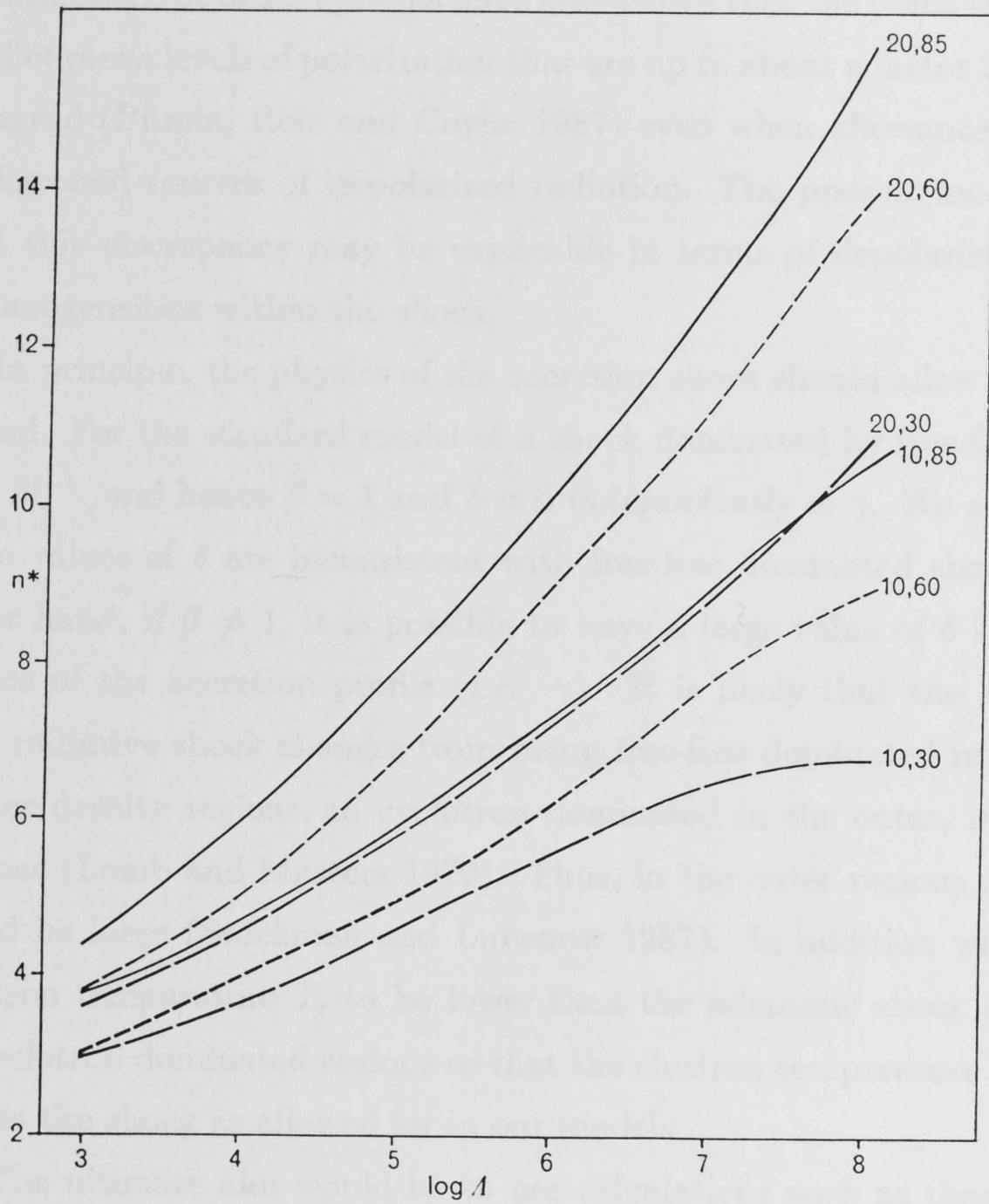


Figure 3.7: Harmonic Number Dependence on Model Parameters
 The dependence of the harmonic number n^* on the optical depth parameter Λ , electron temperature T_e , and viewing angle θ with respect to field direction, for point source models. The curves are labelled by (T_e, θ) .

the shock region was first noted by Wickramasinghe and Meggitt (1982) in connection with their analysis of the observations of VV Puppis. Recent investigations of other systems have also shown that the point source models predict mean levels of polarization that are up to about a factor 2 higher than observed (Piirola, Reiz and Coyne 1987) even when allowance is made for background sources of unpolarized radiation. The present models indicate that this discrepancy may be explicable in terms of depolarization due to inhomogeneities within the shock.

In principle, the physics of the accretion shock should allow β to be estimated. For the standard model of a shock dominated by free-free radiation $h \propto N_e^{-1}$, and hence $\beta = 1$ and $\delta = 0$ *independently* of γ . We conclude that large values of δ are inconsistent with free-free dominated shocks. On the other hand, if $\beta \neq 1$, it is possible to have a large value of δ by a suitable choice of the accretion profile (*i.e.* γ). It is likely that the shock region in a radiative shock changes from being free-free dominated in the central, higher density regions, to cyclotron dominated in the outer, lower density regions (Lamb and Masters 1979). Thus, in the outer regions $\beta \neq 1$ and δ could be large (Stockman and Lubenow 1987). In addition we expect the electron temperature T_e to be lower than the adiabatic shock temperature in cyclotron dominated regions so that the electron temperature may decline across the shock as allowed for in our models.

The ultimate aim would be to use calculations such as those presented here to determine the accretion profiles across the emission regions from spectropolarimetric observations. Such a procedure will have to await a more detailed understanding of the properties of accretion shocks. The recent calculations of Stockman and Lubenow (1987) are clearly an important step in this direction. However, it is not clear at present whether non standard shock models such as those proposed by Kuijpers and Pringle (1982) may also have to be considered.

3.4 Conclusions

We have investigated the effects of field spread and of temperature and density structure across the emission regions of AM Herculis systems and compared our results with predictions from previous point source models. We find that field spread within the cyclotron emission region can significantly affect the intensity and polarization spectra but only for polar caps of angle $\alpha \geq 20^\circ$. In particular, the models predict circular polarization at low harmonics where the equivalent point source models predict zero polarization. The calculations also show that the cyclotron harmonics expected in the visible region will be rendered undetectable due to field spread for polar caps with $\alpha \geq 20^\circ$.

Larger changes occur in models which have temperature and density structure (assumed axisymmetric) across the emission region. We have shown that such regions can be characterized by "Λ profiles" [$\Lambda(r) \propto r^{-\delta}$] and temperature profiles across the shock. Under certain conditions ($\delta \approx 4-6$), these models show intensity spectra which are flat and polarized over a large range of harmonics as required by the observations of some AM Herculis variables.

Finally, we have shown that the asymmetries which are seen in the polarization and light curves of AM Herculis systems are qualitatively similar to what is calculated for axisymmetric emission regions that are displaced from the magnetic poles. Although these models are an improvement on previous point source models where the emission region was assumed to be centred at a pole, it is already clear that non axisymmetric geometrical structures will have to be considered before detailed agreement can be achieved with observations. The results of such calculations will be discussed in a subsequent paper where fits to individual systems will be presented. (Ferrario and Wickramasinghe 1988).

One of us (L.F.) acknowledges support from an Australian National University post graduate scholarship.

3.5 References

- Bailey, J., Axon, D.J., Hough, J.H., Watts, D.J., Giles, A.B., and Greenhill, J.G. 1983, *M. N. R. A. S.*, **205**, 1p.
- Barrett, P.E. and Chanmugam, G. 1984, *Ap. J.*, **278**, 298, (BC).
- Beuermann, K., Stella, L. and Patterson, J. 1987, *Ap. J.*, **316**, 360.
- Chanmugam, G. and Dulk, G. 1981, *Ap. J.*, **242**, 569.
- Chanmugam, G. and Frank, J. 1987, *Ap. J.*, **320**, 746.
- Cropper, M. 1986, *M. N. R. A. S.*, **222**, 853.
- Cropper, M. 1987, *M. N. R. A. S.*, **228**, 389.
- Cropper, M. and Warner, B. 1986, *M. N. R. A. S.*, **220**, 633.
- Ferrario, L., Wickramasinghe, D.T. and Tuohy, I. 1988, submitted.
- Ferrario, L. and Wickramasinghe, D.T. 1988, in preparation.
- Kuijpers, and Pringle, J.E 1982, *Astr. Ap.*, **114**, L4.
- Lamb, D.Q. and Masters, A.R. 1979, *Ap. J. (Letters)*, **234**, L117.
- Liebert, J. and Stockman, H.S. 1985, in *Cataclysmic Variables and Low Mass X-ray binaries*, ed. J. Patterson and D.Q. Lamb (Cambridge: Reidel), p. 151.
- Meggit, S.M.A., and Wickramasinghe, D.T. 1982, *M. N. R. A. S.*, **198**, 71 (MW).
- Meggit, S.M.A. and Wickramasinghe, D.T. 1984, *M. N. R. A. S.*, **207**, 1.
- Meggit, S.M.A. and Wickramasinghe, D.T. 1988, *M. N. R. A. S.*, submitted.
- Pirola, V., 1988, Vatican Workshop, "*Polarized Radiation of Circumstellar Origin*", Ed. Coyne, G. V., Magalhaes, A. M., Moffat, A. F. J., Schulte-Ladbeck, R. E., Tapia, S., and Wickramasinghe, D. T., (Vatican Press), in press.

- Pirola, V., Reiz, A. and Coyne, G.V. 1987, *Astr. Ap.*, in press.
- Schmidt, G. D. 1988, Vatican Workshop, "*Polarized Radiation of Circumstellar Origin*", Ed. Coyne, G. V., Magalhaes, A. M., Moffat, A. F. J., Schulte-Ladbeck, R. E., Tapia, S., and Wickramasinghe, D. T., (Vatican Press), in press.
- Schmidt, G., Stockman, H.S. and Grandi, S. 1986, *Ap. J.* **300**, 804.
- Stockman, H.S., Foltz, C.B., Schmidt, G.D., Tapia, S. 1987, *Ap. J.*, **271**, 725.
- Stockman, H.S., and Lubenow, A.F. 1987, *Ap. Space. Sci.*, **131**, 611.
- Visvanathan, N. and Wickramasinghe, D.T. 1979, *Nature*, **281**, 47.
- Wickramasinghe, D.T. 1988, Vatican Workshop, "*Polarized Radiation of Circumstellar Origin*", Ed. Coyne, G. V., Magalhaes, A. M., Moffat, A. F. J., Schulte-Ladbeck, R. E., Tapia, S., and Wickramasinghe, D. T., (Vatican Press), in press.
- Wickramasinghe, D.T. and Meggitt, S.M.A. 1982, *M. N. R. A. S.*, **198**, 975.
- Wickramasinghe, D.T. and Meggitt, S.M.A. 1985a, *M. N. R. A. S.*, **214**, 605 (WM).
- Wickramasinghe, D.T. and Meggitt, S.M.A., 1985b, *M. N. R. A. S.*, **216**, 857.
- Wickramasinghe, D.T., Reid, I.N. and Bessell, M.S. 1984, *M. N. R. A. S.* **211**, 37p.

4.2 Introduction

Chapter 4

Arc-Shaped Cyclotron Emission Regions in AM Herculis Systems

4.1 Abstract

We discuss the properties of cyclotron radiation originating from homogeneous arc-shaped emission regions, taking into account the effects of field spread across the shock. We find that arc-shaped cyclotron emission regions give rise to asymmetric light and polarization curves which are in closer agreement with observations of some AM Herculis systems than previous point-source and cylindrically extended models.

Subject headings: radiation mechanisms – shock waves – stars: binaries – stars: magnetic.

4.2 Introduction

The AM Herculis systems belong to the cataclysmic variables (CVs) class. These objects are characterized by the presence of strong linear and circular polarization at optical and near IR wavelengths. It is now well established that the polarized emission is of cyclotron origin, arising from accretion shocks near the surface of the strongly magnetized ($B \approx 20 - 60$ MG) white dwarf primary. The radiation properties of AM Herculis systems have been qualitatively explained by Meggitt and Wickramasinghe (1982) and Chamugam and Dulk (1981). Wickramasinghe and Meggitt (1985) modelled the cyclotron emission from AM Her systems in terms of constant Λ (or "point source") models which assume uniform conditions within the shock but allow for optical depth effects. In these models, the emission regions are located at the magnetic poles of a centered dipole field distribution. Although the constant Λ models have been very successful in explaining the general characteristics of the observations, they cannot explain the following observational features: (1) the wide wavelength range over which circular and linear polarization are detected; (2) flat polarized energy distributions in the optical seen in some systems; (3) asymmetries in phase-dependent light and polarization curves and (4) absence of a clear cyclotron harmonic pattern in their spectra.

Wickramasinghe and Ferrario (1988) have shown that it is possible to explain most of the above characteristics by assuming that the radiation originates from cylindrically extended emission regions, displaced from the polar caps and with density and temperature structure across the shock. However, the asymmetries predicted by the model in the phase dependent light and polarization curves are not large enough to explain observations of some systems such as E1405-451 (=V834 Cen). There is now considerable evidence suggesting that in some systems the emission regions are arc-like with a large angular extent (Beuermann, Stella, and Patterson 1987; Cropper 1987; Schmidt 1988; Cropper 1989 [hereafter C89]; Ferrario, Wickramas-

inghe, and Tuohy 1989, [hereafter FWT]). In this paper, we present results of new calculations on the properties of homogeneous arc-shaped cyclotron emission regions which extend across the stellar surface allowing for magnetic field spread. We use our model to interpret some recent observations of E1405-451, VV Puppis and CW1103+254 (=ST LMi). We remark that a preliminary report of this work has been given in a review paper on cyclotron emission properties of AM Her systems presented by Wickramasinghe (1988).

4.3 Why Arc-Shaped Cyclotron Emission Regions?

Very recently, FWT have constructed theoretical models to interpret radial velocity and velocity dispersion data of the broad emission line component in AM Her systems. These models provide information about the location of the coupling region and about the shape and the extension of the cyclotron emission region on the surface of the white dwarf. The application of their model to E1405-451, CW1103+254 and EXO 033319-2554.2 indicates that in these systems the coupling region is located approximately 0.5-0.75 of the way between the white dwarf and the inner Lagrange point, suggesting that the material leaving the secondary star can penetrate deep into the primary's magnetosphere before being threaded by the magnetic field and forced to accrete along non-polar field lines. The angle by which the cyclotron emission region is offset from the dipole axis depends on the location of the coupling region and is found to be $\approx 10^\circ$. In order to fit the velocity dispersion curves, FWT find that it is necessary to assume that accretion occurs over a very wide range of azimuthal angles. This result implies that the cyclotron emission regions can neither be point sources nor have cylindrical symmetry, but must instead have the shape of an arc whose extension in magnetic longitude is much greater than in latitude.

Beuermann, Stella and Patterson (1987) also deduce the presence of an

arc-like emission region in the AM Her system 2A0311-227 (= EF Eri), offset by about 20° - 25° from the magnetic pole and with the cyclotron radiation coming from a very wide region surrounding the small area where the hard X-rays are produced. The existence of an extended cyclotron emission region which is much larger than the X-ray region has been also proposed by Schmidt, Stockman and Grandi (1986), and Liebert and Stockman (1985).

In 1987, Cropper suggested the presence of a cyclotron emission region in H0139-68 (= BL Hyi) which is elongated toward the orbital plane, in order to explain the bright phase duration and the position angle curve.

Further evidence for an azimuthally extended emission region comes from observations of E1114+182 (= DP Leo) conducted by Schmidt (1988) who measured the size and shape of the emission region from the ingress and egress profiles of the eclipse of the emission region by the M-dwarf. Schmidt (1988) concludes that the cyclotron emission in E1114+182 originates from an area whose length in the plane of the orbit is about half the diameter of a $0.4 M_\odot$ primary.

Although large longitudinal extensions of cyclotron emission regions seem to be the only way to explain observational data in several AM Her systems, we remark that this might not be a property shared by all the members of this class. In fact, the length of the arc is expected to be strongly dependent on the dipole inclination and on the location of the coupling region. We note in this connection, that while Schmidt (1988) finds the length of the cyclotron emission region comparable to the size of the primary in E1114+182, similar work conducted by Bailey *et al.* (1988) on EXO 023432-5232.3 gives an upper limit on the length of the cyclotron region which is about one seventh the diameter of the white dwarf.

In this paper, we shall deduce values in the range $\approx 10^{-4} - 10^{-3}$ for the fractional area of the star over which accretion occurs. These values are in agreement with the sizes deduced by Schmidt (1988) and Bailey *et al.* (1988) and with the theoretical results of FWT obtained through an emission line study.

4.4 The Models

Let us consider a coordinate system $Oxyz$ where the origin O is the center of the white dwarf, the z -axis is parallel to the spin axis and the plane Oxy coincides with the orbital plane. In this reference system the dipole axis \vec{d} is inclined at an angle θ_d to the z -axis. The line of sight and the dipole axis are in the plane Oxz at orbital phase $\phi = \phi_0$. The angle Φ (see Fig 4.1a) is $2\pi(\phi - \phi_0)$ or $-2\pi(\phi - \phi_0)$ depending on the sense of rotation of the white dwarf.

We consider a second reference system $Ox'y'z'$ with the z' -axis parallel to \vec{d} and the x' -axis in the plane containing the spin axis Oz and the dipole axis Oz' (see Fig. 4.1a). The ribbon-like cyclotron emission region is delimited in magnetic latitude by θ_1 , θ_2 , and θ_2^* (measured from the z' -axis), and in magnetic longitude by ψ_1 and ψ_2 (measured from the x' -axis). The longitudinal and latitudinal extensions of the region (angular thickness and length) are given by $\Delta\theta (= \theta_2 - \theta_1)$ and $\Delta\psi (= \psi_2 - \psi_1)$ respectively. The quantity $\Delta\theta^* = \theta_2^* - \theta_2$ gives the elongation of the cyclotron emission region towards the magnetic equator. If $\Delta\theta^* = 0^\circ$, the region is an arc whose boundaries are curves of constant magnetic latitude and longitude. We have sketched in Figure 4.1b the location and shape of the cyclotron emission region with the geometrical parameters that we have used in our calculations.

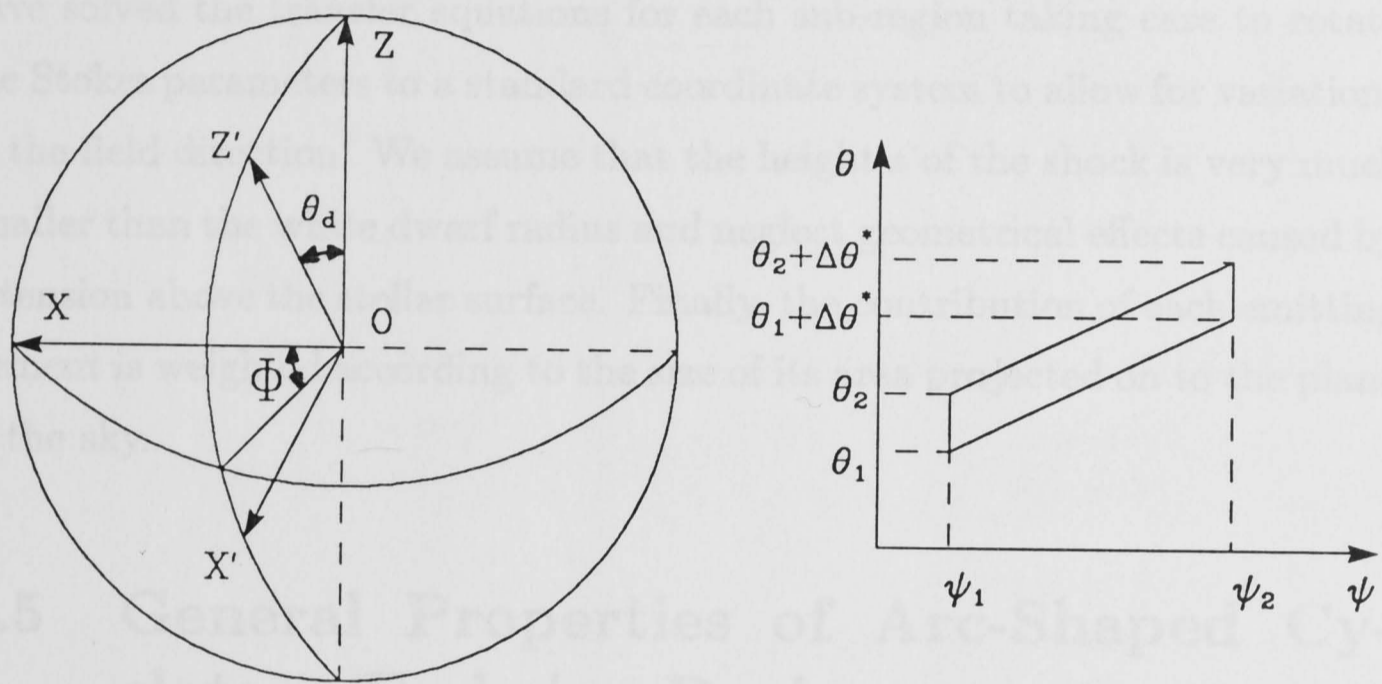
The models have been constructed assuming constant electron temperature, T_e , electron number density, N_e , and radial thickness above the white dwarf surface, s . The emission regions are characterized by the optical depth parameter (Meggitt and Wickramasinghe 1982):

$$\Lambda_s = 2.01 \times 10^6 \left(\frac{s}{10^6 \text{cm}} \right) \left(\frac{N_e}{10^{16} \text{cm}^{-3}} \right) \left(\frac{3 \times 10^7 \text{G}}{B} \right), \quad (1)$$

in the radial direction. The value of Λ_s changes across the cyclotron emission region because of changes in the magnetic field strength B . In order to label the models we shall refer to the polar field strength B_p and to the value of Λ_s obtained by substituting B_p in equation (1). Cyclotron and free-free

specimens are included following Megitt and Wickramasinghe (1983) and Wickramasinghe and Megitt (1985) respectively.

The calculations are carried out by dividing the emitting surface into sufficiently small sub-regions over which the magnetic field strength and the angle α between the direction and line of sight can be taken as constant. We have solved the above equations for each sub-region taking care to ensure the Stokes parameters are calculated in a consistent system to allow for variations in the sign of the parameters. We assume the width of the shock is very much smaller than the radius of the star so that the emission region is a small area on the surface.



(a)

(b)

In Figures 4.2 through 4.5, we have plotted, respectively, intensity, linear and circular polarization and position angle curves as a function of phase for different values of azimuthal extension $\Delta\psi$ and latitudinal $\Delta\theta$ of the emission region towards the magnetic equator. The curves presented correspond to $\Phi = 2\pi(\phi - \phi_0)$ (increasing Φ) with the cyclotron emission region extending from negative azimuthal angles ($\psi_1 < 0^\circ$) to zero ($\psi_2 = 0^\circ$). The curves shown are calculated for $\theta_1 = 0^\circ$ and $\theta_2 = 30^\circ$.

Figure 4.1: Model Geometry

(a) White dwarf geometry. The point O is the center of the white dwarf. The z -axis is parallel to the rotation axis and the x -axis is given by the projection of the line of sight on to the orbital plane. The z' -axis is parallel to the dipole axis and the x' -axis is in the plane Ozz' . The angle that the dipole axis z' forms with the spin axis z is indicated by θ_d . The angle Φ (angle between the projection of the dipole axis z' on to the orbital plane and the x -axis) increases or decreases with orbital phase depending on the sense of rotation of the white dwarf. (b) Magnetic longitudinal (ψ) and latitudinal (θ) boundaries of the cyclotron emission region.

opacities are included following Meggitt and Wickramasinghe (1982) and Wickramasinghe and Meggitt (1985) respectively.

The calculations are carried out by dividing the emitting surface into sufficiently small sub-regions over which the magnetic field strength and the angle α between field direction and line of sight can be taken as constant. We have solved the transfer equations for each sub-region taking care to rotate the Stokes parameters to a standard coordinate system to allow for variations in the field direction. We assume that the height s of the shock is very much smaller than the white dwarf radius and neglect geometrical effects caused by extension above the stellar surface. Finally, the contribution of each emitting element is weighted according to the size of its area projected on to the plane of the sky.

4.5 General Properties of Arc-Shaped Cyclotron Emission Regions

In Figures 4.2 through 4.5, we have plotted, respectively, intensity, linear and circular polarization and position angle curves as a function of phase for different values of azimuthal extension $\Delta\psi$ and elongation $\Delta\theta^*$ of the emission region towards the magnetic equator. The cases presented correspond to $\Phi = 2\pi(\phi - \phi_0)$ (increasing Φ) with the cyclotron emission region extending from negative azimuthal angles ($\psi_1 < 0^\circ$) to zero ($\psi_2 = 0^\circ$). The curves shown are calculated for fixed values of orbital inclination ($= 50^\circ$), colatitude of the magnetic pole ($= 20^\circ$), and thickness $\Delta\theta$ ($\theta_1 = 10^\circ$ and $\theta_2 = 12^\circ$) of the cyclotron emission region. The models have $B_p = 3.0 \times 10^7$ Gauss, $T_e = 10$ keV, $N_e = 1.0 \times 10^{16} \text{ cm}^{-3}$ and $\Lambda_s = 2.0 \times 10^5$ in the radial direction. The curves shown have been obtained for harmonic number $n = \omega/\omega_c = 8$ assuming that the emission is caused by pure cyclotron radiation.

We begin by noting that asymmetries occur whenever the emission region is placed asymmetrically with respect to the magnetic meridian $\psi = 0^\circ$.

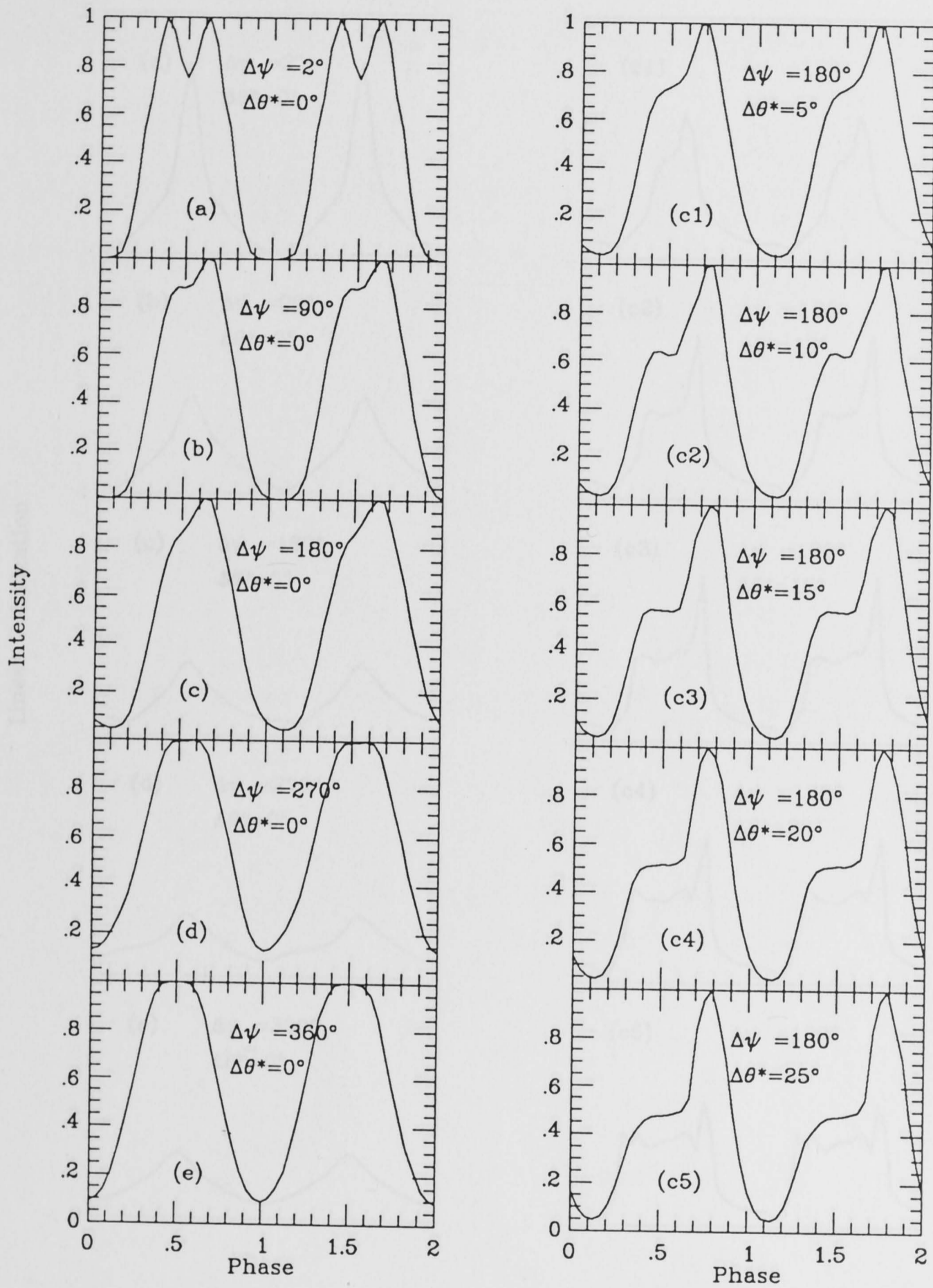


Figure 4.2: Theoretical Intensity Curves
 Theoretical intensity curves obtained for fixed values of $i(= 50^\circ)$, $\theta_d(= 20^\circ)$ and angular thickness of the cyclotron emission region ($\theta_1 = 10^\circ$ and $\theta_2 = 12^\circ$).

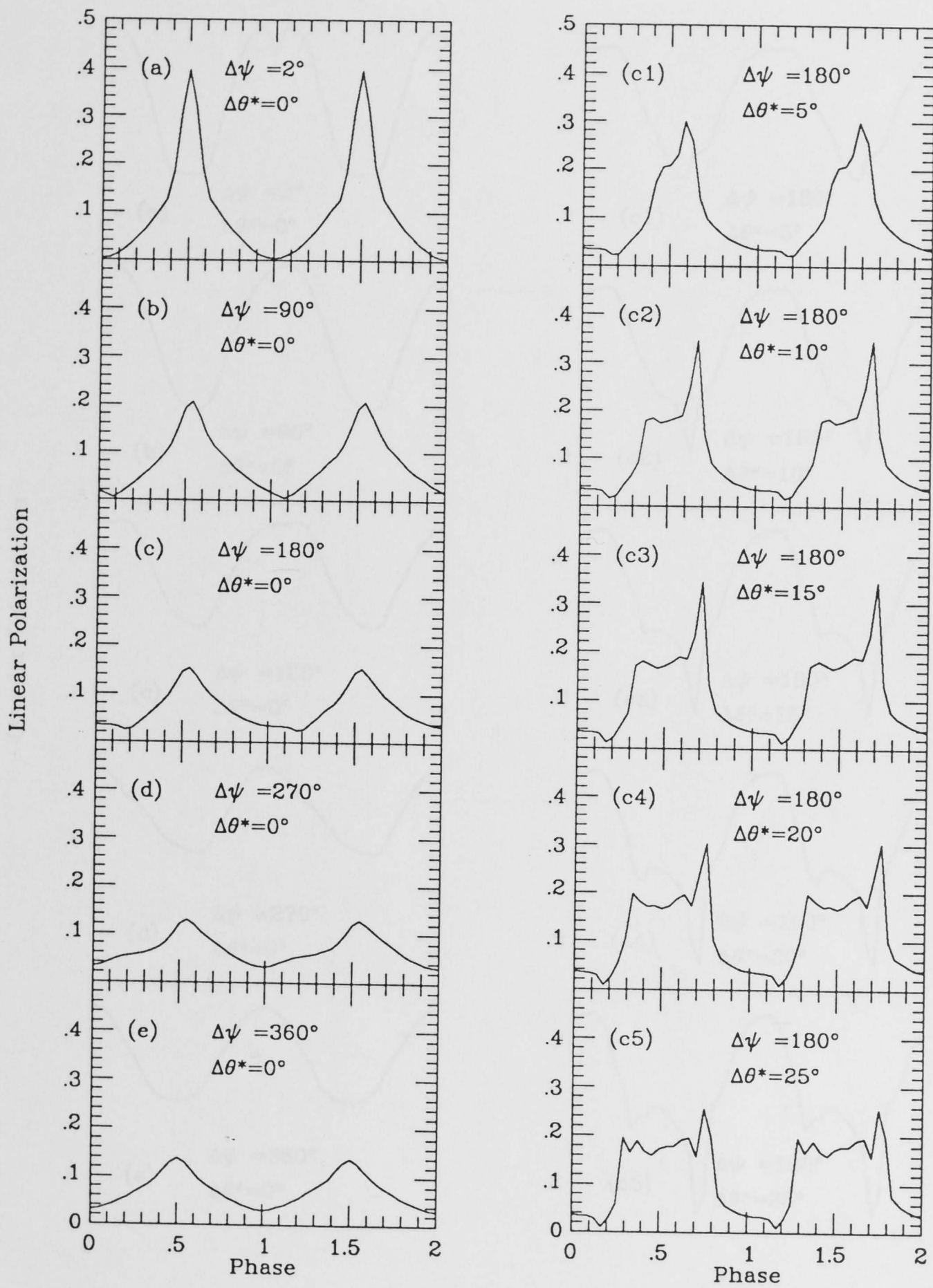


Figure 4.3: Theoretical Linear Polarization Curves
 Theoretical linear polarization curves obtained for fixed values of $i (= 50^\circ)$, $\theta_d (= 20^\circ)$ and angular thickness of the cyclotron emission region ($\theta_1 = 10^\circ$ and $\theta_2 = 12^\circ$).

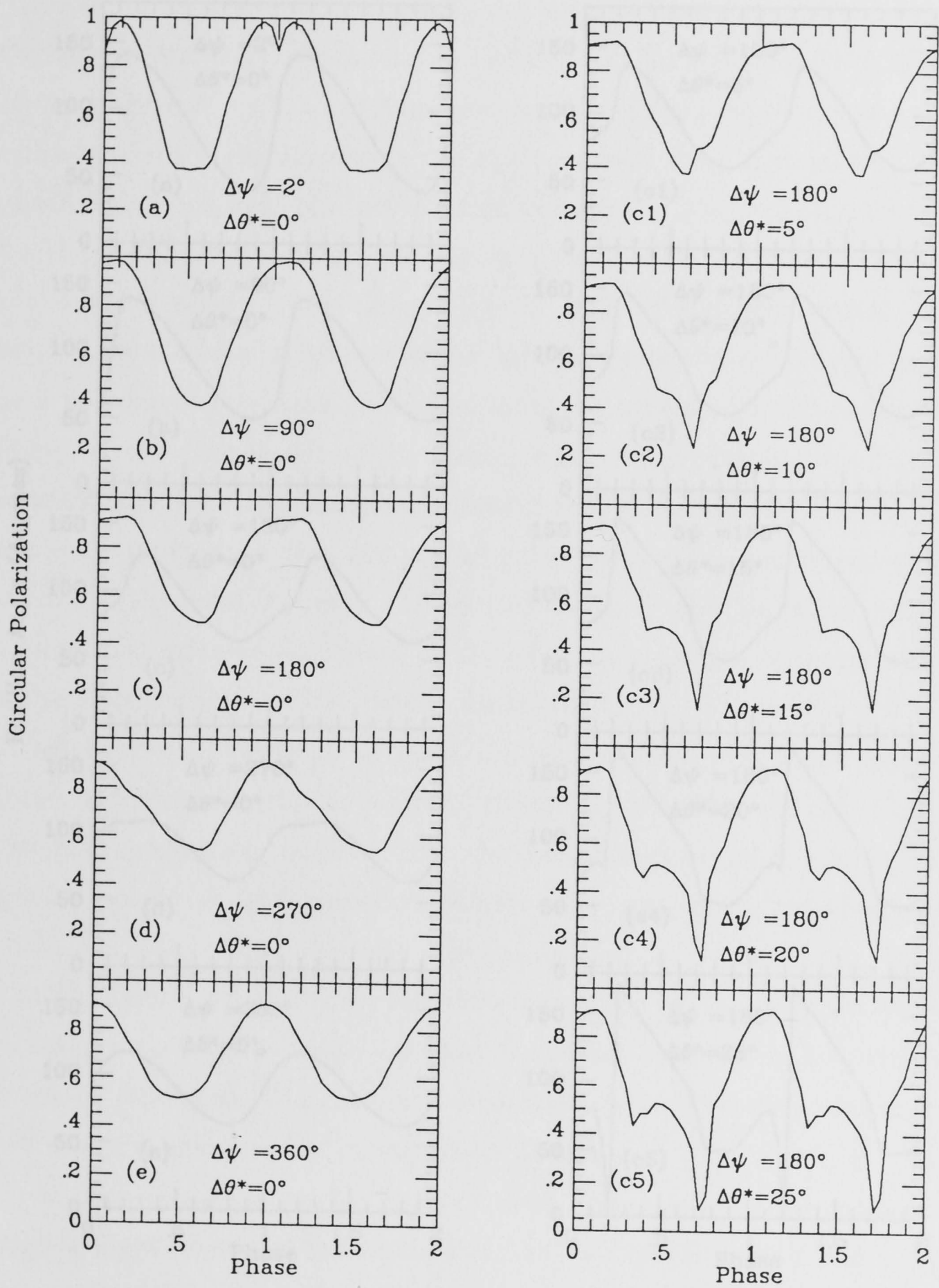


Figure 4.4: Theoretical Circular Polarization Curves
 Theoretical circular polarization curves obtained for fixed values of $i (= 50^\circ)$, $\theta_d (= 20^\circ)$ and angular thickness of the cyclotron emission region ($\theta_1 = 10^\circ$ and $\theta_2 = 12^\circ$).

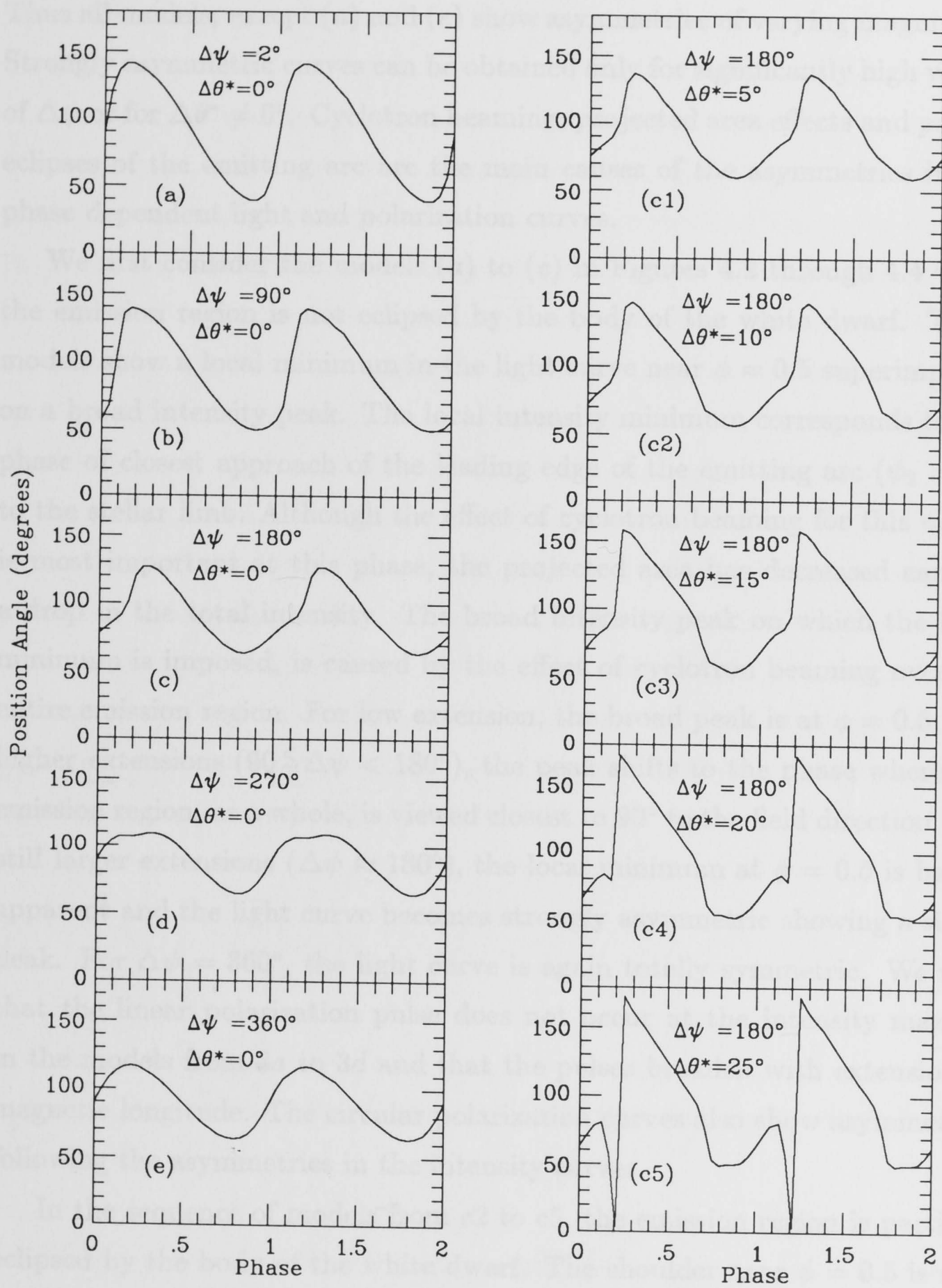


Figure 4.5: Theoretical Position Angle Curves
 Theoretical position angle curves obtained for fixed values of $i (= 50^\circ)$, $\theta_d (= 20^\circ)$ and angular thickness of the cyclotron emission region ($\theta_1 = 10^\circ$ and $\theta_2 = 12^\circ$).

Thus all models, except (a) and (e) show asymmetries of varying magnitude. Strongly asymmetric curves can be obtained only for significantly high values of $\Delta\psi$ or for $\Delta\theta^* \neq 0^\circ$. Cyclotron beaming, projected area effects and partial eclipses of the emitting arc are the main causes of the asymmetries in the phase dependent light and polarization curves.

We first consider the models (a) to (e) in Figures 4.2 through 4.4 when the emission region is not eclipsed by the body of the white dwarf. These models show a local minimum in the light curve near $\phi = 0.5$ superimposed on a broad intensity peak. The local intensity minimum corresponds to the phase of closest approach of the leading edge of the emitting arc ($\psi_2 = 0^\circ$) to the stellar limb. Although the effect of cyclotron beaming for this region is most important at this phase, the projected area has decreased causing a drop in the total intensity. The broad intensity peak on which the local minimum is imposed, is caused by the effect of cyclotron beaming over the entire emission region. For low extension, the broad peak is at $\phi = 0.5$. For higher extensions ($90^\circ \lesssim \Delta\psi < 180^\circ$), the peak shifts to the phase where the emission region, as a whole, is viewed closest to 90° to the field direction. For still larger extensions ($\Delta\psi \approx 180^\circ$), the local minimum at $\phi = 0.5$ is barely apparent and the light curve becomes strongly asymmetric showing a single peak. For $\Delta\psi = 360^\circ$, the light curve is again totally symmetric. We note that the linear polarization pulse does not occur at the intensity maxima in the models from 3a to 3d and that the pulses broaden with extension in magnetic longitude. The circular polarization curves also show asymmetries following the asymmetries in the intensity curves.

In the sequence of models from c2 to c5, the emission region is partially eclipsed by the body of the white dwarf. The shoulder near $\phi = 0.5$ is now the result of the eclipse of regions near the leading edge of the arc. A double pulse appears in these models since the angle between the field direction near the leading edge of the arc and the line of sight crosses 90° twice. The circular polarization curve becomes highly asymmetric showing minima at the phases of these pulses ($\phi \approx 0.3$ and $\phi \approx 0.7$). For still larger $\Delta\theta^*$ (not

shown), the circular polarization shows a reversal in sign over a short phase range.

Let us now consider the variation of position angle with orbital phase illustrated in Figure 4.5. For small extensions of the cyclotron emission region, we find the behaviour seen in point source models. The curve changes shape for large $\Delta\psi$ and $\Delta\theta^*$. The main effect caused by an increase in $\Delta\psi$ (for $\Delta\theta^* = 0^\circ$) is a decrease in the amplitude of the position angle curve. As $\Delta\psi$ increases, regions with field directions that make smaller angles with the spin axis become included and as a result the amplitude of the position angle curve decreases. The most dramatic effects occur again when the cyclotron emission region extends toward the magnetic equator ($\Delta\theta^* \neq 0^\circ$). The sharp rise at $\phi \approx 0.2$ is caused by the line of sight approaching the field cone (cone generated by the field direction, see Wickramasinghe 1988) at the leading edge of the arc. This rise becomes sharper when $\Delta\theta^*$ increases. When $\Delta\theta^* = 25^\circ$ (model c5) the line of sight crosses the field cone so that full variations from 0° to 180° become possible. The final result consists of two separate waves in the position angle curve.

4.6 Application to Three AM Herculis Systems

4.6.1 *Non-Eclipsing Cyclotron Emission Region: Application to E1405-451*

E1405-451 is an AM Her object with a period of 101.5 min (Jensen, Nousek and Nugent 1982). The light curve does not show any evidence for an eclipse and the circular polarization always shows the same sign. These observations have been interpreted in terms of a dominant cyclotron emission region which is always in the visible hemisphere so that the angle between the line of sight and the magnetic field never crosses the value of 90° . The linear po-

sition angle data oscillate between a minimum and a maximum value, never reaching 180° , therefore indicating that the line of sight \vec{l} is outside the cone generated by the field direction \vec{B} (field cone). The presence of a linear polarization pulse detected near $\phi \approx 0.5$ (C89, Cropper, Menzies, and Tapia 1986; Tuohy, Visvanathan, and Wickramasinghe 1985) suggests that the field direction makes an angle $\approx 80^\circ - 90^\circ$ with the line of sight at this phase. If we assume that the emission region is near the magnetic pole with the field lines nearly radial, the dipole inclination is $\theta_d \approx 35^\circ - 10^\circ$ and the orbital inclination is $i \approx 45^\circ - 60^\circ$.

In this section, we apply our cyclotron emission model to some data for E1405-451 obtained by Cropper, Menzies and Tapia (1986) and C89. Our best fit models for these data are obtained by assuming an orbital inclination $i = 45^\circ$ and a colatitude of the dipole axis $\theta_d = 15^\circ$. The emission region is characterized by $B_p = 2.5 \times 10^7$ Gauss, $N_e = 1.0 \times 10^{16} \text{ cm}^{-3}$, $T_e = 10$ keV and $\Lambda_s = 2.4 \times 10^5$ in the radial direction. Since the observations are in white light, several harmonics will contribute to the observed radiation, thus our model fit only give an estimate of an *effective* n for the white light passband. The harmonic number n can change with accretion rate as the intensity peak shifts within the waveband.

Let us first consider the data in Figure 4.6 obtained by Cropper, Menzies and Tapia (1986) in April 1983. We note that the light curve shows a double hump with a minimum at $\phi \approx 0.5$, caused by a projected area effect, and two maxima at $\phi \approx 0.3$ and $\phi \approx 0.7$. The circular polarization data also show the presence of a double peak. The minimum corresponding to $\phi \approx 0.0$ occurs when we are looking down the accretion column. This minimum is explained in the following way. In case of pure cyclotron emission, the maximum percentage of circular polarization occurs at the intensity minimum. Therefore, if other sources of unpolarized radiation are present (*e.g.* white dwarf photosphere, accretion stream, secondary star, etc.), they become dominant and give rise to the observed low percentage of circular polarization (standstill) at the light minimum. We have been able to reproduce this standstill by

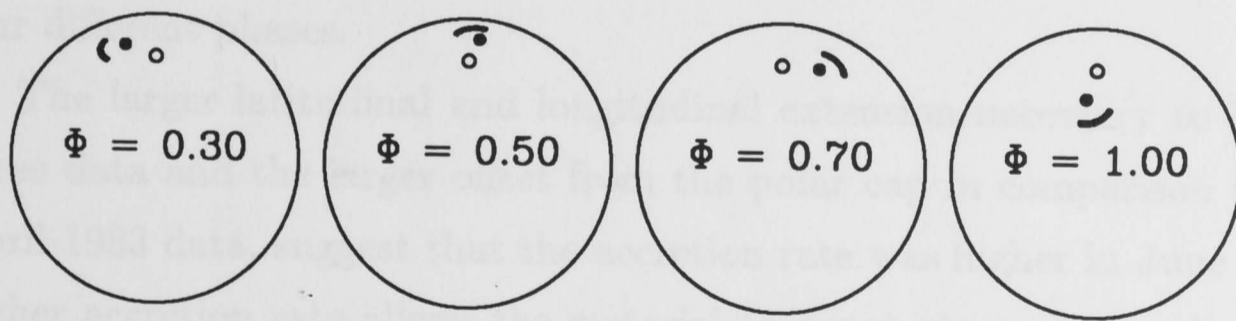
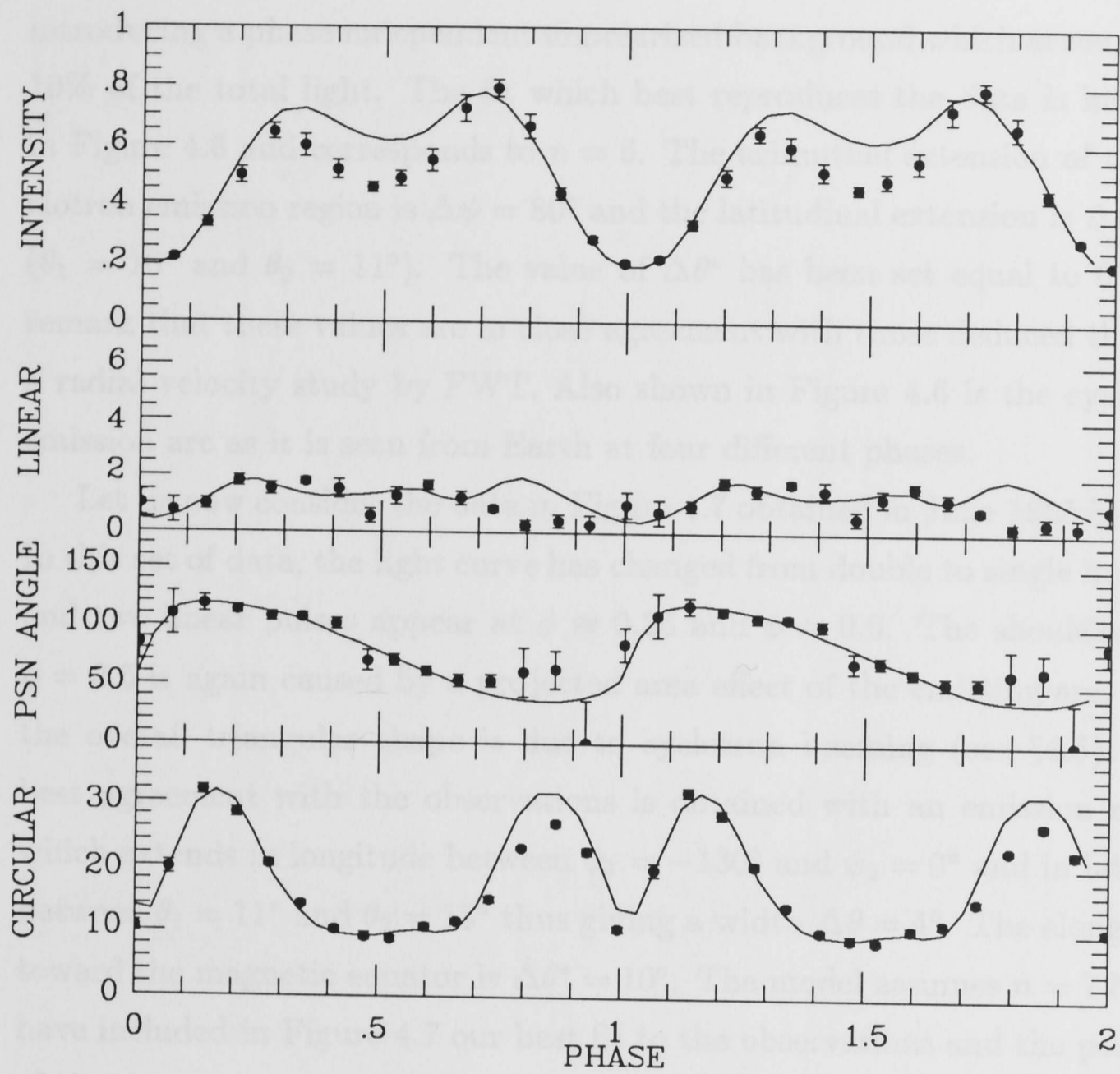


Figure 4.6: Application of Model to E1405-451: April 1983
 Upper panel: Application of our model to data for E1405-451 obtained by Cropper, Menzies, and Tapia (1983). Lower panel: position of the cyclotron emission region as seen from Earth at four different phases. Circle: spin axis, filled circle: dipole axis.

introducing a phase independent unpolarized background which accounts for 10% of the total light. The fit which best reproduces the data is included in Figure 4.6 and corresponds to $n = 6$. The azimuthal extension of the cyclotron emission region is $\Delta\psi = 80^\circ$ and the latitudinal extension is $\Delta\theta = 1^\circ$ ($\theta_1 = 10^\circ$ and $\theta_2 = 11^\circ$). The value of $\Delta\theta^*$ has been set equal to 0° . We remark that these values are in close agreement with those deduced through a radial velocity study by FWT. Also shown in Figure 4.6 is the cyclotron emission arc as it is seen from Earth at four different phases.

Let us now consider the data in Figure 4.7 obtained in June 1985 by C89. In this set of data, the light curve has changed from double to single humped and two linear pulses appear at $\phi \approx 0.35$ and $\phi \approx 0.6$. The shoulder near $\phi = 0.5$ is again caused by a projected area effect of the emitting arc, while the overall triangular shape is due to cyclotron beaming (see §4.5). The best agreement with the observations is obtained with an emission region which extends in longitude between $\psi_1 = -130^\circ$ and $\psi_2 = 0^\circ$ and in latitude between $\theta_1 = 11^\circ$ and $\theta_2 = 15^\circ$ thus giving a width $\Delta\theta = 4^\circ$. The elongation toward the magnetic equator is $\Delta\theta^* = 10^\circ$. The model assumes $n = 7.5$. We have included in Figure 4.7 our best fit to the observations and the position of the emitting arc on the visible hemisphere of the white dwarf surface at four different phases.

The larger latitudinal and longitudinal extension necessary to interpret these data and the larger offset from the polar cap in comparison with the April 1983 data, suggest that the accretion rate was higher in June 1985. A higher accretion rate allows the material to penetrate more deeply into the white dwarf magnetosphere, thus forcing accretion along field lines whose foot points are further away from the polar caps.

The agreement achieved with the observations is good for both intensity and linear polarization data. We note that the model predicts two pulses from the same cyclotron emission region, but they are not as sharp as observed.

The observed circular polarization curve shows the same characteristics as in the April 1983 data except that the percentage of circular polarization

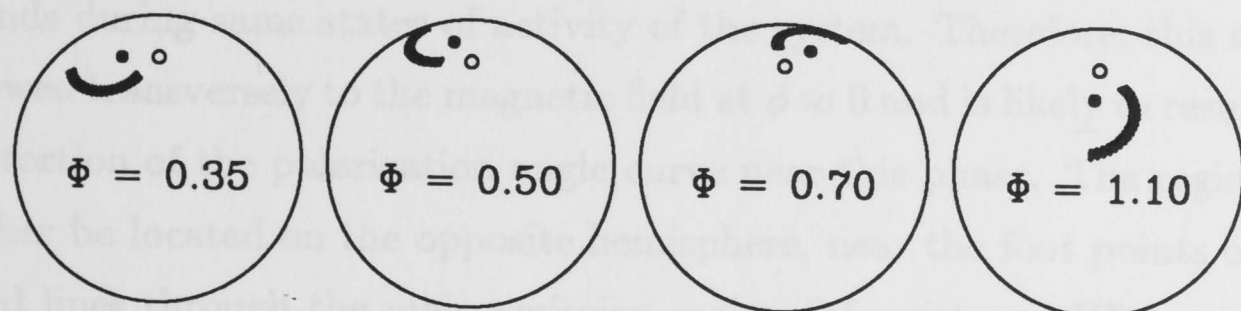
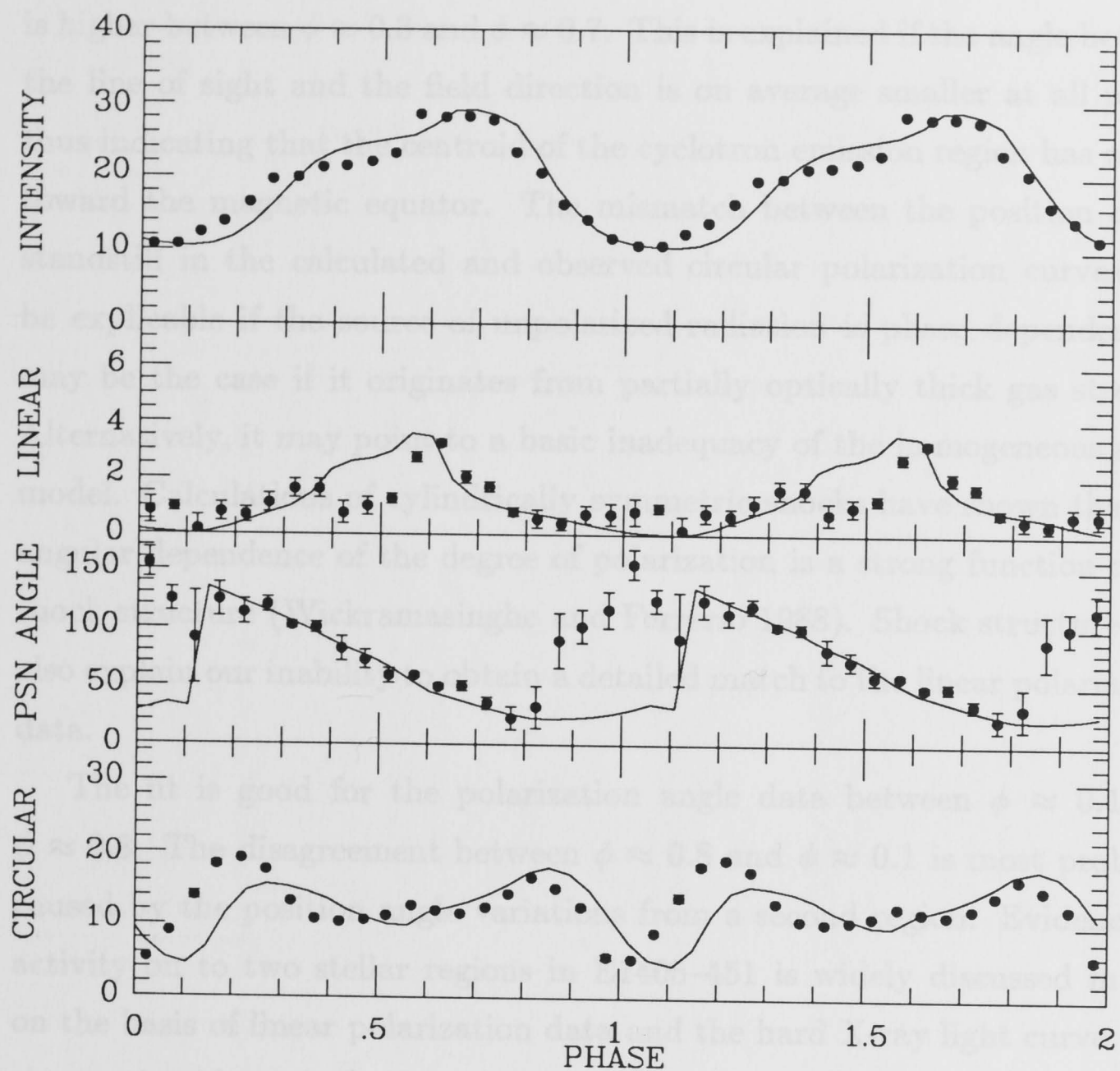


Figure 4.7: Application of Model to E1405-451: June 1985
 Upper panel: Application of our model to data for E1405-451 obtained by Cropper (1989). The discrepancy between the theoretical curves and the data for the polarization angle between $\phi \approx 0.8 - 0.1$ is probably caused by inhomogeneities in the emitting arc and/or by the presence of a second emission region. Lower panel: position of the cyclotron emission region as seen from Earth at four different phases. Circle: spin axis, filled circle: dipole axis.

is higher between $\phi \approx 0.3$ and $\phi \approx 0.7$. This is explained if the angle between the line of sight and the field direction is on average smaller at all phases thus indicating that the centroid of the cyclotron emission region has moved toward the magnetic equator. The mismatch between the position of the standstill in the calculated and observed circular polarization curves may be explicable if the source of unpolarized radiation is phase dependent, as may be the case if it originates from partially optically thick gas streams. Alternatively, it may point to a basic inadequacy of the homogeneous shock model. Calculations of cylindrically symmetric shocks have shown that the angular dependence of the degree of polarization is a strong function of the shock structure (Wickramasinghe and Ferrario 1988). Shock structure may also explain our inability to obtain a detailed match to the linear polarization data.

The fit is good for the polarization angle data between $\phi \approx 0.1$ and $\phi \approx 0.8$. The disagreement between $\phi \approx 0.8$ and $\phi \approx 0.1$ is most probably caused by the position angle variations from a second region. Evidence for activity on to two stellar regions in E1405-451 is widely discussed in C89 on the basis of linear polarization data and the hard X-ray light curve. The strongest evidence is the presence of a third pulse near $\phi = 0$ in the V and I_{kc} bands during same states of activity of the system. Therefore, this region is viewed transversely to the magnetic field at $\phi \approx 0$ and is likely to result in the distortion of the polarization angle curve near this phase. The region could either be located on the opposite hemisphere, near the foot points of closed field lines through the main emission region (Meggitt and Wickramasinghe 1989; FWT), or may simply be a lower density tail of the main cyclotron emission arc. The good agreement with the observations obtained for the position angle curve of the April 1983 data is explained by the lower state of activity of the system, during which the white dwarf did not have appreciable accretion at the second region.

Finally, we present in Figure 4.8 another set of data obtained by C89 in May 1984. In order to reproduce the observed sawtooth-like intensity profile,

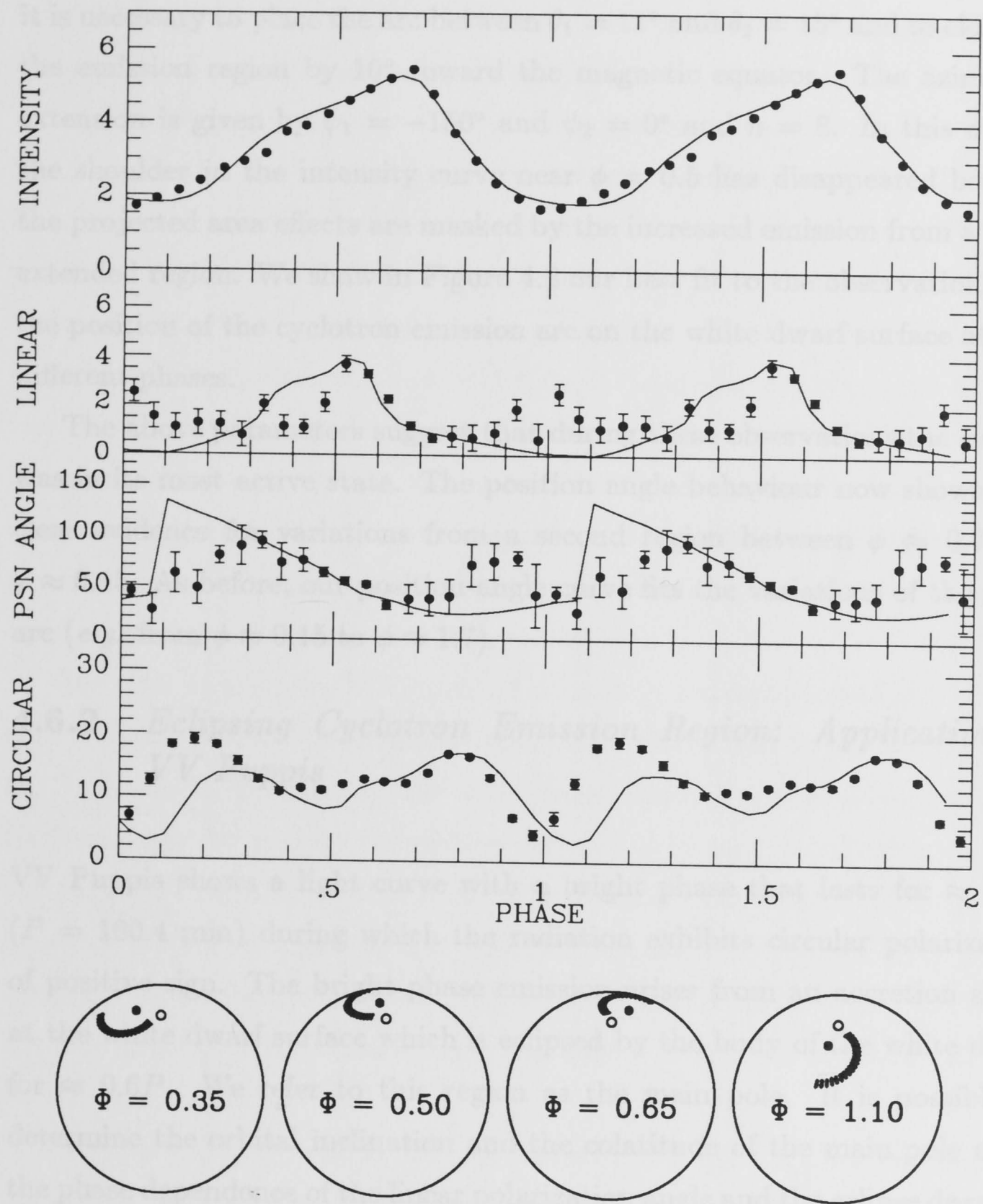


Figure 4.8: Application of Model to E1405-451: May 1984
 Upper panel: Application of our model to data for E1405-451 obtained by Cropper (1989). The discrepancy between the theoretical curves and the data for the polarization angle between $\phi \approx 0.8 - 0.1$ is probably caused by inhomogeneities in the emitting arc and/or by the presence of a second emission region. Lower panel: position of the cyclotron emission region as seen from Earth at four different phases. Circle: spin axis, filled circle: dipole axis.

it is necessary to place the arc between $\theta_1 = 11^\circ$ and $\theta_2 = 15^\circ$ and to elongate the emission region by 10° toward the magnetic equator. The azimuthal extension is given by $\psi_1 = -150^\circ$ and $\psi_2 = 0^\circ$ and $n = 8$. In this model, the shoulder in the intensity curve near $\phi = 0.5$ has disappeared because the projected area effects are masked by the increased emission from a more extended region. We show in Figure 4.8 our best fit to the observations and the position of the cyclotron emission arc on the white dwarf surface at four different phases.

The above parameters suggest that during these observations the system was in its most active state. The position angle behaviour now shows very clear evidence for variations from a second region between $\phi \approx 0.7$ and $\phi \approx 0.15$. As before, our position angle curve fits the variations of the main arc (*e.g.* from $\phi \approx 0.15$ to $\phi \approx 1.7$).

4.6.2 *Eclipsing Cyclotron Emission Region: Application to VV Puppis*

VV Puppis shows a light curve with a bright phase that lasts for $\approx 0.4P$ ($P = 100.4$ min) during which the radiation exhibits circular polarization of positive sign. The bright phase emission arises from an accretion shock at the white dwarf surface which is eclipsed by the body of the white dwarf for $\approx 0.6P$. We refer to this region as the main pole. It is possible to determine the orbital inclination and the colatitude of the main pole using the phase dependence of the linear polarization angle and the eclipse duration (Cropper and Warner 1986; Meggitt and Wickramasinghe 1989). Meggitt and Wickramasinghe (1989) find $i = 74^\circ$ and $\theta_d = 145^\circ$.

The faint phase exhibits either no circular polarization or circular polarization of negative sign depending on the state of activity of the system. It has long been suspected that the polarized emission seen during the faint phase originates from a second shock near the white dwarf surface (Liebert and Stockman 1979). The recent discovery of cyclotron emission harmonics

from both magnetic poles in VV Puppis have confirmed this model (Wickramasinghe, Ferrario, and Bailey 1989).

In this section, we apply our cyclotron emission model to some data of VV Puppis obtained by Cropper and Warner (1986) (Fig. 4.9). In order to interpret these data we have assumed an orbital inclination $i = 75^\circ$ and a colatitude of the dipole axis $\theta_d = 150^\circ$. We will model the cyclotron emission of the main pole only, and no attempts will be made to match the negative circular polarization contribution of the second pole between $\phi \approx 0.2$ and $\phi \approx 0.7$. Following the recent observational results of Wickramasinghe, Ferrario, and Bailey (1989), we have offset the dipole by $0.1R_{wd}$ from the center of the white dwarf in the direction of the dipole axis and we have assumed an "effective" centered dipolar field strength of 4.0×10^7 Gauss (*cf.* Wickramasinghe, Ferrario, and Bailey 1989).

Our best fit is shown in Figure 4.9 superimposed on the data of Cropper and Warner (1986). The emission region is characterized by $N_e = 1.0 \times 10^{16}$ cm^{-3} , $T_e = 10$ keV, $\Lambda_s = 1.5 \times 10^5$ in the radial direction and $n = 8$. Furthermore, the cyclotron emission region has an azimuthal extent $\Delta\psi = 80^\circ$ ($\psi_1 = 20^\circ$ and $\psi_2 = 100^\circ$) and a latitudinal extent of 2° ($\theta_1 = 9^\circ$ and $\theta_2 = 11^\circ$). The elongation $\Delta\theta^*$ toward the magnetic equator is 5° . The longitudinal position of the arc suggests that the material is coupled on to the field lines after the stream passes the line of projection of the dipole axis on the orbital plane.

In general, our model is in good agreement with the observations. In particular, we note that the intensity curve shows a slow rise after eclipse egress and a more rapid decline toward eclipse ingress, as observed. The circular polarization curve shows a similar behaviour and it is characterized by a flat top. The reversal in the sign of the circular polarization at $\phi \approx 0.1$ implies that the field is inclined to the stellar surface and that the average angle α between the field direction and the line of sight crosses 90° at this phase. The absence of a similar reversal near eclipse egress suggests that the field leads the emitting region and that the average angle between the

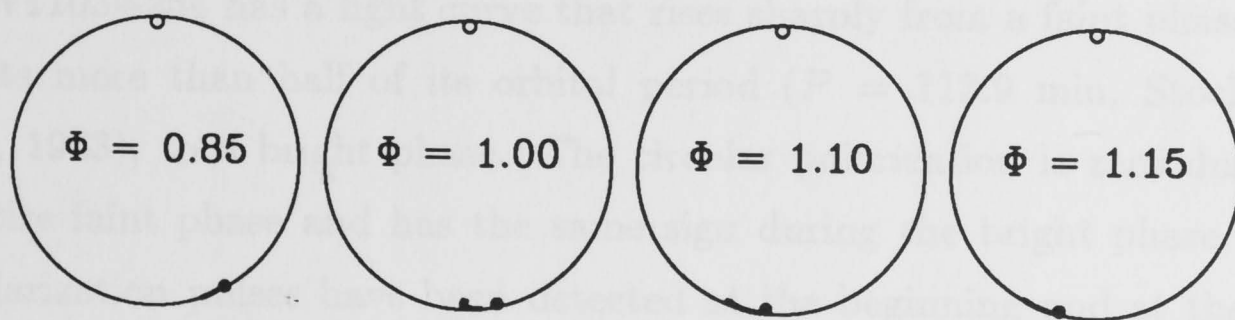
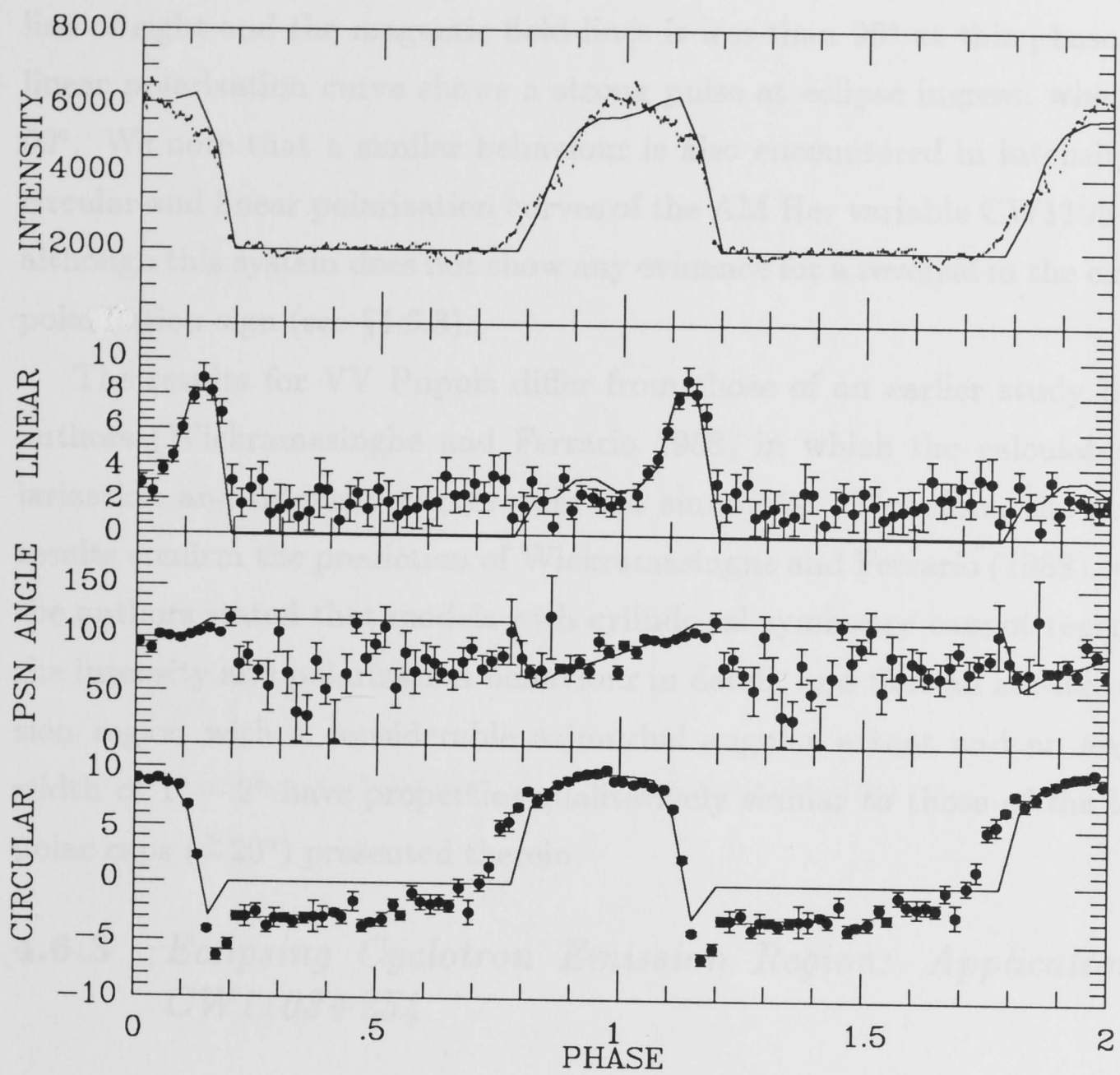


Figure 4.9: Application of Model to VV Puppis
 Upper panel: Application of our model to data for VV Puppis obtained by Cropper and Warner (1986). Lower panel: position of the cyclotron emission region as seen from Earth at four different phases. Circle: spin axis, filled circle: dipole axis.

line of sight and the magnetic field lines is less than 90° at this phase. The linear polarization curve shows a strong pulse at eclipse ingress, when $\alpha \approx 90^\circ$. We note that a similar behaviour is also encountered in intensity and circular and linear polarization curves of the AM Her variable CW1103+254, although this system does not show any evidence for a reversal in the circular polarization sign (see §4.6.3).

The results for VV Puppis differ from those of an earlier study by the authors (Wickramasinghe and Ferrario 1988) in which the calculated polarization and intensity curves were too sinusoidal. Therefore, the present results confirm the prediction of Wickramasinghe and Ferrario (1988), where the authors stated that models with cylindrical symmetry cannot reproduce the intensity and polarization behaviour in detail, and that an arc-like emission region with a considerable azimuthal angular extent and an angular width of $1^\circ - 2^\circ$ have properties qualitatively similar to those of the larger polar caps ($\gtrsim 20^\circ$) presented therein.

4.6.3 *Eclipsing Cyclotron Emission Region: Application to CW1103+254*

CW1103+254 has a light curve that rises sharply from a faint phase, which lasts more than half of its orbital period ($P = 113.9$ min, Stockman *et al.*, 1983), to a bright phase. The circular polarization is zero during the entire faint phase and has the same sign during the bright phase. Linear polarization pulses have been detected at the beginning and at the end of the bright phase by Cropper (1986) and Stockman *et al.* (1983). Unlike VV Puppis, this system has shown no evidence for a secondary emission region in the optical. The observations have been interpreted in terms of a single cyclotron emission region which gives rise to the polarized emission and is eclipsed by the body of the white dwarf during the faint phase (Stockman *et al.* 1983; Schmidt Stockman and Grandi 1983). Cropper (1986) has used the variation of the linear polarization angle with phase to estimate an orbital

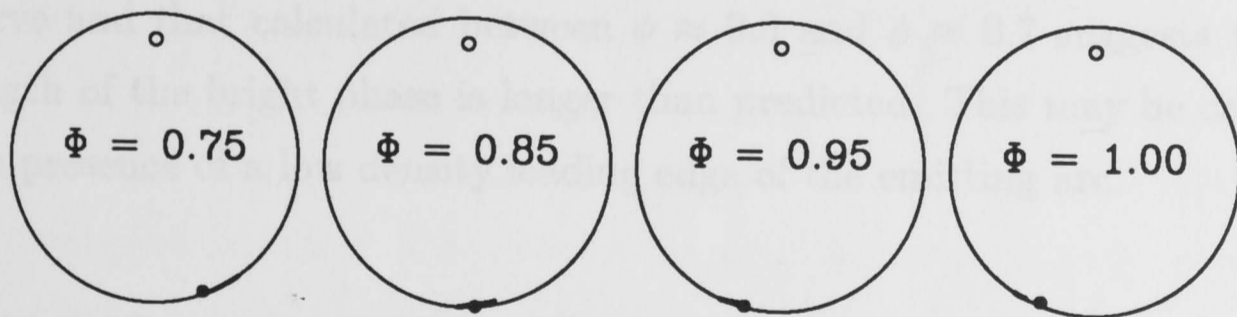
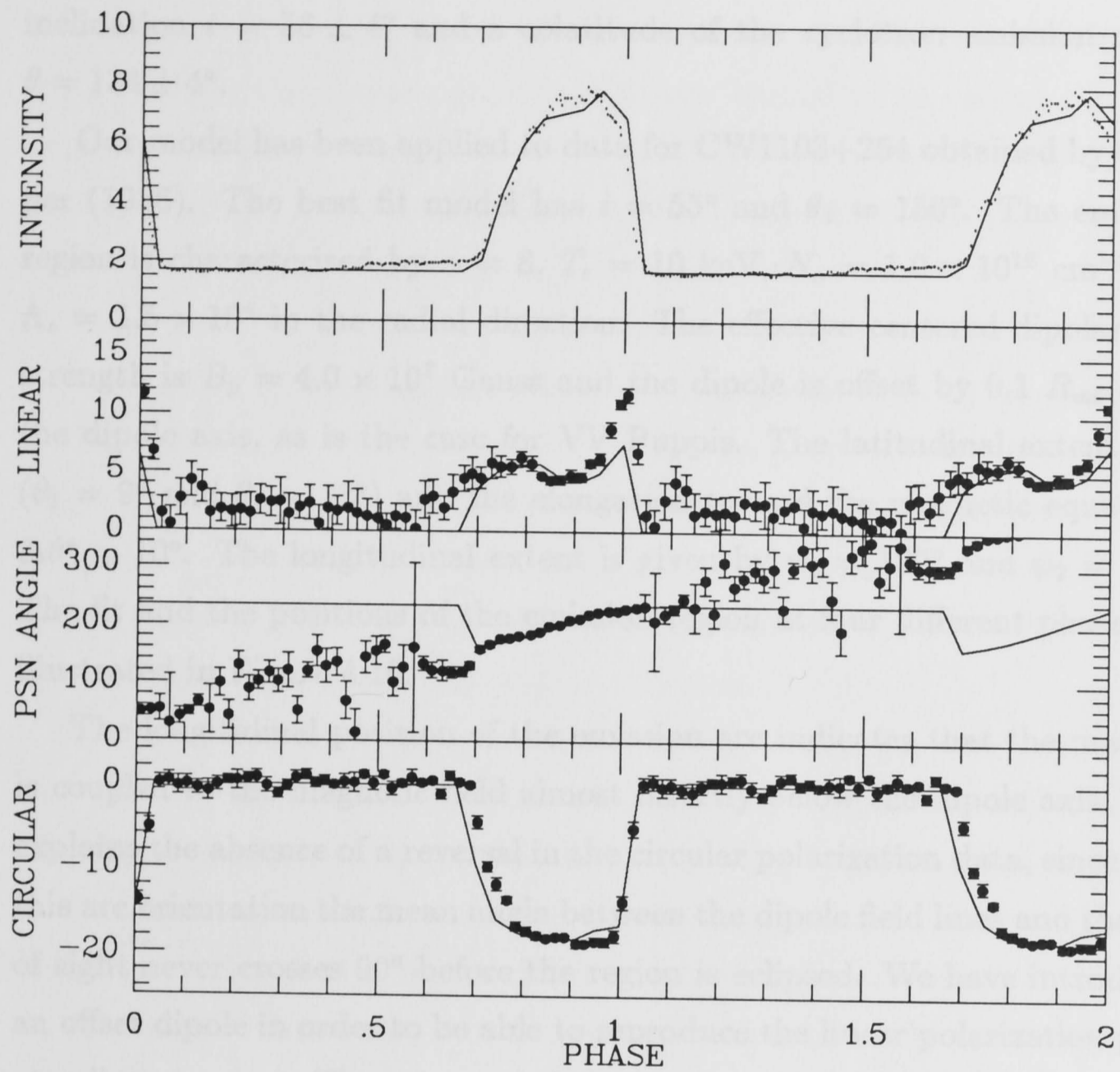


Figure 4.10: Application of Model to CW1103+254
 Upper panel: Application of our model to data for CW1103+254 obtained by Cropper (1986). Lower panel: position of the cyclotron emission region as seen from Earth at four different phases. Circle: spin axis, filled circle: dipole axis.

inclination $i = 56 \pm 4^\circ$ and a colatitude of the cyclotron emission region $\theta = 134 \pm 4^\circ$.

Our model has been applied to data for CW1103+254 obtained by Cropper (1986). The best fit model has $i = 55^\circ$ and $\theta_d = 150^\circ$. The emission region is characterized by $n = 8$, $T_e = 10$ keV, $N_e = 1.0 \times 10^{16}$ cm $^{-3}$ and $\Lambda_s = 1.5 \times 10^4$ in the radial direction. The effective centered dipolar field strength is $B_p = 4.0 \times 10^7$ Gauss and the dipole is offset by $0.1 R_{wd}$ along the dipole axis, as is the case for VV Puppis. The latitudinal extent is 2° ($\theta_1 = 9^\circ$ and $\theta_2 = 11^\circ$) and the elongation toward the magnetic equator is $\Delta\theta^* = 10^\circ$. The longitudinal extent is given by $\psi_1 = 130^\circ$ and $\psi_2 = 200^\circ$. The fit and the positions of the emission region at four different phases are illustrated in Figure 4.10.

The longitudinal position of the emission arc indicates that the material is coupled to the magnetic field almost directly below the dipole axis. This explains the absence of a reversal in the circular polarization data, since with this arc orientation the mean angle between the dipole field lines and the line of sight never crosses 90° before the region is eclipsed. We have introduced an offset dipole in order to be able to reproduce the linear polarization pulse at eclipse ingress. The mismatch between the observed linear polarization curve and that calculated between $\phi \approx 0.6$ and $\phi \approx 0.7$ suggests that the length of the bright phase is longer than predicted. This may be caused by the presence of a low density leading edge of the emitting arc.

4.7 Conclusions

We have investigated the cyclotron emission properties of arc-shaped emission regions. We have found that it is possible to obtain large asymmetries in the polarization and intensity curves by introducing extensions in magnetic latitude and longitude. The main causes for these asymmetries are cyclotron beaming, projected area effects and partial eclipses of the emitting arc.

We have applied our model to three different accretion states of E1405-451. A change in the accretion rate causes variations in the position and extent of the emission region on the surface of the white dwarf. As a consequence, the light curve changes from double humped through single humped to sawtooth-shaped with increasing accretion rate.

The model has also been applied to data for VV Puppis and CW1103+254. The agreement with the observations is good. In particular, we have seen that it is possible to obtain the characteristic rise in intensity after eclipse egress which is more gradual than the decline into eclipse. Furthermore, we have been able to reproduce the flat-topped circular polarization curves. It was not possible to reproduce these features using point source models or cylindrically symmetric emission regions.

We can conclude that our arc-like emission regions produce polarization and intensity curves that are in close agreement with observations of AM Herculis systems. In addition, we have shown that by fitting intensity, linear and circular polarization curves simultaneously it is possible to know the magnetic longitudinal and latitudinal extent of the emitting arc.

Additional information on the location and extension of the emission region can be obtained from the polarization angle curve. We have only had partial success in modelling the position angle variations for two accretion states of E1405-451 because of the presence of a second interfering region on the white dwarf surface and/or because of inhomogeneities of the main cyclotron emission arc. The problem of multiple emission regions and inhomogeneous arcs will be discussed fully in a subsequent paper.

L. F. acknowledges support from an Australian National University post-graduate scholarship.

4.8 References

- Bailey, J. A., Wickramasinghe, D. T., Hough, J., and Cropper, M. 1988, *M. N. R. A. S.*, **234**, 19p.
- Beuermann, K., Stella, L., and Patterson, J. 1987, *Ap. J.*, **316**, 360.
- Chanmugam, C., and Dulk, G. A. 1981, *Ap. J.*, **244**, 569.
- Cropper, M. 1986, *M. N. R. A. S.*, **222**, 853.
- Cropper, M. 1987, *M. N. R. A. S.*, **228**, 389.
- Cropper, M. 1989, *M. N. R. A. S.*, **236**, 935 (C89).
- Cropper, M., Menzies, J. W., and Tapia, S. 1986, *M. N. R. A. S.*, **218**, 201.
- Cropper, M., and Warner, B. 1986, *M. N. R. A. S.*, **220**, 633.
- Ferrario, L., and Wickramasinghe, D. T. 1988, *IAU Colloquium 114 on White Dwarfs*, in press.
- Ferrario, L., Wickramasinghe, D. T., and Tuohy, I. R. 1989, *Ap. J.*, **341**, 227 (FWT).
- Liebert, J., and Stockman, H. S. 1985, in "*Cataclysmic Variables and Low-Mass X-ray Binaries*", ed. D. Q. Lamb and J. Patterson (Dordrecht: Reidel), p. 151.
- Meggitt, S. M. A., and Wickramasinghe, D. T. 1982, *M. N. R. A. S.*, **198**, 71.
- Meggitt, S. M. A., and Wickramasinghe, D. T. 1989, *M.N.R.A.S.*, **236**, 31.
- Schmidt, G. D. 1988, Vatican Workshop, "*Polarized Radiation of Circumstellar Origin*", Ed. Coyne, G. V., Magalhaes, A. M., Moffat, A. F. J., Schulte-Ladbeck, R. E., Tapia, S., and Wickramasinghe, D. T., (Vatican Press), in press.
- Schmidt, G. D., Stockman, H. S., and Grandi, S. A. 1983, *Ap. J.*, **271**, 735.

4.8 References

- Bailey, J. A., Wickramasinghe, D. T., Hough, J., and Cropper, M. 1988, *M. N. R. A. S.*, **234**, 19p.
- Beuermann, K., Stella, L., and Patterson, J. 1987, *Ap. J.*, **316**, 360.
- Chanmugam, C., and Dulk, G. A. 1981, *Ap. J.*, **244**, 569.
- Cropper, M. 1986, *M. N. R. A. S.*, **222**, 853.
- Cropper, M. 1987, *M. N. R. A. S.*, **228**, 389.
- Cropper, M. 1989, *M. N. R. A. S.*, **236**, 935 (C89).
- Cropper, M., Menzies, J. W., and Tapia, S. 1986, *M. N. R. A. S.*, **218**, 201.
- Cropper, M., and Warner, B. 1986, *M. N. R. A. S.*, **220**, 633.
- Ferrario, L., and Wickramasinghe, D. T. 1988, *IAU Colloquium 114 on White Dwarfs*, in press.
- Ferrario, L., Wickramasinghe, D. T., and Tuohy, I. R. 1989, *Ap. J.*, **341**, 227 (FWT).
- Liebert, J., and Stockman, H. S. 1985, in "*Cataclysmic Variables and Low-Mass X-ray Binaries*", ed. D. Q. Lamb and J. Patterson (Dordrecht: Reidel), p. 151.
- Meggitt, S. M. A., and Wickramasinghe, D. T. 1982, *M. N. R. A. S.*, **198**, 71.
- Meggitt, S. M. A., and Wickramasinghe, D. T. 1989, *M.N.R.A.S.*, **236**, 31.
- Schmidt, G. D. 1988, Vatican Workshop, "*Polarized Radiation of Circumstellar Origin*", Ed. Coyne, G. V., Magalhaes, A. M., Moffat, A. F. J., Schulte-Ladbeck, R. E., Tapia, S., and Wickramasinghe, D. T., (Vatican Press), in press.
- Schmidt, G. D., Stockman, H. S., and Grandi, S. A. 1983, *Ap. J.*, **271**, 735.

- Schmidt, G. D., Stockman, H. S., and Grandi, S. A. 1986, *Ap. J.*, **300**, 804.
- Stockman, H. S., Foltz, C. B., Schmidt, G.D., and Tapia, S. 1983, **271**, 725.
- Wickramasinghe, D. T. 1988, Vatican Workshop, "*Polarized Radiation of Circumstellar Origin*", Ed. Coyne, G. V., Magalhaes, A. M., Moffat, A. F. J., Schulte-Ladbeck, R. E., Tapia, S., and Wickramasinghe, D. T., (Vatican Press), in press.
- Wickramasinghe, D. T. 1988, *IAU Colloquium 114 on White Dwarfs*, in press.
- Wickramasinghe, D. T., and Ferrario, L. 1988, *Ap. J.*, **334**, 412.
- Wickramasinghe, D. T., Ferrario, L., and Bailey, J. A. 1989, *Ap. J. (Letters)*, **342**, L35.
- Wickramasinghe, D. T., and Meggitt, S. M. A. 1985, *M. N. R. A. S.*, **216**, 857.

Chapter 5

A 56 MG Field at the Second Pole in VV Puppis

5.1 Abstract

We present phase dependent spectropolarimetric observations of VV Puppis which show, for the first time, cyclotron lines from both poles. The main and secondary emission regions have fields of 30.5 MG and 56 MG respectively. The second pole is visible at all phases and is located within 10° of the rotation axis of the white dwarf. The observations can be interpreted in terms of a dipole which is offset by $\approx 0.1R_{wd}$ from the center of the white dwarf in the direction of the dipole axis with the emission regions located near the foot points of closed field lines.

Subject headings: stars: magnetic – stars: variables – stars: white dwarfs – X-rays: binaries.

5.2 Introduction

We present phase dependent spectropolarimetric observations of VV Puppis which show, for the first time, resolvable cyclotron harmonic lines from both poles. The two emission regions have field strengths of 56 MG (secondary pole) and 30.5 MG (main pole) providing strong evidence in support of a model in which the dipole is offset from the center of the white dwarf.

5.3 Observations

Phase dependent circular spectropolarimetric observations of VV Puppis were obtained on 1988, Nov 29 and Nov 30 with the 3.9m Anglo-Australian Telescope (AAT) using the Pockels cell spectropolarimeter with the RGO spectrograph and the IPCS as detector (McLean *et al.* 1984). The wavelength coverage was $\lambda\lambda 3150 - 7300$ and the spectral resolution $\approx 10\text{\AA}$ FWHM. The exposures were 500 s long. We observed VV Puppis for one cycle on Nov 29 and for two consecutive cycles on Nov 30. We present the bright and faint phase data obtained on Nov 29 in Figures 5.1 and 5.2 respectively and the faint phase data for one of the cycles on Nov 30 in Figure 5.3. In Figures 5.1 and 5.2 we show the percentage of circular polarization and in Figure 5.3 the polarized flux (percentage of circular polarization multiplied by the flux). The second cycle obtained on Nov 30 gives very similar results to those on Nov 29 and it is not shown. The spectra in Figure 5.4 have been obtained by subtracting the faint phase spectra obtained on Nov 29 from the corresponding bright phase spectra in order to isolate the cyclotron contribution of the main, more active, pole.

The faint phase flux spectra obtained on Nov 29 (Fig. 5.2) and Nov 30 (Fig. 5.3) show cyclotron emission lines with maxima at 4200\AA , 5100\AA and 6700\AA . An inspection of the phase resolved spectra shows that the positions

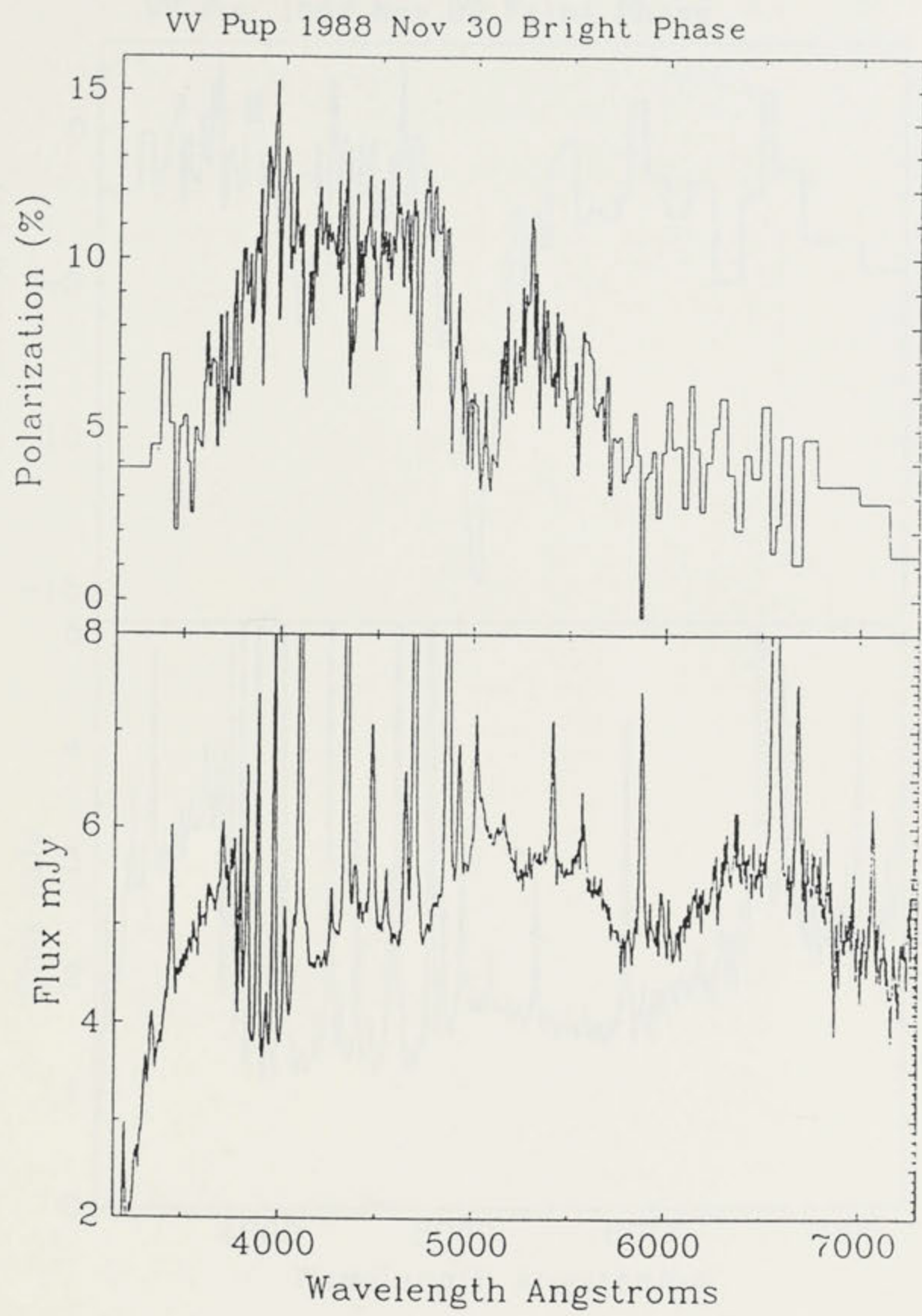


Figure 5.1: Bright Phase Spectra
AAT bright phase spectra of VV Puppis obtained on 1988, Nov 29.

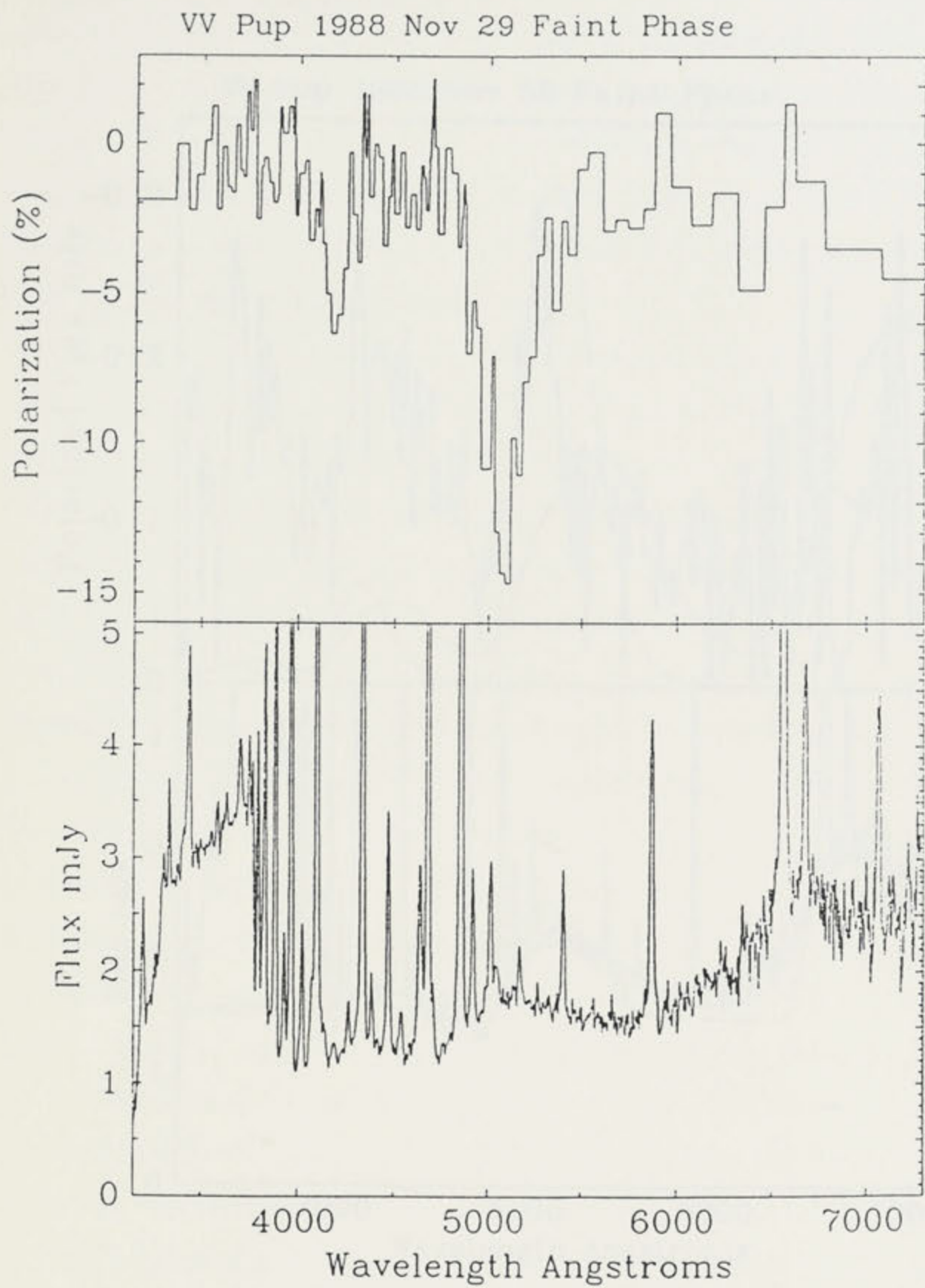


Figure 5.2: Faint Phase Spectra
AAT faint phase spectra of VV Puppis obtained on 1988, Nov 29.

VV Pup 1988 Nov 30 Faint Phase

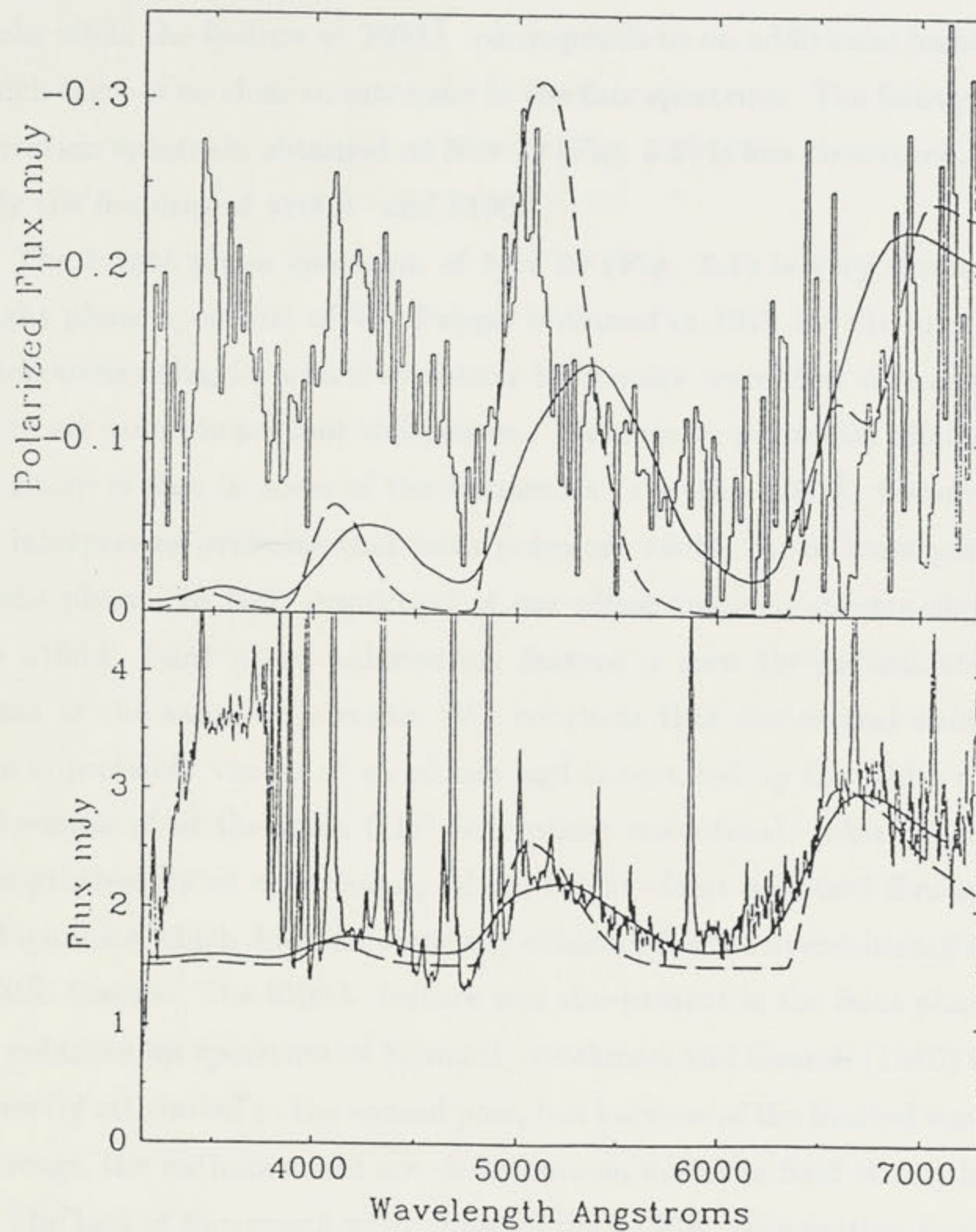


Figure 5.3: Faint Phase Spectra with Best Fits
AAT faint phase spectra of VV Puppis obtained on 1988, Nov 30. The solid and dashed lines are our best fit models for $T_e = 20$ keV and $T_e = 5$ keV respectively (see text).

of the harmonic peaks do not move with phase. The polarized flux spectrum obtained on Nov 30 (Fig. 5.3) shows similar structure with peaks at 3600Å, 4200Å and 5100Å. The features at 4200Å and 5100Å are close to the flux peaks while the feature at 3600Å corresponds to an additional harmonic for which there is no clear counterpart in the flux spectrum. The faint phase polarization spectrum obtained on Nov 29 (Fig. 5.2) is less structured, showing only the features at 4200Å and 5100Å.

The bright phase spectrum of Nov 29 (Fig. 5.1) is very similar to the bright phase spectrum of VV Puppis obtained in 1979 by Visvanathan and Wickramasinghe, in which cyclotron harmonics were first discovered, but there are some important differences. We note in particular that multiple structure is seen in some of the harmonics (*e.g.* the 5200Å feature) which we interpret as evidence that both poles are visible for at least part of the bright phase. In fact, inspection of our phase resolved spectra shows that the 5100Å faint phase polarization feature is seen throughout the bright phase at the same wavelength. We conclude that the second emission region is probably visible at *all* phases and is occulted by the white dwarf for a duration of at the most $0.1P$ (our phase resolution). This conclusion is strengthened by an examination of the bright-faint polarized flux spectrum in Figure 5.4 which does not show any evidence for the oversubtraction of the 5100Å feature. The 5100Å feature was also present in the faint phase circular polarization spectrum of Schmidt, Stockman and Grandi (1986) and was correctly attributed to the second pole, but because of the limited wavelength coverage, the authors could not determine an accurate field strength.

The lack of movement with phase of the 5100Å polarization feature and of individual harmonic lines in the flux spectra indicates that the angle θ between the line of sight and the field direction at the second spot does not change by more than 20° throughout the entire cycle (Wickramasinghe 1988). It follows that the colatitude of the secondary region is $\delta_2 \leq 10^\circ$ so that the spot is located close to the spin axis of the white dwarf. This angle is also consistent with the second emission region being visible at all phases if the

orbital inclination $i = 75^\circ$ (Meggitt and Wickramasinghe 1989, MW).

5.4 Discussion

The simplest of the models used to calculate cyclotron spectra are the constant Λ models (Wickramasinghe and Meggitt 1985) which assume uniform conditions within the shock but allow for optical depth effects. The emergent intensity along a given path length l is calculated as a function of electron temperature, T_e , viewing angle with respect to the field direction, θ , harmonic number, and optical depth parameter Λ . The flux spectrum in Figure 5.4, corresponding to the cyclotron emission spectrum from the main pole, shows cyclotron peaks at 4400\AA , 4900\AA , 5500\AA and 6350\AA which are shifted by $\approx 200\text{\AA}$ in comparison to the 1979 data. We have fitted constant Λ models to the data assuming a mean viewing angle $\theta = 85^\circ$ and found $B = 30.5$ MG, $T_e = 10$ keV and $\Lambda = 6 \times 10^5$. These results should be compared with the values $B = 32$ MG, $T_e = 10$ keV and $\Lambda = 1 \times 10^5$ deduced by Wickramasinghe and Meggitt (1982) from the 1979 bright phase data. The difference in field is significant and indicates that the centroid of the main emission region has migrated by $\approx 10^\circ$ toward the magnetic equator in response to the observed increase in accretion rate.

The calculated polarized flux is in general agreement with observations except for $\lambda > 6000\text{\AA}$ where the model shows too little polarization. We note also that the model predicts a polarized flux peak in between harmonics near 6000\AA while the observations appear to show a feature coincident with the flux peak at 6350\AA . We conclude that although the constant Λ model gives a reasonable fit to the overall energy distribution, the lack of detailed agreement with the polarized flux observations at long wavelengths points to the necessity for considering more sophisticated structured shock models.

The faint phase spectra in Figures 5.2 and 5.3 show energy distributions which rise steeply towards longer wavelengths (for $\lambda > 3700\text{\AA}$) up to the cut

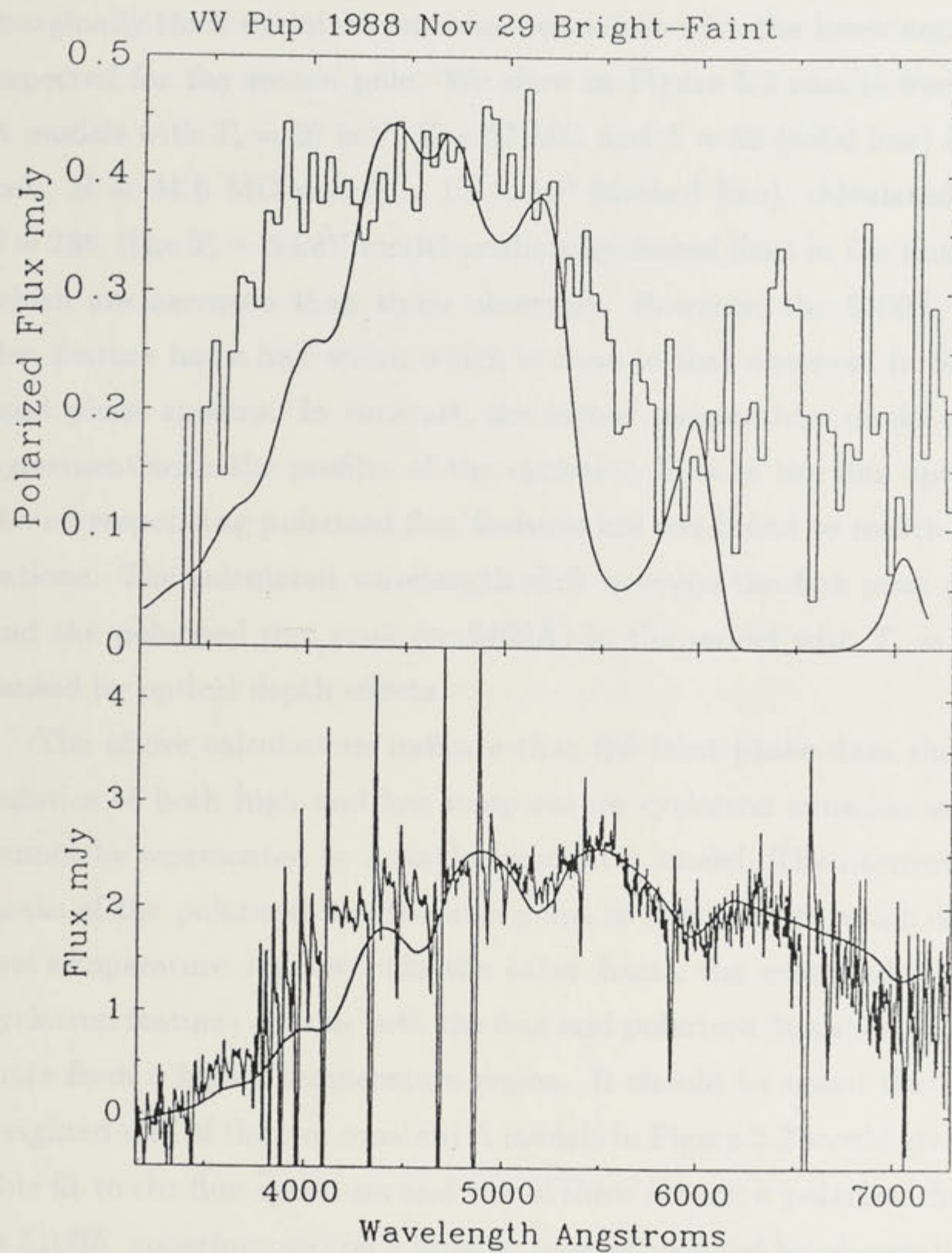


Figure 5.4: Bright Phase Spectra with Best Fit

Spectra of VV Puppis obtained by subtracting the faint phase spectra shown in Figure 5.2 from the bright phase spectra in Figure 5.1. The residual features at the emission lines result from the velocity shift between the bright and the faint phase spectra. The solid line is our best fit model (see text).

off in the observations at 7300\AA . The spectra are typical of optically thin or marginally thick cyclotron emission consistent with the lower accretion rate expected for the second pole. We show in Figure 5.3 results from constant Λ models with $T_e = 20$ keV, $B = 57$ MG and $\Lambda = 32$ (solid line) and $T_e = 5$ keV, $B = 54.6$ MG and $\Lambda = 1.1 \times 10^3$ (dashed line), calculated assuming $\theta = 75^\circ$. The $T_e = 5$ keV model predicts cyclotron lines in the flux spectrum which are narrower than those observed. However, the 5100\AA polarized flux feature has a half width which is close to that observed in both sets of faint phase spectra. In contrast, the higher temperature model gives good agreement with the profiles of the cyclotron lines in the flux spectra while the corresponding polarized flux features are too broad to match the observations. The calculated wavelength shift between the flux peak ($\approx 5100\text{\AA}$) and the polarized flux peak ($\approx 5400\text{\AA}$) in the model with $T_e = 20$ keV is caused by optical depth effects.

The above calculations indicate that the faint phase data show characteristics of both high and low temperature cyclotron emission regions and cannot be represented by a single constant Λ model. The narrowness of the peaks of the polarized flux features point to components which originate in low temperature regions. On the other hand, the extended wings of the cyclotron features seen in both the flux and polarized flux spectra must originate from a higher temperature region. It should be noted that a suitable weighted sum of the two constant Λ models in Figure 5.3 would give a reasonable fit to the flux spectrum and would show a narrow polarized flux feature at 5100\AA superimposed on a broader base as required by observations. Nevertheless, this model would still not predict the polarized flux peaks seen at shorter wavelengths (3600\AA and 4200\AA) in the data of Nov 30.

The present observations provide a direct determination of the magnetic fields at both shock regions on the white dwarf surface and place strong constraints on the field structure. If we assume that the two spots are located near the foot points of closed field lines (MW; Ferrario, Wickramasinghe, and Tuohy 1989), then the unequal field strength at the spots indicate that the

dipole must be offset from the center of the star. The observed field strengths can be explained if the dipole is displaced by $\approx 0.1R_{wd}$ in the direction of the dipole axis. With this offset, the effective centered dipole polar field strength is about 40 MG. The colatitude of the spots ($\delta_1 = 145^\circ$ [MW], and $\delta_2 \leq 10^\circ$) imply that they are separated by $\approx 145^\circ - 155^\circ$ on the surface of the white dwarf. The assumption of accretion along closed field lines would then place the dipole axis within $\approx 20^\circ$ of the spin axis. The model is similar to that recently proposed by MW on the basis of an analysis of the linear polarization angle data. The field structure deduced for VV Puppis from cyclotron lines is similar to that deduced for AM Herculis on the basis of Zeeman spectra (Wickramasinghe and Martin 1985). Both systems show evidence for an offset dipole and the pole having the weaker field is located on the hemisphere that faces the companion star.

Finally, we note that there are now two systems (VV Puppis and EXO 033319 - 2554.2) which show evidence for field strengths that are considerably higher than previously deduced for AM Her variables (Schmidt 1988). Following our results on VV Puppis it is likely that the large difference in field strength between the two poles in EXO 033319 - 2554.2 (56 MG and 28 MG [Ferrario *et al.* 1989]) can also be explained in terms of an offset dipole. This implies that for both these systems the effective centered dipole polar field strength is about 40 MG, much smaller than that of the stronger pole.

We thank Gary Schmidt for useful comments. L.F. acknowledges support from an Australian National University postgraduate scholarship.

5.5 References

- Ferrario, L., Wickramasinghe, D. T., Bailey, J. A., Tuohy, I. R., and Hough, J. H. 1989, *Ap. J.*, **337**, 832.
- Ferrario, L., Wickramasinghe, D. T., and Tuohy, I. R. 1989, *Ap. J.*, in press.
- McLean, I. S., Heathcote, S. R., Fordham, M. J., and Shortridge, K. 1984 *M.N.R.A.S.*, **209**, 655.
- Meggitt, S. M. A., and Wickramasinghe, D. T. 1989, *M.N.R.A.S.*, **236**, 31 (MW).
- Schmidt, G. D. 1988, Vatican Workshop, "*Polarized Radiation of Circumstellar Origin*", Ed. Coyne, G. V. *et al.*, (Vatican Press), in press.
- Schmidt, G. D., Stockman, H. S., and Grandi, S. A. 1986, *Ap. J.*, **300**, 804.
- Visvanathan, N. V., and Wickramasinghe, D. T. 1979, *Nature*, **281**, 47.
- Wickramasinghe, D. T. 1988, Vatican Workshop, "*Polarized Radiation of Circumstellar Origin*", Ed. Coyne, G. V. *et al.*, (Vatican Press), in press.
- Wickramasinghe, D. T., and Martin, B. 1985, *M.N.R.A.S.*, **212**, 353.
- Wickramasinghe, D. T., and Meggitt, S. M. A. 1982, *M.N.R.A.S.*, **198**, 975.
- Wickramasinghe, D. T., and Meggitt, S. M. A. 1985, *M.N.R.A.S.*, **216**, 857.

Chapter 6

EXO 033319–2554.2: An Eclipsing AM Herculis System Showing Cyclotron Emission Features

6.1 Abstract

We report spectroscopic and circular polarization observations of the soft X-ray binary EXO 033319–2554.2 which confirm it as a member of the AM Herculis class with properties similar to VV Puppis. Circular polarization reaching 10% in the blue and less than or equal to 2% in the *I*-band is seen during the bright phase which lasts for 70 minutes of the 126.5 minute orbital cycle. The optical light curve exhibits a narrow eclipse due to the companion star, lasting about 8 minutes and occurring towards the end of the bright phase. The radial velocity curves show a sharp discontinuity due to an eclipse of the line forming region by the accretion funnel and the white dwarf. Broad resolvable and variable cyclotron harmonics are seen during the bright phase. At the centre of the bright phase, the emission peaks are located near 4200Å, 5200Å and 6550Å, corresponding to a magnetic field $B \approx 5.6 \times 10^7$ Gauss and a temperature $T = 20$ keV. Detailed theoretical models suggest the presence of a second emission region of field strength

$B \approx 2.8 \times 10^7$ Gauss which can be seen towards the end of the bright phase. We deduce a mass ratio of ≈ 0.1 and estimate an orbital inclination of $\approx 88^\circ$ and a colatitude of $\approx 14^\circ$ for the main emission region, assuming that it is a point source and that the duration of the bright phase is $\Delta\phi \approx 0.55$.

Subject headings: eclipsing binaries – polarization – stars: individual (EXO 033319–2554.2) – stars: magnetic – stars: white dwarfs – X-rays: binaries.

One of the magnetic stars that belong to the category of stars with the end of the bright phase. Brownman and Thomas (1977) identified EXO 033319–2554.2 with an 18° magnetic dipole moment and a variable blue continuum and emission lines similar to that reported from an AM Her-type system during a low state.

In this paper we report spectroscopic and photometric observations of EXO 033319–2554.2 obtained when the system was in a bright state ($V_{\text{max}} = 14$) close to the end of optical identification. The photometric observations confirm its magnetic nature through the detection of periodic polarization. After polarization, the spectroscopic data show that EXO 033319–2554.2 is the smallest AM Her system in which cyclotron harmonics in the optical spectrum similar to those first discovered by Vignani by Vignani and Warganowich (1970). Preliminary results of our observations have been reported by Bailey et al. (1987) and Brown et al. (1988). We note that cyclotron features have been independently reported by Brownman, Thomas and Schwarz (1987).

6.3 Observations

6.3.1 Polarimetry and Photometry

Ultraviolet polarimetry and photometry of EXO 033319–2554.2 were obtained on 1977 Dec 16 using the Mark II Helios 1 Telescope (Bailey 1976) for the

6.2 Introduction

EXO 033319-2554.2 was recently reported to be a soft X-ray source with a period of 126.7 minutes (Giommi *et al.* 1987; Osborne *et al.* 1988). Its X-ray light curve is similar to that of VV Puppis showing 100% modulation, with a bright phase which lasts for ≈ 0.56 of the orbital period. A narrow eclipse, due to the companion star and lasting for ≈ 8 minutes, is seen near the end of the bright phase. Beuermann and Thomas (1987) identified EXO 033319-2554.2 with an 18th magnitude object showing a variable blue continuum and emission lines similar to that expected from an AM Herculis system during a low state.

In this paper we report spectroscopic and polarimetric observations of EXO 033319 - 2554.2 obtained when the system was in a brighter state ($V_{\max} \approx 17$) than at the time of optical identification. The polarimetric observations confirm its magnetic nature through the detection of circular polarization. More interestingly, the spectroscopic data show that EXO 033319-2554.2 is the second AM Her system to exhibit cyclotron harmonics in its optical spectrum similar to those first discovered in VV Puppis by Visvanathan and Wickramasinghe (1979). Preliminary results of our observations have been reported in Bailey *et al.* (1987) and Ferrario *et al.* (1988). We note that cyclotron features have been independently reported by Beuermann, Thomas and Schwöpe (1987).

6.3 Observations

6.3.1 Polarimetry and Photometry

Circular polarimetry and photometry of EXO 033319-2554.2 were obtained on 1987 Dec 15 using the Mark 2 Hatfield Polarimeter (Bailey 1988a) on the

3.9m Anglo-Australian Telescope (AAT). Simultaneous observations were obtained in five bands with wavelength ranges 3400 – 4800Å, 3400 – 5300Å, 4900 – 5700Å, 5500 – 8400Å and 6500 – 8400Å. The circular polarization data for three of the five bands are plotted in Figure 6.1. The 3400 – 4800Å band gives very similar results to the 3400 – 5300Å band, while the 4900 – 5700Å data are of poor signal to noise ratio. Just over one cycle was observed, but thin cloud was present for part of the observation (this caused the large errors near $\phi = 0.3$), so we cannot make use of the photometric data over the whole cycle. However the light curve of the eclipse was unaffected and is plotted in Figure 6.2 for two of the bands.

Photometry in the infrared *J* band was obtained on 1987 Dec 3 using the Infrared Photometer Spectrometer (IRPS) on the AAT. One cycle was observed and is plotted in Figure 6.3.

6.3.2 Spectroscopy

Spectroscopy of EXO 033319–2554.2 was obtained on 1987 Nov 27 using the AAT under photometric conditions. The Royal Greenwich Observatory spectrograph was used with a GEC CCD as a detector to give a resolution of $\approx 6\text{Å}$ FWHM. Two consecutive and overlapping sets of spectra were obtained: a blue set of 24 images covering the wavelength range 3947–5757Å, and a red set of 25 images covering the range 4987–6797Å. Both sets spanned approximately one binary cycle, and the time resolution was either 300 s or 120 s, with a CCD read-out time in between spectra of 60 s. The flat-fielded and sky-subtracted spectra were converted to AB magnitudes using calibration curves derived from observations of bright standards tabulated in Taylor (1984). Examination of the night sky lines was undertaken to confirm that the zero point of velocity of the two sets of spectra remained stable to less than or equal to 7 km s^{-1} .

Recurrent eclipses are present in our spectra toward the end of the bright phase, and the centres of these events have been used to define phase zero

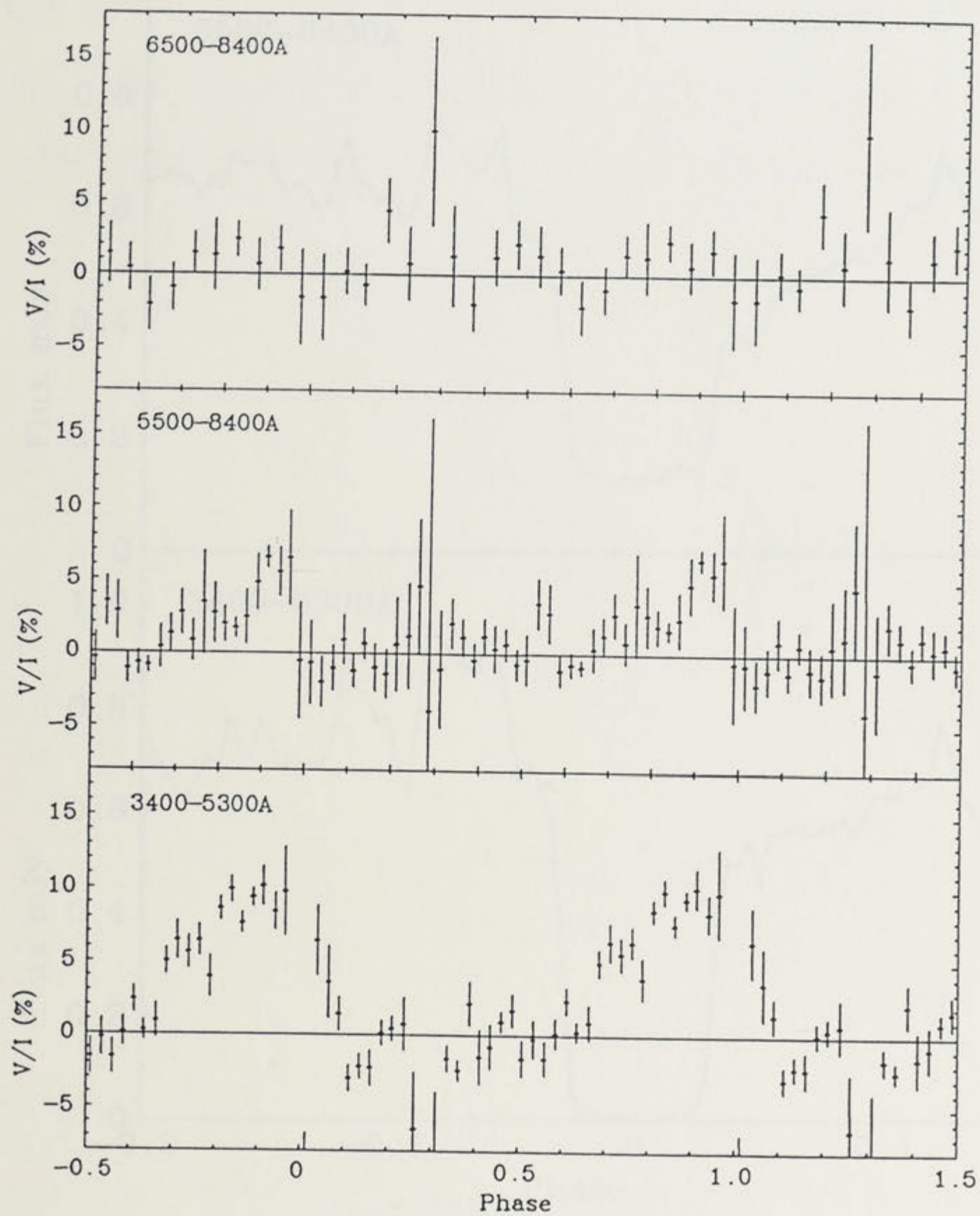


Figure 6.1: Circular Polarization Data
 Circular polarization data for EXO 033319-2554.2 obtained on 1987 Dec 15. The polarization in the blue band reaches $\approx 10\%$ and there is a reversal in sign near $\phi = 0.1$.

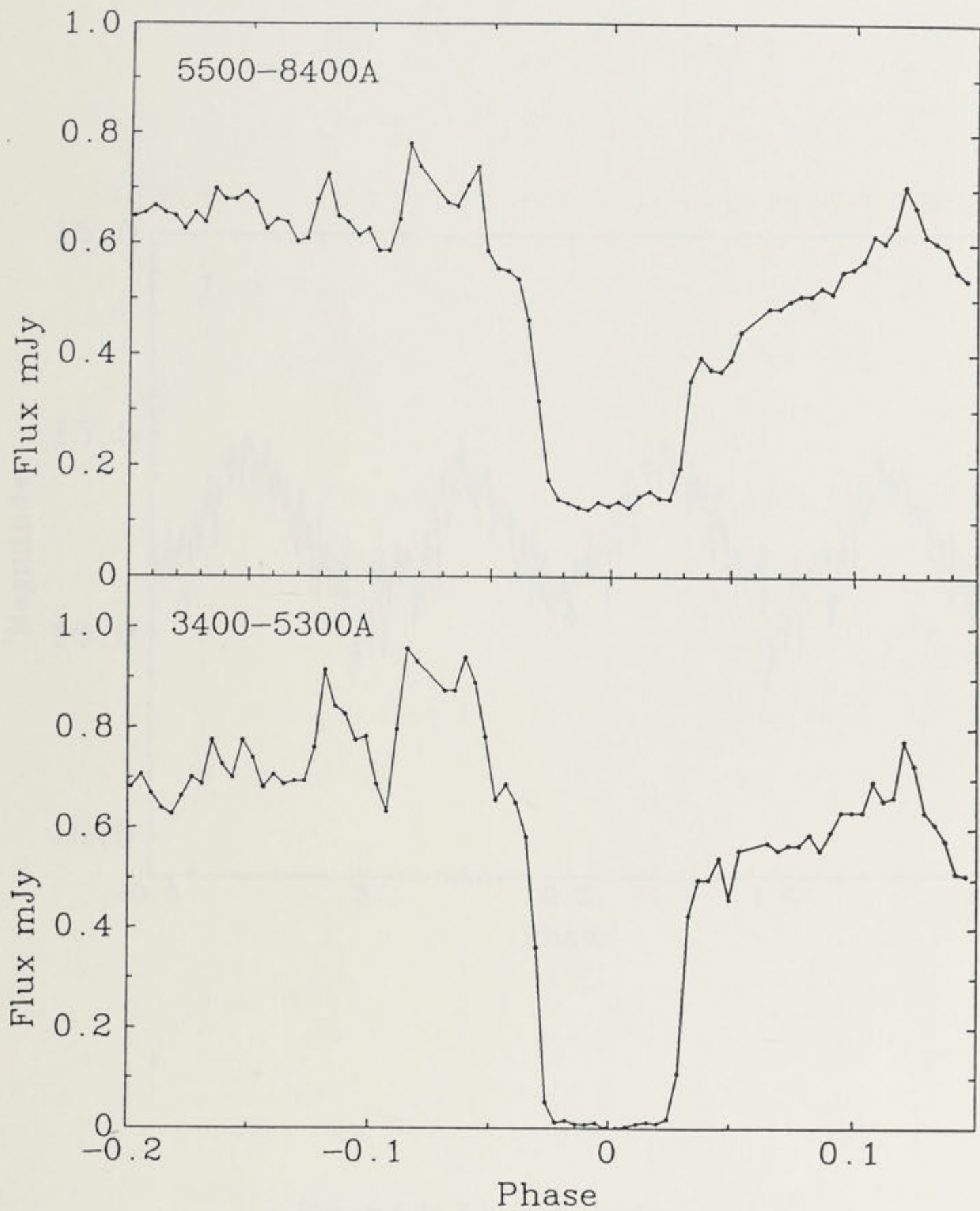


Figure 6.2: Light Curves of the Eclipse
 Light curves of the eclipse of EXO 033319-2554.2 measured in two bands on 1987 Dec 15. The ingress and egress are not resolved, implying durations of less than or equal to 32 seconds. Note that the eclipse appears to be total in the blue band.

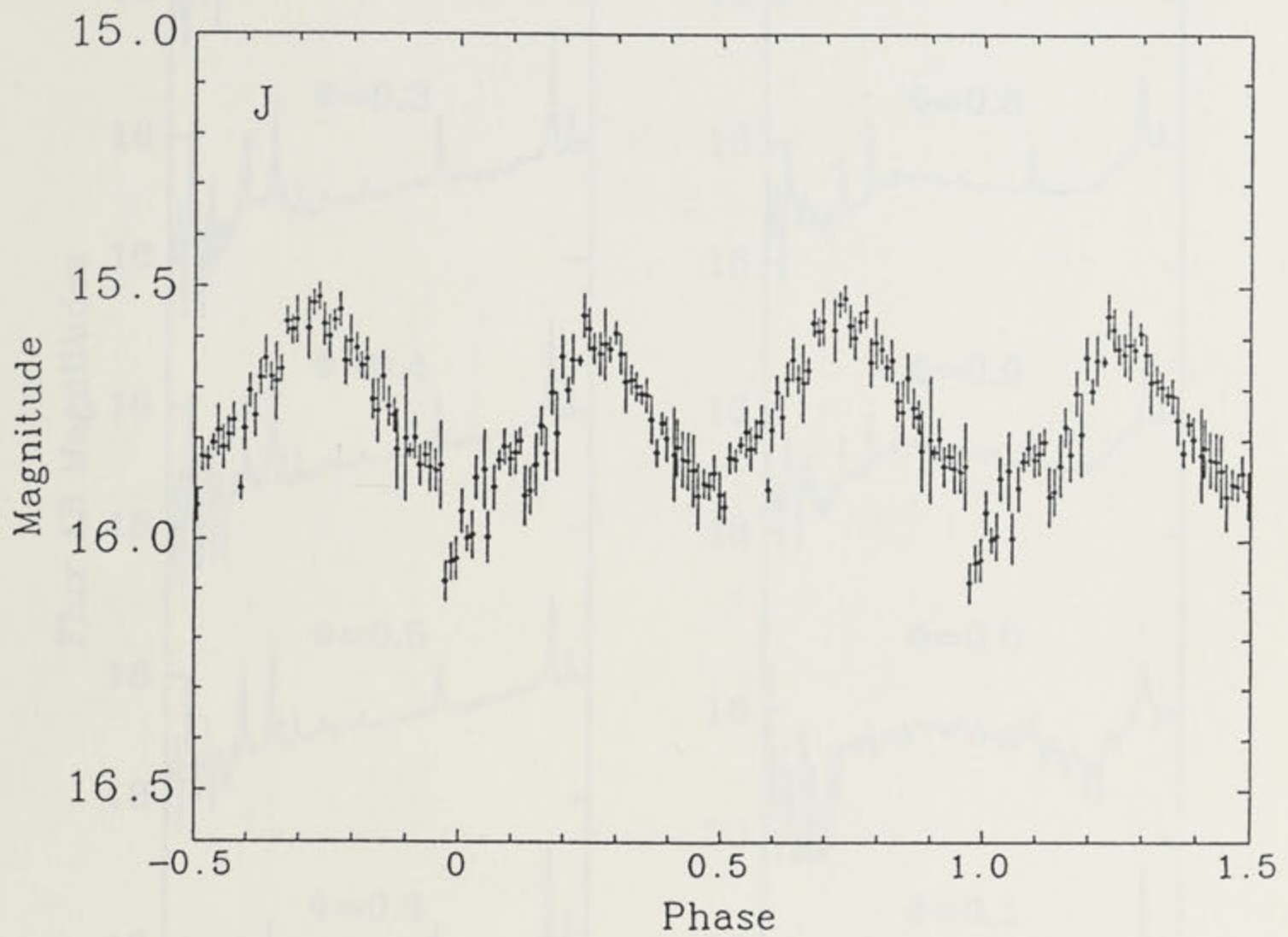


Figure 6.3: *J*-band Light Curve

J-band light curve of EXO 033319-2554.2 obtained on 1987 Dec 3. The modulation is mainly due to the ellipsoidal light variations of the Roche-lobe filling M dwarf.

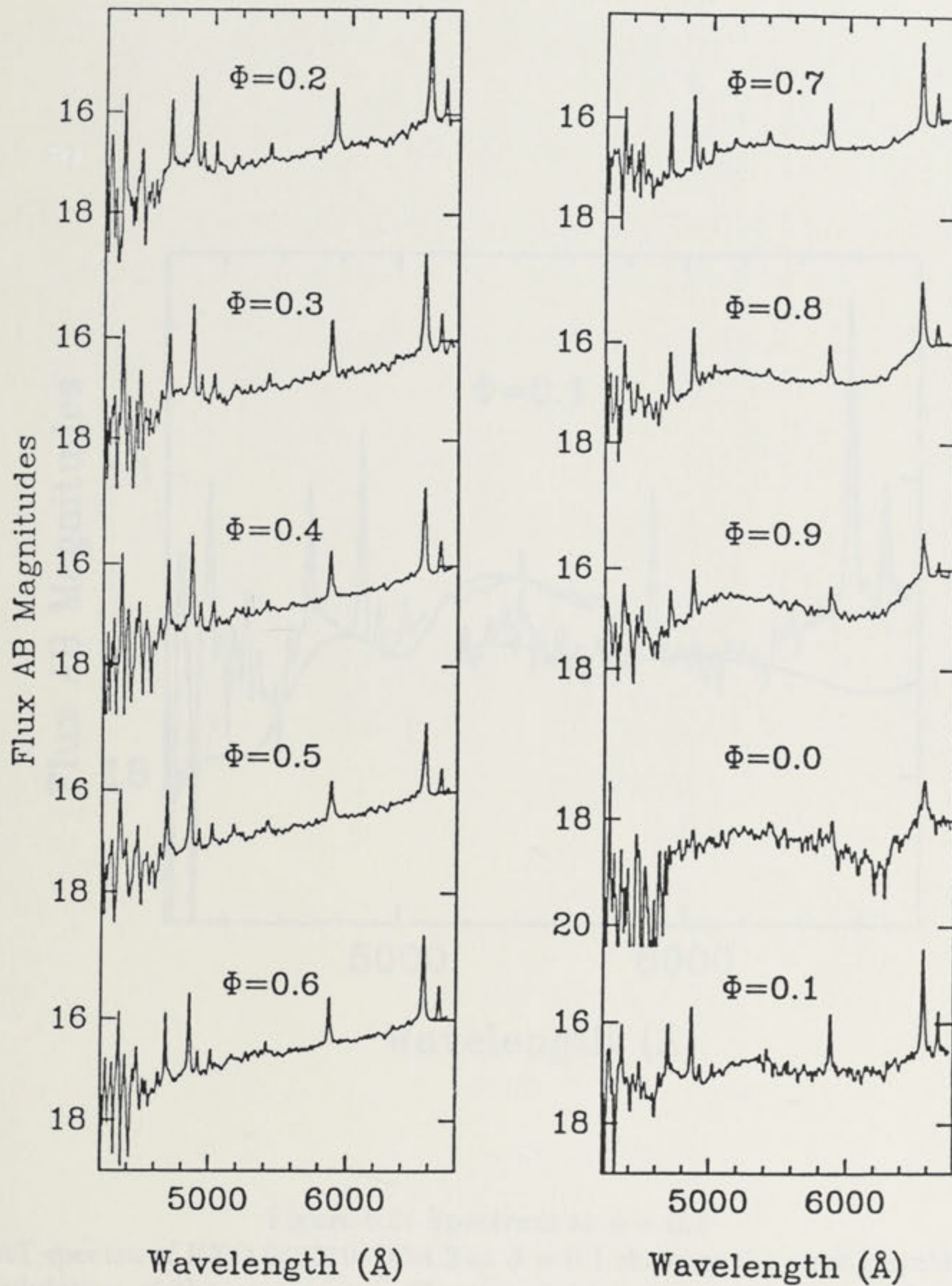


Figure 6.4: Spectra
 AAT spectra of EXO 033319-2554.2 obtained on 1987 Nov 27. The blue and red spectra have been summed and merged into 10 phase bins. Prominent cyclotron emission features are visible near 5200Å and 6550Å from $\phi = 0.7$ to $\phi = 0.9$.

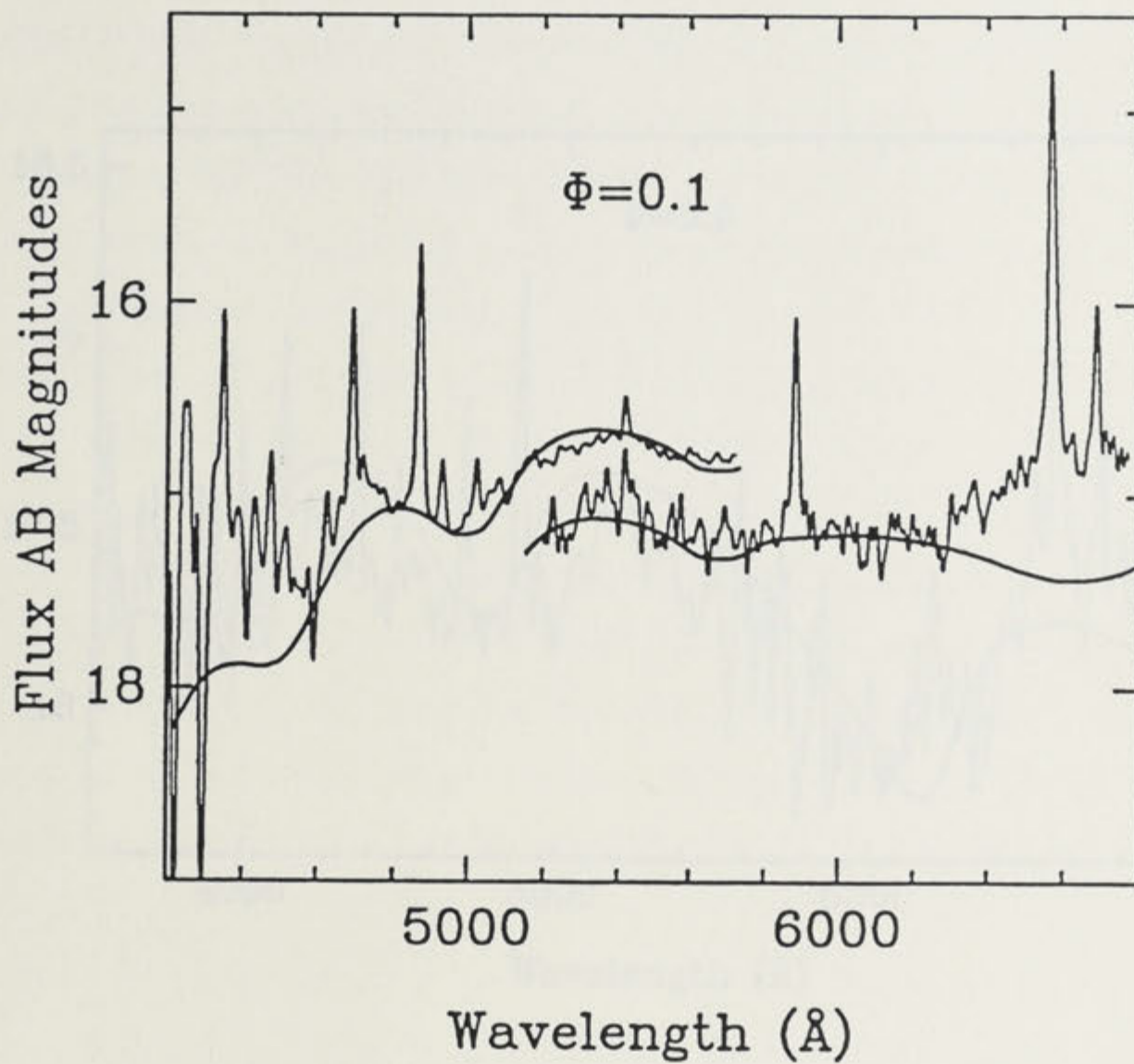


Figure 6.5: Spectrum at $\phi = 0.1$
 AAT spectra of EXO 033319-2554.2 at $\phi = 0.1$ showing the strong cyclotron modulation of the continuum. The two overlapping spectra were obtained on consecutive binary cycles and are displaced by an arbitrary amount for clarity. The magnitude scale corresponds to the blue spectrum. The solid line represents our best fit for a magnetic field $B = 2.8 \times 10^7$ Gauss and $\theta = 90^\circ$.

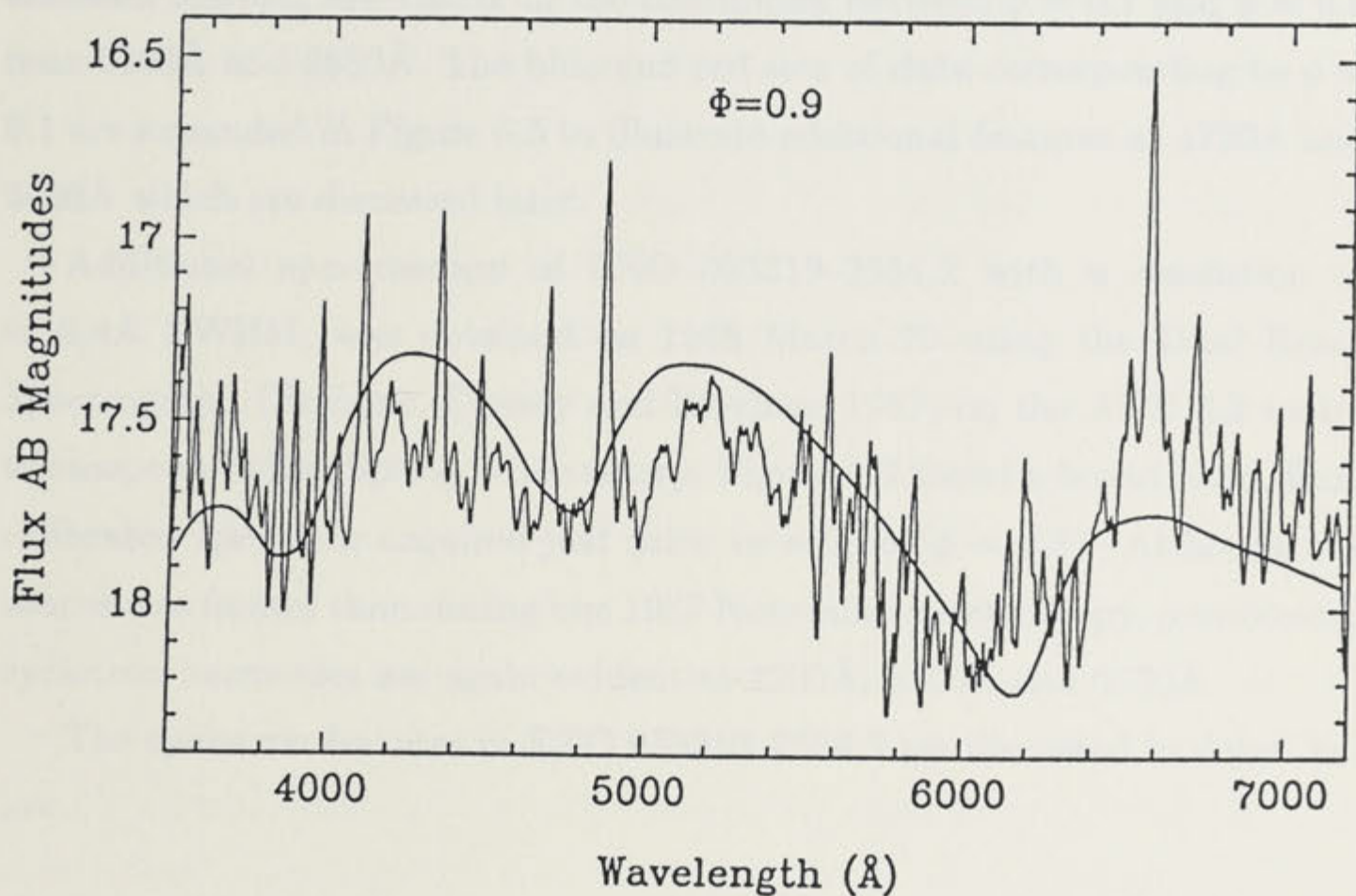


Figure 6.6: Broad Band Spectrum at $\phi = 0.9$
 A broad band spectrum of EXO 033319-2554.2 acquired on 1988, March 20 using the Dual Beam Spectrograph on the ANU 2.3 metre telescope. Broad cyclotron harmonics are evident at 4200Å, 5200Å and 6550Å. The increased noise in the spectrum near 6000Å is due to the presence of a dichroic in the spectrograph. The solid line represents our best fit for a magnetic field $B = 5.6 \times 10^7$ Gauss and $\theta = 75^\circ$.

in our data. The two sets of overlapping spectra have been summed into 10 phase bins covering a single orbital period. The blue and red sets of spectra have been merged since the continuum was found to be highly repeatable for all 10 spectra in the overlap region ($\Delta\lambda \approx 770\text{\AA}$). The ten phase-resolved spectra are displayed in Figure 6.4, and show strong Balmer lines, HeI lines and HeII $\lambda 4686$ in emission. Furthermore, broad and resolvable cyclotron emission features are visible in the continuum between $\phi = 0.7$ and $\phi = 0.9$ near 5200\AA and 6550\AA . The blue and red sets of data corresponding to $\phi = 0.1$ are expanded in Figure 6.5 to illustrate additional features at 4720\AA and 5650\AA which are discussed later.

Additional spectroscopy of EXO 033319-2554.2 with a resolution of $\approx 6.4\text{\AA}$ FWHM, was obtained on 1988 March 20 using the Dual Beam Spectrograph (Rodgers, Conroy and Bloxham 1987) on the ANU 2.3 metre telescope at Siding Spring Observatory. Figure 6.6 shows a broad band, flux-calibrated spectrum acquired just prior to eclipse ($\phi = 0.9$). Although the source was fainter than during our 1987 November spectroscopy, pronounced cyclotron harmonics are again evident at 4200\AA , 5200\AA and 6550\AA .

The cyclotron features in EXO 033319-2554.2 are discussed in detail below.

6.4 Results and Discussion

6.4.1 Polarization Behaviour

The polarization data in Figure 6.1 show circular polarization reaching about 10% in the blue ($3400 - 5300\text{\AA}$) band. The polarization lasts from about $\phi = 0.65$ to $\phi = 0.2$. Furthermore, a reversal of circular polarization sign, which is similar to that seen in VV Pup, is evident from $\phi = 0.1$ to $\phi = 0.2$. The longer wavelength bands show lower polarization, with no significant polarization ($\leq 2\%$) being detected in the $6500 - 8400\text{\AA}$ band.

The presence of strong circular polarization confirms that the object is of AM Herculis type. The polarization is observed during the X-ray and optical bright phase as expected for a system in which the emission region passes behind the white dwarf for part of the cycle. The fact that the polarization is observed predominantly in the blue is unusual for AM Herculis binaries. Most systems have their peak polarized flux in the red or near infrared region of the spectrum (Bailey 1988b), the exception being VV Pup with peak polarized flux at about $0.4\mu\text{m}$. It seems likely that the polarized flux in EXO 033319–2554.2 peaks even further into the UV as we see substantial polarization only in the bluest bands observed, whereas VV Pup has substantial polarization out to the *I* band ($0.8\mu\text{m}$) and other AM Her systems have polarization out to the *H* band ($1.6\mu\text{m}$). This suggests that the polar field strengths in VV Puppis and EXO 033319–2554.2 are higher than in the other systems.

The polarization curve can be explained either in terms of a single emission region or two emission regions on the surface of the white dwarf. In the case of a single eclipsing cyclotron emission region, the reversal in the sign of the circular polarization at $\phi = 0.1$ implies that the field is inclined to the stellar surface and that the average angle θ between the field direction and the line of sight crosses 90° at this phase. The absence of a similar reversal near eclipse egress suggests that the field leads the emitting region as in VV Puppis, and that the average angle between the line of sight and the magnetic field lines is less than 90° at this phase. By analogy with VV Puppis, we expect a narrow linear polarization pulse at $\phi = 0.1$ and a broad pulse near $\phi = 0.7$ (Wickramasinghe and Ferrario 1987, 1988).

Alternatively, the reversal in the sign of the circular polarization could be explained by the presence of a second emission region of opposite field polarity on the surface of the white dwarf. In this case the main emission region would contribute polarization of positive sign and the secondary region polarization of negative sign to the observed polarization curve. The contribution from the main emission region dominates between $\phi = 0.7$ and $\phi = 0.9$, while the secondary region becomes dominant between $\phi = 0.1$ and

$\phi = 0.2$, and results in a reversal in the sign of circular polarization. Since the two emission regions are unlikely to be diametrically opposite to each other, they are expected to be simultaneously visible for part of the orbital cycle. Support for this idea comes from a comparison of the phase dependent circular polarization data in the 5500–8400Å and 3400–5300Å bands, which shows that the phase of the second zero crossing of the circular polarization changes from $\phi = 0.95$ to $\phi = 0.1$ between the two bands. This could result from the addition of two emission regions which contribute different signs of circular polarization but which have different spectral energy distributions at the phases when they are simultaneously visible (Wickramasinghe 1988).

6.4.2 *Eclipse Properties*

The sharp eclipses seen in the optical are coincident in phase with the eclipses observed at X-ray wavelengths and clearly indicate the presence of an eclipse by the companion star rather than an absorption dip due to the stream (the other possibility discussed by Osborne *et al.* 1988).

In Table 6.1 we list timings of mid-eclipse for the two eclipses observed during the AAT spectroscopy run, and the one eclipse observed during the polarimetry observations. In addition, an approximate timing can be derived for the shallow eclipse feature seen in the *J* band light curve. Together with the two X-ray eclipse timings reported by Osborne *et al.* (1988) we derive the following ephemeris:

$$T_{\min} = \text{HJD } 2445567.17697(10) + 0.087865393(7) E$$

The period of 126.53 minutes is the longest period known for the short period group of cataclysmic variables, and lies just inside the nominal 2-3 hour "period gap". The next longest directly measured period is 115.5 minutes for EXO 023432 – 5232.3 (Bailey *et al.* 1988) while YZ Cnc has a period of 126 minutes inferred from its superhump period (Ritter 1984).

The eclipse light curves in Figure 6.2 show that the eclipse ingress and

TABLE 6.1: TIMINGS OF MID-ECLIPSE FOR EXO 033319-2554.2

Cycle	HJD	Error	O-C ^a
0	2445567.17697	0.00016	0.00000
10013	6446.97317	0.00016	0.00002
17754	7127.13880	0.00030	-0.00030
17755	7127.22710	0.00030	0.00010
17820	7132.93600	0.00100	-0.00200
17958	7145.06370	0.00006	0.00000

^a Observed-Calculated

egress are comparable to or faster than our time resolution of 32 seconds, implying an eclipsed object of white dwarf dimensions or smaller. The eclipse duration, measured between the mid-points of the ingress and egress is 0.062 in phase or 7.8 minutes. For an eclipse by a Roche lobe filling secondary, the eclipse duration determines a relation between the mass ratio $q = M_{rd}/M_{wd}$ and the inclination i , where M_{rd} and M_{wd} are the masses of the red dwarf and the white dwarf respectively. Using the observed eclipse half angle of $11^\circ.16$ and the method described by Chanan, Middleditch and Nelson (1976) we derive the $q - i$ relation given in Table 6.2. We have also tabulated in Table 6.2 the corresponding values of the colatitude δ of the main emission region derived from the relation $\cot i = -\cos(\Delta\phi_B\pi)\tan\delta$ (Wickramasinghe and Meggitt 1982) for a point source cyclotron emission region, using $\Delta\phi_B = 0.55$ for the duration of the bright phase. The smallest value of q which can produce the observed eclipse duration is 0.094. Recent determinations of q for short period cataclysmic binaries suggest that its value is likely to be in the range between 0.1 and 0.25, and thus $i \approx 88 - 80^\circ$ and $\delta \approx 14 - 48^\circ$. We argue in §6.4.5 that the mass ratio is likely to be near the lower limit of this range.

TABLE 6.2: ECLIPSE PARAMETERS FOR EXO 033319-2554.2

q	$i(^{\circ})$	$\delta(^{\circ})$
0.094	90.0	...
0.10	87.8	13.8
0.15	83.8	34.8
0.20	81.8	42.7
0.25	80.3	47.5
0.30	79.2	50.6
0.50	76.1	57.7

6.4.3 *The Secondary Star*

The eclipse in the blue is extremely deep. This is a distinctive feature of eclipsing AM Herculis binaries and indicates that most of the radiation arises very close to the white dwarf and is totally eclipsed by the companion star. At longer wavelengths, however, there is a more substantial residual flux at mid-eclipse, and in the J band light curve the eclipse depth is only about 0.2 magnitudes. This change with wavelength can be understood as due to the increasing contribution of the red dwarf secondary at longer wavelengths. The magnitudes at mid-eclipse are approximately $V = 20.4$, $I = 17.7$ and $J = 16.0$. The first two values are approximate only as they are estimated from observations in broader bands than the standard V and I bands. The colours are consistent with those of an M4 dwarf.

The J band light curve (Figure 6.3) shows an approximately sinusoidal light curve with minima at $\phi = 0.0$ and $\phi = 0.5$ and an amplitude of about 0.35 magnitude. This suggests that it is dominated by the ellipsoidal light curve of the Roche lobe filling secondary. The presence of a shallow eclipse as well as the departure of the light curve from a sinusoid shows that some light still originates from the vicinity of the white dwarf at this wavelength.

The $J-K$ colour of an M4 dwarf is about 0.9, so we can estimate $K = 14.9$ (at the mean value of the ellipsoidal variations) and $V - K = 5.3$. Together with an assumed secondary mass of $0.1M_{\odot}$ we then use the method of Bailey (1981) to obtain a distance of 208 ± 40 pc. The distance scales as $M_{rd}^{1/3}$ for other secondary masses.

Finally, we point out that although important physical parameters concerning the secondary star could be obtained from the mid-eclipse spectrum, we have not found any evidence in our data for absorption features characteristic of a late-type companion.

6.4.4 *Radial Velocity Curves*

The spectra of AM Herculis type systems are characterized by prominent emission lines which are highly modulated in velocity and amplitude with binary phase. Their profiles are usually extremely complex but at the dispersion available to us, it is only possible to divide them into a broad and a medium velocity component (*cf.* Rosen, Mason and Córdova 1986). The observed emission line profiles are a consequence of a superposition of different line components formed in distinct regions of the accretion flow. We believe that both these components originate from the material that is magnetically channelled, with the broad component arising from a region closer to the white dwarf surface. For a review of the accretion processes in AM Herculis systems see Liebert and Stockman (1985).

In order to establish positions and widths of these components in our AAT spectroscopy, the profiles of $H\alpha$, $H\beta$ and $HeII \lambda 4686$ have been fitted with double gaussian curves on a parabolic background. The results for all three lines are identical and are illustrated in Figure 6.7 where broad and medium velocity components of $H\alpha$ are plotted against orbital phase. We note that there is a phase lag of $\Delta\phi \approx 0.1 - 0.2$ between the broad and medium components, strengthening the hypothesis that they originate from different regions of the curved accretion flow. More interestingly, there is

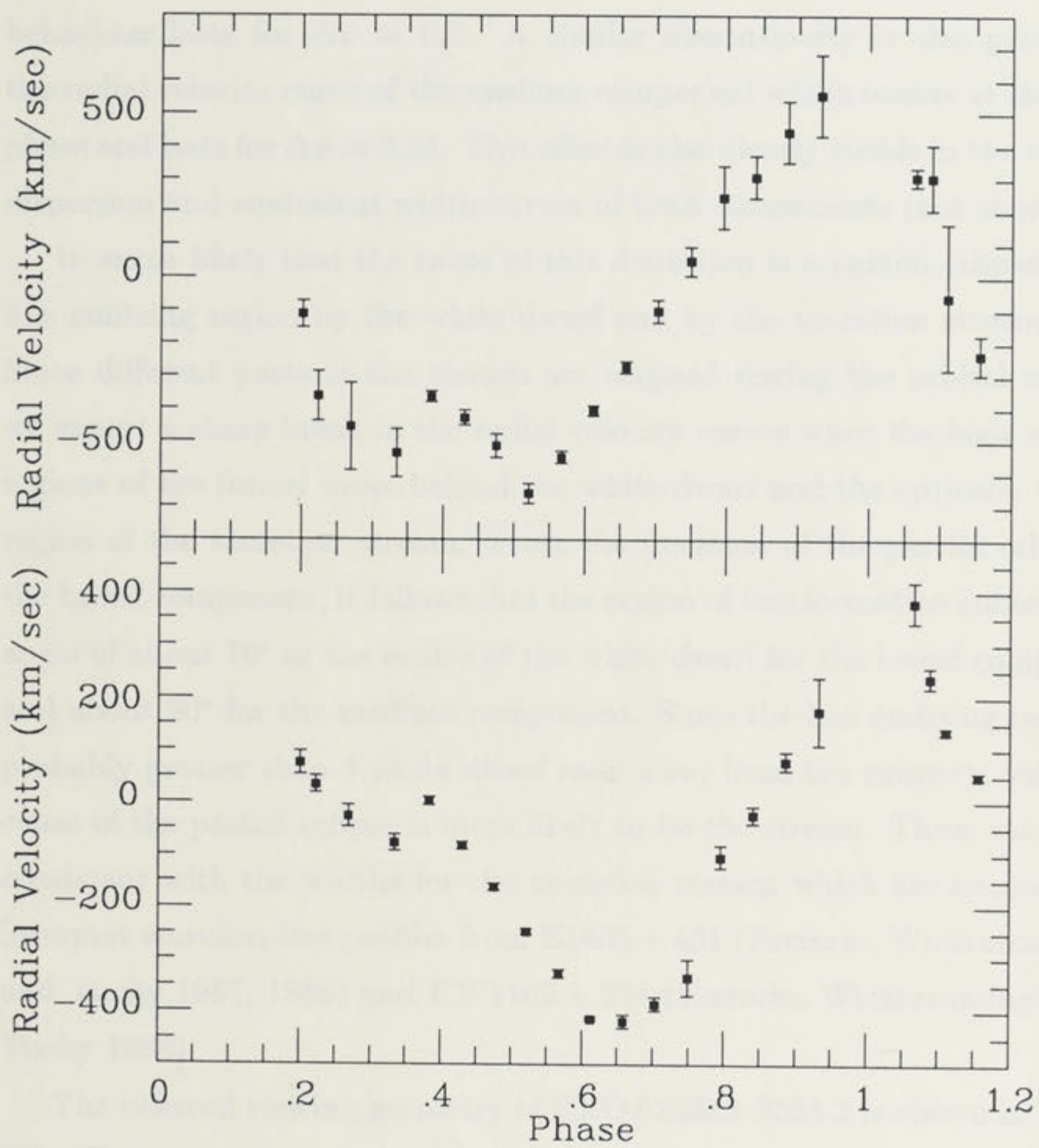


Figure 6.7: Radial Velocity Curves

Radial velocity curves of $H\alpha$ for EXO 033319-2554.2. Upper panel: broad velocity component. Lower panel: medium velocity component. The phase lag between the two curves indicates a curved accretion stream. A pronounced discontinuity is visible for both components near $\phi = 0.35$.

clear evidence for a departure from the sinusoidal behaviour expected for the radial velocity curves. For the broad component, a discontinuity ($\Delta V \approx 200 \text{ km s}^{-1}$) is seen at $\phi = 0.35$ and the deviation from the expected sinusoidal behaviour lasts for $\Delta\phi \approx 0.2$. A similar discontinuity is also present in the radial velocity curve of the medium component which occurs at the same phase and lasts for $\Delta\phi \approx 0.25$. This effect is also clearly visible in the velocity dispersion and equivalent width curves of both components (not shown).

It seems likely that the cause of this distortion is a partial eclipse of the line emitting region by the white dwarf and by the accretion stream itself. Since different parts of the stream are eclipsed during the orbital motion, we expect a sharp break in the radial velocity curves when the high velocity regions of the funnel move behind the white dwarf and the optically thicker region of the accretion stream. From the duration of the partial eclipse of the broad component, it follows that the region of line formation subtends an angle of about 70° at the centre of the white dwarf for the broad component and about 90° for the medium component. Since the line emitting region is probably greater than 5 white dwarf radii away from the primary, the main cause of the partial eclipse is more likely to be the stream. These values are consistent with the widths for the accretion stream which are necessary to interpret emission line profiles from E1405 – 451 (Ferrario, Wickramasinghe and Tuohy 1987, 1988) and CW1103 + 254 (Ferrario, Wickramasinghe and Tuohy 1988).

The inferred viewing geometry of EXO 033319–2554.2 is shown in Figure 6.8. This geometry is based on our results pertaining to the polarization, eclipsing, and radial velocity behaviour of this system.

6.4.5 *The Cyclotron Spectrum*

The broad features seen in the continuum during the bright phase of EXO 033319 – 2554.2 are reminiscent of similar features sometimes seen in the continuum of VV Puppis. The features in VV Puppis were interpreted as

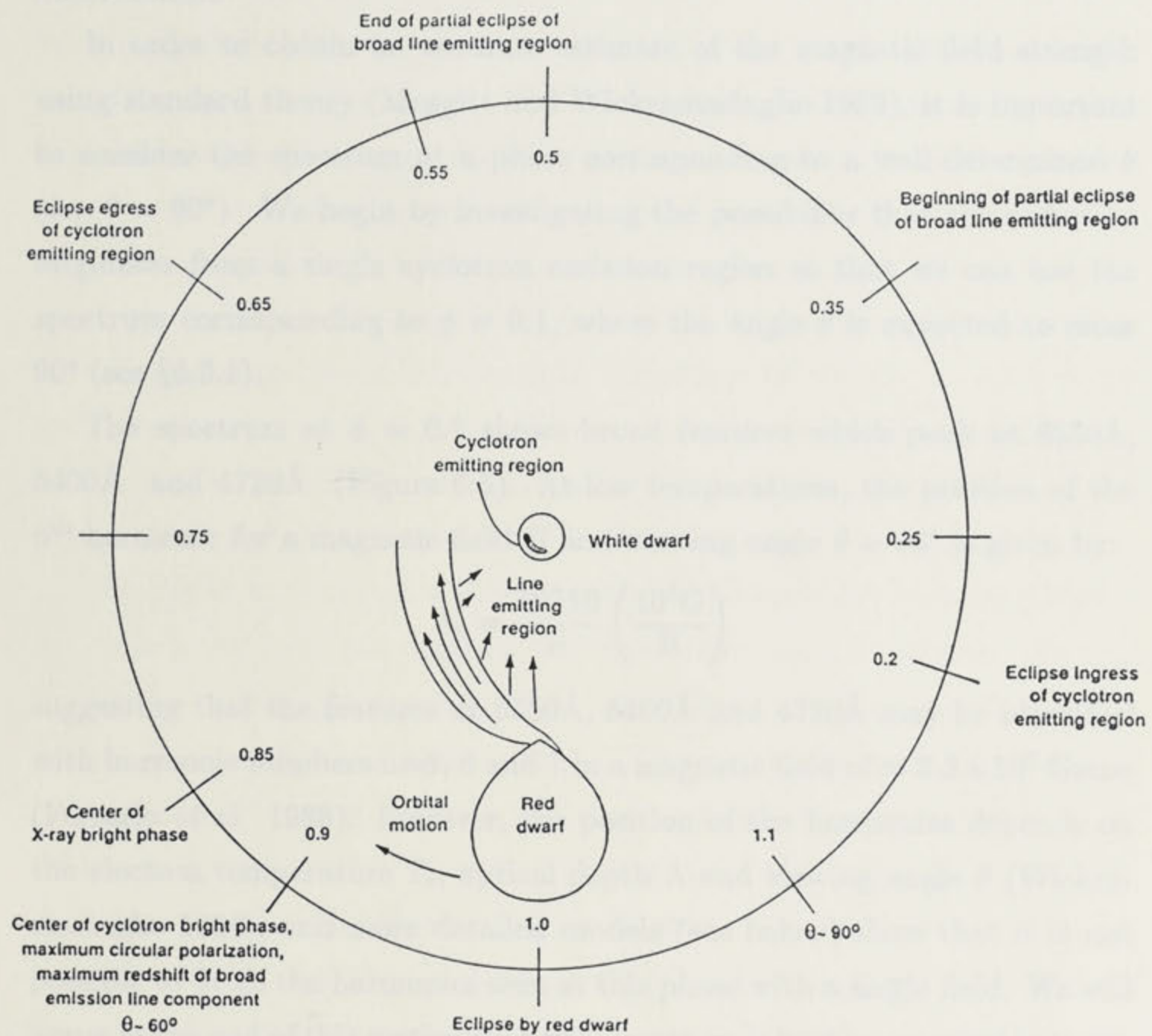


Figure 6.8: Derived Viewing Geometry of EXO 033319-2554.2

cyclotron harmonics in emission arising from an accretion shock at a temperature of ≈ 10 keV and a magnetic field of $\approx 3.2 \times 10^7$ Gauss (Wickramasinghe and Meggitt 1982). A similar interpretation is also possible for the present observations.

In order to obtain an accurate estimate of the magnetic field strength using standard theory (Meggitt and Wickramasinghe 1982), it is important to consider the spectrum at a phase corresponding to a well determined θ (*ie.* $\theta = 90^\circ$). We begin by investigating the possibility that the radiation originates from a single cyclotron emission region so that we can use the spectrum corresponding to $\phi = 0.1$, where the angle θ is expected to cross 90° (see §6.3.1).

The spectrum at $\phi = 0.1$ shows broad features which peak at 6550\AA , 5400\AA and 4720\AA (Figure 6.5). At low temperatures, the position of the n^{th} harmonic for a magnetic field B and viewing angle $\theta = 90^\circ$ is given by:

$$\lambda_n = \frac{10710}{n} \left(\frac{10^8 \text{G}}{B} \right)$$

suggesting that the features at 6550\AA , 5400\AA and 4720\AA may be identified with harmonic numbers $n=5$, 6 and 7 in a magnetic field of $\approx 3.3 \times 10^7$ Gauss (Ferrario *et al.* 1988). However, the position of the harmonics depends on the electron temperature T_e , optical depth Λ and viewing angle θ (Wickramasinghe 1988), and more detailed models (see below) show that it is not possible to fit all the harmonics seen at this phase with a single field. We will argue at the end of this section that this spectrum is best interpreted in terms of *two* emission regions of different field strengths which are simultaneously visible at this phase.

We next consider the possibility of modelling the spectrum at $\phi = 0.9$ by assuming that the angle θ with the field direction is at a minimum at this phase. Since $\phi = 0.9$ corresponds to the centre of the bright phase, it is likely that the spectrum is dominated by radiation from the main emission region, if two emission regions are present. The disadvantage of using this spectrum is that we have no knowledge of the value of θ at the corresponding

phase. It follows from Table 6.2 that for a point source emission region and radial field lines, the value of $\theta_{min}(= i - \delta)$ is very sensitive to the mass ratio. Therefore, θ_{min} ranges from $32^\circ.8$ at $q = 0.25$ to 74° at $q = 0.1$. Significantly larger values of θ_{min} are only possible if $q < 0.1$ or if the field is strongly inclined to the stellar surface. We have constructed two models assuming $\theta_{min} = 60^\circ$ and 75° . The models have been computed following Wickramasinghe and Meggitt (1985) assuming a point source emission region. The best fit spectrum corresponds to a field $B = 5.1 \times 10^7$ Gauss with an electron temperature $T_e = 10$ keV, electron number density $N_e = 1.0 \times 10^{15}$ cm^{-3} , an optical depth parameter $\Lambda = 1.2 \times 10^4$ and $\theta = 60^\circ$. A similar model constructed for $\theta = 75^\circ$ yields $B = 5.6 \times 10^7$ Gauss, $\Lambda = 1.1 \times 10^3$ for $T_e = 20$ keV and $N_e = 1.0 \times 10^{15}$ cm^{-3} . On these models the features at 4200\AA , 5200\AA and 6550\AA are identified with harmonic numbers 5, 4 and 3. The results for $\theta = 75^\circ$ are included in Figure 6.6.

The theory of cyclotron emission predicts a shift towards lower frequencies and a broadening of the emission features as the angle θ increases. Due to the limited wavelength coverage of the AAT data, a complete emission profile is only observed for harmonic number 4. The position of this harmonic does not appear to change by more than 50\AA over the phase interval $\phi = 0.7 - 0.9$. Although our wavelength coverage allows only the blue edge of $n=3$ and the red edge of $n=5$ to be observed, their locations do not appear to shift by more than 100\AA over the phase range $\phi = 0.7 - 0.1$. We believe this to be a real effect despite the uncertainties introduced in locating the emission peaks due to our limited wavelength coverage. There is evidence for a significant shift ($\approx 200 \text{\AA}$) in the position of $n=4$ between the spectra at $\phi = 0.9$ and $\phi = 0.1$ but this could be partly due to the broadening of this feature due to the appearance of a second emission region at $\phi = 0.1$ (see below).

If we assume that the field lines are nearly radial, θ will vary between $\approx 90^\circ$ (at $\phi = 0.7$ and $\phi = 0.1$) and θ_{min} (at $\phi = 0.9$). Our calculations predict shifts of about 280 , 550 and 680\AA for $n=5$, 4 , and 3 between $\theta = 60^\circ$ and $\theta = 90^\circ$ when $B = 5.1 \times 10^7$ Gauss (Figure 6.9). In particular, we

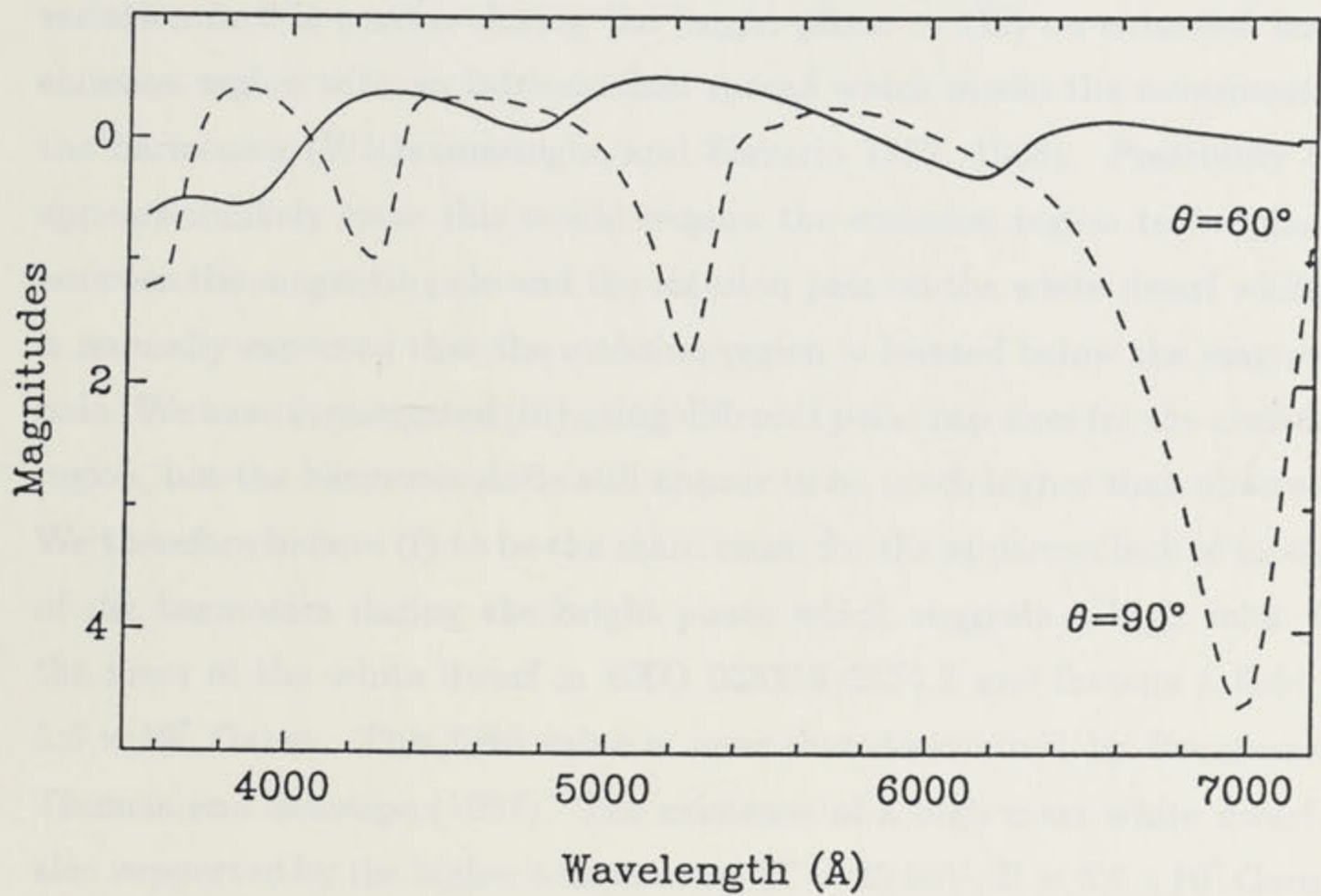


Figure 6.9: Predicted Cyclotron Harmonic Shift
 Cyclotron spectra computed for a magnetic field $B = 5.1 \times 10^7$ Gauss at viewing angles of $\theta = 60^\circ$ and $\theta = 90^\circ$. Note the large wavelength shift of the harmonics which is expected over this range of viewing angles.

would expect to see the blue edge of $n=3$ shift beyond 6800\AA (the long wavelength cut-off of our AAT observations) at the beginning and at the end of the bright phase, contrary to our observations. The lack of evidence for significant movement of all the harmonics between $\phi = 0.7$ and $\phi = 0.9$ must indicate either (i) a value of $\theta_{min} \geq 75^\circ$ due to a low mass ratio, (ii) a field direction that is non-radial and inclined towards the rotation axis so that the variation in θ is smaller during the bright phase or (iii) an extended main emission region with an intrinsic field spread which masks the movement of the harmonics (Wickramasinghe and Ferrario 1987, 1988). Possibility (ii) appears unlikely since this would require the emission region to be placed between the magnetic pole and the rotation pole on the white dwarf while it is normally expected that the emission region is located below the magnetic pole. We have investigated (iii) using different polar cap sizes for the emission region, but the harmonic shifts still appear to be much higher than observed. We therefore believe (i) to be the main cause for the apparent lack of motion of the harmonics during the bright phase which suggests a high value for the mass of the white dwarf in EXO 033319-2554.2 and favours a field of 5.6×10^7 Gauss. This field value is near that determined by Beuermann, Thomas and Schwöpe (1987). The existence of a high mass white dwarf is also supported by the higher temperature ($T = 20$ keV, $B = 5.6 \times 10^7$ Gauss) previously deduced for the cyclotron emission region in comparison with the value inferred for VV Puppis ($T = 10$ keV, $B = 3.2 \times 10^7$). We note in this connection that the shock temperature $T_s \propto M_{wd}^{4/3}$. Finally, we point out that Hameury, King and Lasota (1988) have independently concluded that EXO 033319-2554.2 contains a white dwarf of unusually high mass.

Let us now return to the spectrum at $\phi = 0.1$ (Figure 6.5). This spectrum differs from the other bright phase spectra in exhibiting a further emission peak at 4720\AA . A closer examination of the AAT data shows in addition, the presence of a broad depression centred near 5650\AA in both the blue and the red sets of data which were obtained on consecutive cycles. We have attempted to model the spectrum at $\phi = 0.1$ by assuming that all the broad

features are caused by the presence of cyclotron harmonics. We find that it is impossible to model the main peaks at 4720Å, 5400Å, and 6550Å without invoking the presence of a second region with a significantly different field strength. The results are included in Figure 6.5. The second emission region has $T_e = 10$ keV, $N_e = 1.5 \times 10^{16}$ cm⁻³, $B = 2.8 \times 10^7$ Gauss, $\Lambda = 3.2 \times 10^5$ and is assumed to be viewed at $\theta = 90^\circ$. The lower temperature of this emission region may not be inconsistent with the high mass white dwarf, since at lower field strengths the cyclotron lines could only be produced in the cooler outer regions of a shock with density and temperature structure. The peaks at 4720Å and 5400Å correspond to harmonic numbers 8 and 7 while the dip at 5650Å occurs at the blue edge of harmonic number 6 which is optically thick and almost completely undetectable. The peak at 6650Å is attributed to the main emission region which is assumed to be also visible at $\phi = 0.1$. We note that there is some evidence that the feature at 4720Å is also seen in the AAT data at $\phi = 0.3$ (Figure 6.4), indicating that the second cyclotron emission region may still be making some contribution to the total light at this phase.

We believe that the radiation originates from two distinct emission regions rather than from a single and very extended one. In the latter case, the required extension of the region would be so high (almost from magnetic equator to the pole for a centred dipole field distribution) that a very high spread in magnetic field would be expected and the cyclotron harmonics would be washed out (Wickramasinghe and Ferrario 1987, 1988).

It has recently been argued by Ferrario, Wickramasinghe and Tuohy (1988) that, except for a special orientation of the magnetic axis, the emission regions on the white dwarf surface are likely to occur near the foot points of closed field lines (see also Wickramasinghe 1988). The field strengths deduced for the emission regions in EXO 033319-2554.2 are in the ratio 2:1 and cannot correspond to the field strengths at the foot points of closed field lines if the field distribution is that of a centred dipole. However, the observed ratio is expected for the ratio of field strengths at the foot points of

closed field lines which connect the polar and equatorial regions in a centred *quadrupole* field distribution. Such a field distribution has recently been proposed by Meggitt and Wickramasinghe (1988) for the AM Herculis variable 2A0311 – 227. We note that cyclotron emission regions which are separated by much less than 180° on the white dwarf surface have been suggested to explain the polarization and intensity behaviour of the AM Herculis system H0139 – 68 (Piirola, Reiz and Coyne 1987; Cropper 1987; Bailey 1988b), and the AM Herculis candidate Grus V1 (Tuohy *et al.* 1988).

Our conclusion that there are two distinct cyclotron emission regions in EXO 033319–2554.2 is based mainly on spectroscopic data and in particular, on the additional strong feature at 4720\AA seen in the spectrum at $\phi = 0.1$. Although we have been able to develop a consistent model, the possibility remains that the new feature may have a different (non-cyclotron) origin.

We believe that an interpretation of the spectrum at $\phi = 0.1$ in terms of distortion of the continuum due to photospheric Zeeman absorption is unlikely, since the feature at $\approx 4720\text{\AA}$ is clearly absent in most of the faint phase spectra. It is, however, possible that the feature may arise from an accretion halo when the main cyclotron emission region is viewed near $\theta = 90^\circ$ as in E1405 – 451 (Wickramasinghe, Tuohy and Visvanathan 1987), in CW1103+254 (Schmidt, Stockman and Grandi 1983), and in 2A0311 – 227 (Schmidt, Stockman and Grandi 1986). The Zeeman calculations for hydrogen (Kemic 1974; Henry and O'Connell 1984, 1985; Wunner *et al.* 1985) show that there are no $H\alpha$ or $H\beta$ transitions that will produce a broad absorption feature centred at $\approx 5000\text{\AA}$ for field strengths of $\leq 10^8$ Gauss. A possibility is that there may be an absorption feature near $\approx 4600\text{\AA}$ which distorts the position of the blue harmonic in our data. Although there are several $H\beta$ Zeeman transitions (*eg.* $H\beta$ $2p + 1 - 4s0$) which may absorb near this wavelength for $B \approx 5 \times 10^7$ Gauss, we would also expect to see even stronger associated features due to $H\alpha$ in the wavelength region $5000 - 6500\text{\AA}$ (*eg.* $H\alpha$ $2p0 - 3d0$, near 6400\AA). Furthermore, we note that the other systems with halo features only show evidence of the strongest of the $H\alpha$ transitions

and not of the other Balmer lines. There is some evidence for narrow features near 6400\AA which, if taken on their own, may be identified with $H\alpha$ absorption from the halo. However, due to their intrinsic weakness relative to the 4600\AA feature, it is not possible to identify both sets of features with absorption due to Balmer transitions from the accretion halo. We conclude that a Zeeman absorption interpretation is unlikely as an explanation for the feature at 4600\AA and that the broad modulation seen in the spectrum at $\phi = 0.1$ is in fact of cyclotron origin as previously assumed by us. However, further observations are required to establish if the narrow features seen at $\phi = 0.1$ are real and if they originate from an accretion halo.

6.5 Conclusions

We have presented circular polarization and spectroscopic observations of the X-ray source EXO 033319-2554.2 which show it to be an exciting new member of the AM Herculis class. It is the third system to show eclipses due to the M dwarf and the second to show cyclotron harmonic emission features in its optical spectrum.

The circular polarization data indicate that EXO 033319-2554.2 is similar to VV Puppis, with the maximum polarization occurring in the blue, in contrast to what is usually observed in AM Herculis binaries.

We have argued that the spectrum of EXO 033319-2554.2 can be interpreted in terms of cyclotron emission from a main region of field strength 5.6×10^7 Gauss and a second region of field strength 2.8×10^7 Gauss.

The absence of large shifts in the positions of harmonics with phase has allowed us to place strong limits on the possible values for the mass ratio. We estimate $q \approx 0.1$ which implies the presence of a high mass white dwarf in EXO 033319-2554.2.

We are grateful to Paolo Giommi and Julian Osborne for communicating

EXOSAT results in advance of publication and to Mike Bessell for assistance with the data analysis. We thank the AAO staff for their excellent technical support. One of us (L.F.) acknowledges support from an Australian National University Postgraduate Research Scholarship.

6.6 Circular Polarisation Modelling

We have constructed theoretical polarisation curves by adding the contributions from two point source cyclotron emission regions contributing polarisation of opposite sign and characterised by the same parameters used to interpret the cyclotron spectra. Our best fit is shown in Figure 6.10. The emission regions are 90° apart on the white dwarf surface at colatitudes of 15° (5.6×10^7 G region) and 105° (2.8×10^7 G region). The orbital inclination is 88° . The location of the higher field cyclotron emission region and the orbital inclination are chosen to be consistent with the values determined in §6.4.5. We assume that the contribution to the circularly polarised light from the lower field region is half of the contribution from the higher field region and that the unpolarised background is about four times less important for the bluest of the presented bands. The latter assumption may be justified by noting that the red star is only likely to make an important contribution to the total light for $\lambda \geq 7000 \text{ \AA}$.

In our model the main emission region ($B = 5.6 \times 10^7$ G) is visible from $\phi = 0.65$ to $\phi = 0.1$ and the secondary emission region from $\phi = 0.65$ to $\phi = 0.25$, and they are viewed most directly at $\phi = 0.85$ and $\phi = 0.95$ respectively. We point out that the lengths of the bright phases corresponding to the two regions are in complete agreement with our spectroscopic observations. Namely, the main emission region is eclipsed by the body of the white dwarf at $\phi = 0.1$ which coincides with the phase of last detection of cyclotron harmonics originating from the 5.6×10^7 G region. The eclipse of the secondary region is also in excellent agreement with the spectroscopic data, which show the presence of cyclotron harmonics from the 2.8×10^7 G region until $\phi = 0.3$. Berriman and Smith (1988) also suggest the presence of two cyclotron emission regions by comparing the circular polarisation data that they obtained on two consecutive nights. In one night they detected a reversal in the sign of the circular polarisation data, similar to that detected

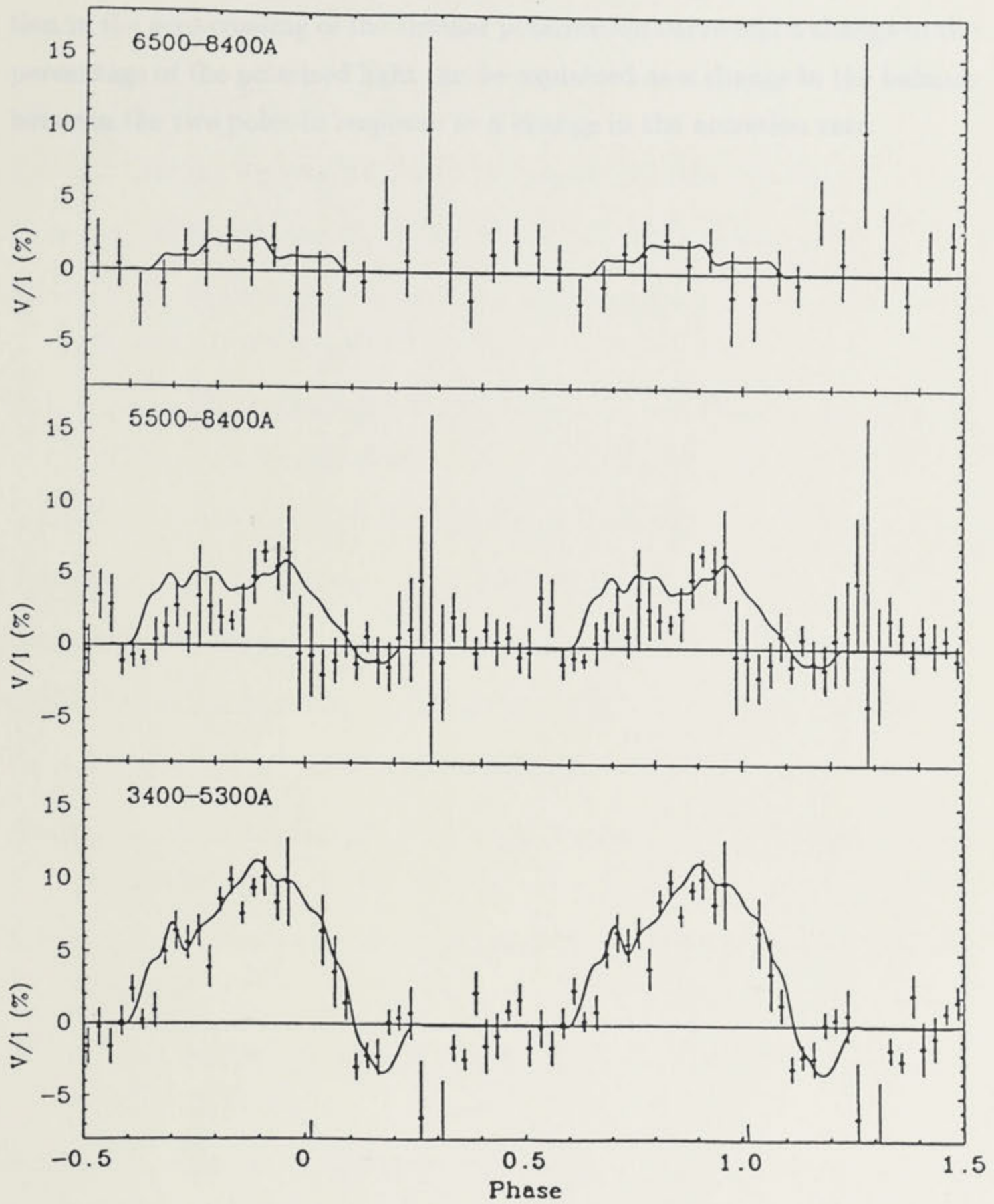


Figure 6.10: Circular Polarization Modelling
 Circular polarisation data for EXO 033319 - 2554.2 and theoretical polarisation curves obtained by adding the contributions of two cyclotron emission regions (see text).

by us, but this reversal was not present in the next night. A temporal variation in the zero crossing of the circular polarisation curve and a change in the percentage of the polarised light can be explained as a change in the balance between the two poles in response to a change in the accretion rate.

Dalrymple, J. 1978a, *Victoria Workshop, Chromospheric Polarisation*.

Dalrymple, J. 1978b, *Victoria Workshop, Chromospheric Polarisation*.

Dalrymple, J. A., Ferraro, L., Tully, J. R., Wickramasinghe, D. T., and Bagnall, J. B. 1987, *MNRAS*, **167**.

Dalrymple, J. A., Wickramasinghe, D. T., Bagnall, J., and Cropper, M. 1988, *M. N. R. A. S.*, to be submitted.

Davies, G., and Smith, P. S. 1965, *Ap. J. (Suppl)*, **32**, 187.

Downing, K., and Thomas, R. C. 1987, *MNRAS*, **167**.

Downing, K., Thomas, R. C., and Bagnall, J. 1989, *MNRAS*, **197**.

Edwards, G. A., Matthews, J., and Nelson, J. E. 1978, *Ap. J.*, **219**, 877.

Cropper, M. 1987, *M. N. R. A. S.*, **216**, 399.

Ferraro, L., Wickramasinghe, D. T., and Tully, J. R. 1987, *Proc. Astron. Soc. Australia*, to appear.

Ferraro, L., Wickramasinghe, D. T., and Tully, J. R. 1988, *Ap. J.*, to appear.

Ferraro, L., Wickramasinghe, D. T., Tully, J. R., and Dalrymple, J. A. 1986, *MNRAS*, **161**.

Giannini, P., Angilli, I., Di Criscuolo, J. P., Stella, L., and Tringali, G. 1987, *MNRAS*, **167**.

Hannigan, J. M., King, A. J., and Linnell, J. P. 1986, *Astr. Ap.*, to appear.

Henry, R. J. W. and O'Donoghue, R. P. 1984, *Ap. J. (Suppl)*, **28**, 187.

Henry, R. J. W. and O'Donoghue, R. P. 1986, *Pub. Astr. Soc. Aust.*, **3**.

6.7 References

- Bailey, J. 1981, *M. N. R. A. S.*, **197**, 31.
- Bailey, J. 1988a, Vatican Workshop, *Circumstellar Polarization*.
- Bailey, J. 1988b, Vatican Workshop, *Circumstellar Polarization*.
- Bailey, J. A., Ferrario, L., Tuohy, I. R., Wickramasinghe, D. T., and Hough, J. H. 1987, *IAU Circ*, # 4517.
- Bailey, J. A., Wickramasinghe, D. T., Hough, J., and Cropper, M. 1988, *M. N. R. A. S.*, to be submitted.
- Berriman, G., and Smith, P. S. 1988, *Ap. J. (Letters)*, **329**, L97.
- Beuermann, K., and Thomas, H. C. 1987, *IAU Circ*, # 4486.
- Beuermann, K., Thomas, H. C., and Schwope, A. 1987, *IAU Circ*, # 4517.
- Chanan, G.A., Middleditch, J. and Nelson, J.E. 1976, *Ap. J.*, **208**, 512.
- Cropper, M. 1987, *M. N. R. A. S.*, **228**, 389.
- Ferrario, L., Wickramasinghe, D. T., and Tuohy, I. R. 1987, *Proc. Astron. Soc. of Australia*, in press.
- Ferrario, L., Wickramasinghe, D. T., and Tuohy, I. R. 1988, *Ap. J.*, to be submitted.
- Ferrario, L., Wickramasinghe, D. T., Tuohy, I. R., and Bailey, J. A. 1988, *IAU Circ*, # 4523.
- Giommi, P., Angelini, L., Osborne, J. P., Stella, L., and Tagliaferri, G. 1987, *IAU Circ*, # 4486.
- Hameury, J. M., King, A. R., and Lasota, J. P. 1988, *Astr. Ap.*, submitted.
- Henry, R. J. W. and O'Connell, R. F. 1984 *Ap. J. (Letters)*, **282**, L97.
- Henry, R. J. W. and O'Connell, R. F. 1985, *Pub. A. S. P.*, **97**, 333.

- Kemic, S. B. 1974, *Joint Institute of Laboratory Astrophysics*, Report 113.
- Liebert, J., and Stockman, H. S. 1985, in *Cataclysmic Variables and Low-Mass X-ray Binaries*, ed. D. Q. Lamb and J. Patterson (Dordrecht: Reidel), p. 151.
- Meggitt, S. M. A., and Wickramasinghe, D.T. 1982, *M. N. R. A. S.*, **198**, 71.
- Meggitt, S. M. A., and Wickramasinghe, D.T. 1988, *M. N. R. A. S.*, submitted.
- Osborne, J. P., Giommi, P., Angelini, L., Tagliaferri, G., and Stella, L. 1988, *Ap. J. (Letters)*, in press.
- Pirola, V., Reiz, A., and Coyne, G. V. 1987, *Astr. Ap.*, **185**, 189.
- Rodgers, A. W., Conroy, P., and Bloxham, G. 1987, *Pub. A. S. P.*, submitted.
- Rosen, S. R., Mason, K. O., and Córdova, F. A. 1986, *M. N. R. A. S.*, **224**, 987.
- Ritter, H. 1984, *Astr. Ap. Suppl.*, **57**, 385.
- Schmidt, G. D., Stockmann, H. S., and Grandi, S. A. 1983, *Ap. J.*, **271**, 735.
- Schmidt, G. D., Stockmann, H. S., and Grandi, S. A. 1986, *Ap. J.*, **300**, 804.
- Taylor, B. J. 1984, *Ap. J. Suppl.*, **54**, 259.
- Tuohy, I. R., Ferrario, L., Wickramasinghe, D. T., and Hawkins, M. R. S. 1988, *Ap. J. (Letters)*, in press.
- Visvanathan, N., and Wickramasinghe, D. T. 1979, *Nature*, **281**, 47.
- Wickramasinghe, D. T. 1988, Vatican Workshop, *Circumstellar Polarization*.
- Wickramasinghe, D. T., and Ferrario, L. 1987, *Proc. Astron. Soc. of Australia*, in press.
- Wickramasinghe, D. T., and Ferrario, L. 1988, *Ap. J.*, in press.

Wickramasinghe, D. T., and Meggitt, S. M. A. 1982, *M. N. R. A. S.*, **198**, 975.

Wickramasinghe, D. T., and Meggitt, S. M. A. 1985, *M. N. R. A. S.*, **216**, 857.

Wickramasinghe, D. T., Tuohy, I. R., and Visvanathan, N. 1987, *Ap. J.*, **318**, 326.

Wunner, G., Rosner, W., Herold, H., and Ruder, H. 1985 *Astr. Ap.*, **149**, 102.

2.1 Abstract

We present U, V, R, I and long-term color photometry of the faint and highly variable detached variable star HD 161411. The star is a member of the δ Scuti class of pulsating stars. Observations of the V and I bands using the $AAVSO$ 12-inch telescope and the $AAVSO$ 12-inch telescope at the University of Toronto and reported variations of a binary period of 1.014 days. Diurnal colour differences are evident in the U, V, R, I light curves of the V band, a single maximum peak is present, while in the U, R, I bands, a second red peak is dominant at a phase separated of 180°. The observations are consistent with a pulsating variable star and suggest an origin in an $AAVSO$ δ Scuti binary system. The binary period and the long-term color photometry of the star also support this conclusion. We conclude therefore that the object (designated $AAVSO$ 161411) is almost certainly a new $AAVSO$ δ Scuti variable, and develops a model in which the blue and red outbursts originate from two different (but possibly by analogy) systems regions that are characterized by different physical temperatures and spectral distributions are used regarding the binary star.

Chapter 7

Evidence for Nonpolar Emission Regions in a New AM Herculis Candidate

7.1 Abstract

We present *UBVRI* and long-term plate photometry of the faint and highly erratic cataclysmic variable discovered by Hawkins from a sequence of UK Schmidt measurements. Observations of the $V \approx 18$ star using the ANU 2.3 metre telescope over two consecutive nights in September 1986 show pronounced and repeatable modulation at a binary period of 108.6 minutes. Dramatic colour differences are evident in the folded *UBVRI* light curves: in the *U* band, a single sinusoidal peak is present, while at longer wavelengths, a second red peak is dominant at a phase separation of $\Delta\phi \approx 0.5$. This behaviour is strongly suggestive of cyclotron emission from two magnetic accretion funnels in an AM Herculis binary system. The binary period and the long timescale two-state activity of the source also support this classification. We conclude therefore that the object (designated Grus V1) is almost certainly a new AM Herculis variable, and develop a model in which the blue and red components originate from two *nondiometric* (and probably *nonpolar*) cyclotron regions that are characterized by differing electron temperatures and opacities. Predictions are made regarding the linear and

circular polarization properties of the system.

Subject headings: stars: binaries – stars: individual (Grus V1) – stars: magnetic – stars: white dwarfs

(1991, 1993) studied three unusual cataclysmic variables from a 20.4 year sequence of UK Schmidt plates taken from a field centred on the constellation Crux. One of these objects, referred to as V1, was found to exhibit particularly intense He II λ 685 emission and a high degree of variability. This variability was confined to two distinct states corresponding to $B - V$ and $B - R$, each of which appeared to persist for a timescale of years. These properties suggested that V1 might belong to the new AM Her class comprising a highly magnetic ($B > 20$ MG) white dwarf accreting material from a late-type secondary (e.g. Leight and Pickering 1992). Unfortunately, this possibility could not be pursued further because the object was found to be too faint and located essentially unobservably. In 1993 however, V1 re-emerged in the bright state and provided an opportunity for detailed follow-up study.

In this letter we report preliminary multi-colour photometry of V1, which we name the temporary designation Crux V1. The orbital period that we have found and the distinctive nature of the UVES light curves leave little doubt that Crux V1 is in fact a new AM Her variable. The coordinates for the object are $\alpha = 07^{\text{h}} 31^{\text{m}} 43.7^{\text{s}}$, $\delta = -47^{\circ} 52' 40''$ (1993), and a finding chart (with North at the bottom and East to the right) is presented by Dawson (1993).

7.3 Observations and Results

7.3.1 UK Schmidt Plate Photometry

Crux V1 lies in a field which is being regularly monitored as a programme of red long term variables, and a large number of UK Schmidt plates have been

7.2 Introduction

As part of a survey aimed at detecting faint and variable objects, Hawkins (1981, 1983) isolated three unusual cataclysmic variables from a ≈ 6 year sequence of UK Schmidt plates taken for a field centred in the constellation Grus. One of these objects, referred to as V1, was found to exhibit particularly intense He II λ 4686 emission and a high degree of variability. This variability was confined to two distinct states corresponding to $B \approx 18$ and $B \approx 21$, each of which appeared to persist for a timescale of years. These properties suggested that V1 might belong to the rare AM Herculis class comprising a highly magnetic ($B \approx 20$ MG) white dwarf accreting material from a late-type secondary (*e.g.*, Liebert and Stockman 1985). Unfortunately this possibility could not be pursued further because the object reentered the faint state and became essentially unobservable. In 1986 however, V1 returned to the bright state and presented an opportunity for detailed follow-up study.

In this *Letter* we report multicolour and plate photometry of V1, to which we assign the temporary designation Grus V1. The orbital period that we have found and the distinctive nature of the *UBVRI* light curves leave little doubt that Grus V1 is in fact a new AM Her variable. The coordinates for the object are $\alpha = 21^{\text{h}} 34^{\text{m}} 45.2^{\text{s}}$, $\delta = -43^{\circ} 55' 46''$ (1950), and a finding chart (with North at the bottom and East to the right) is presented by Hawkins (1981).

7.3 Observations and Results

7.3.1 UK Schmidt Plate Photometry

Grus V1 lies in a field which is being regularly monitored to measure medium and long term variables, and a large number of UK Schmidt plates have been

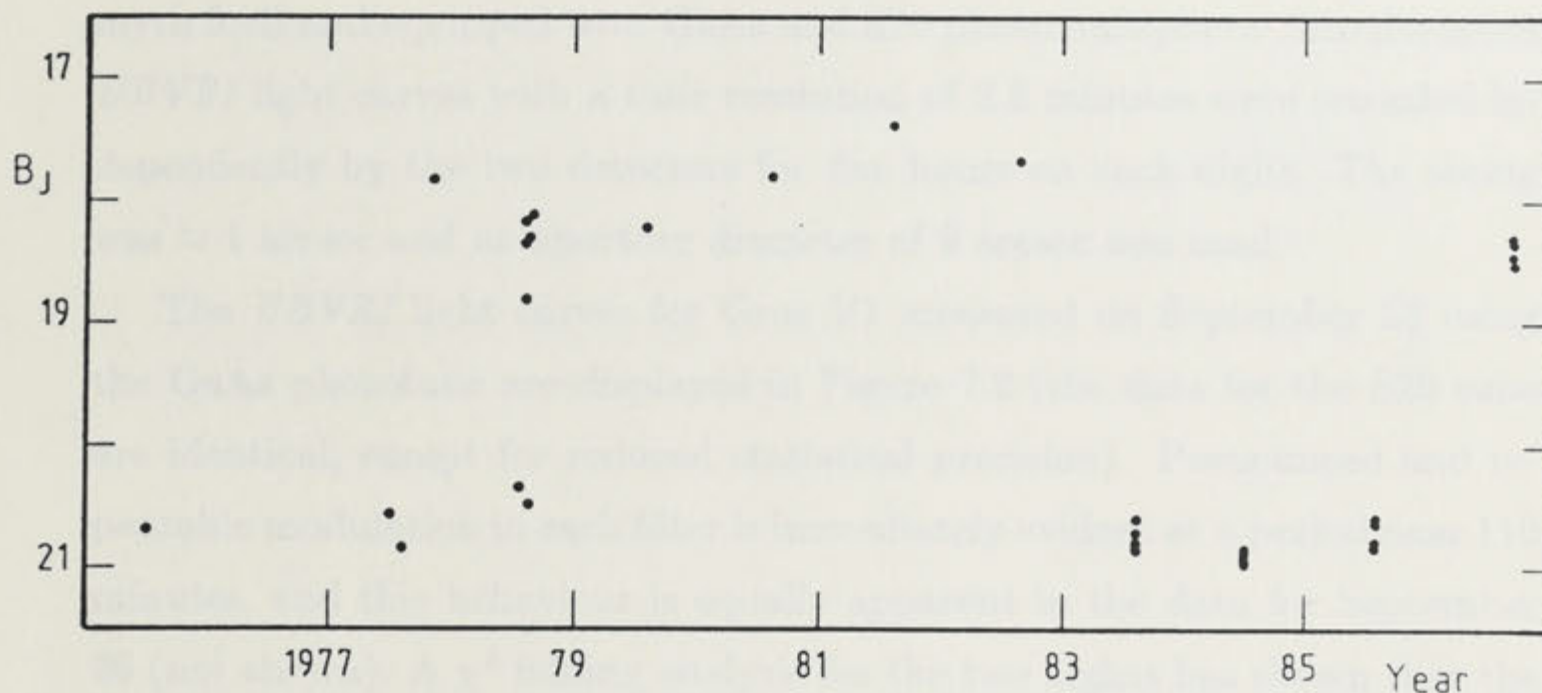


Figure 7.1: Long Term Monitoring of Grus V1

Long term monitoring of Grus V1 between 1975-1986. The B_J magnitudes have been measured from UK Schmidt plates and have errors of 0.1 mag.

accumulated over a period of 11 years. Figure 7.1 shows the light curve of Grus V1 sampled between 1975 and 1986. The variability is dominated by high and low states around $B_J = 18$ and $B_J = 21$, and as noted from an earlier subset of the data (Hawkins 1983), the two states seem to last for several years. During the period 1977-1978 however, the object underwent violent fluctuations in luminosity of up to 3 magnitudes in a few days before settling down to an apparently uninterrupted high state. The low state from 1983-1985 was followed by a new maximum, during which the *UBVRI* observations discussed below were made. Recently (August 1987), the object appears to have reentered a phase of violent fluctuations, but detailed plate photometry is not yet available.

7.3.2 *UBVRI* Photometry

UBVRI photometry of Grus V1 was obtained on 1986 September 25 and 26 using the ANU 2.3 metre telescope at Siding Spring Observatory. The Two Channel Chopper (see Tuohy *et al.* 1986) was mounted to one of the nas-

myth focii and equipped with GaAs and S20 photomultipliers. Simultaneous *UBVRI* light curves with a time resolution of 2.8 minutes were recorded independently by the two detectors for five hours on each night. The seeing was ≈ 1 arcsec and an aperture diameter of 9 arcsec was used.

The *UBVRI* light curves for Grus V1 measured on September 25 using the GaAs phototube are displayed in Figure 7.2 (the data for the S20 tube are identical, except for reduced statistical precision). Pronounced and repeatable modulation in each filter is immediately evident at a period near 110 minutes, and this behaviour is equally apparent in the data for September 26 (not shown). A χ^2 folding analysis for the two nights has shown that the five light curves are all consistent with an unambiguously determined period of 108.6 ± 0.4 minutes. Defining phase zero to be the centre of the maximum in the *U*-band light curve, we derive the following heliocentric ephemeris for Grus V1:

$$\text{HJD } 2,446,698.9765(47) + 0.07537(35) \text{ E.}$$

We remark that no other periodicities in the range 10 – 200 minutes were revealed by our folding analysis, or by Fourier analysis.

In Figure 7.3 we show the average *UBVRI* light curves for Grus V1 produced by folding the approximately six cycles at a period of 108.6 minutes. Substantial differences in the five filters are evident. In the *U*-band, the modulation is closely sinusoidal with a single peak at $\phi = 0.0$ (by definition), while in the *B*-band, a second peak appears at a phase separation of $\Delta\phi = 0.51 \pm 0.04$ and progressively becomes more dominant towards *R* and *I*. This second red peak is much narrower than the blue peak; the FWHM of the blue peak measured relative to the minimum in the *U*-band modulation is $\Delta\phi \approx 0.44$, compared with a FWHM of $\Delta\phi \approx 0.17$ for the red peak measured in the *R*-band (the red peak is only present during the brief phase interval $\phi \approx 0.4 - 0.6$). We also note that there is clear evidence for a progressive phase shift by $\Delta\phi \approx 0.1$ in the centroid of the blue peak between the *U* and *I* bands (in the sense that the peak in the *I*-band occurs at a later phase).

The mean *B* magnitude and colours for Grus V1 averaged over the 108.6

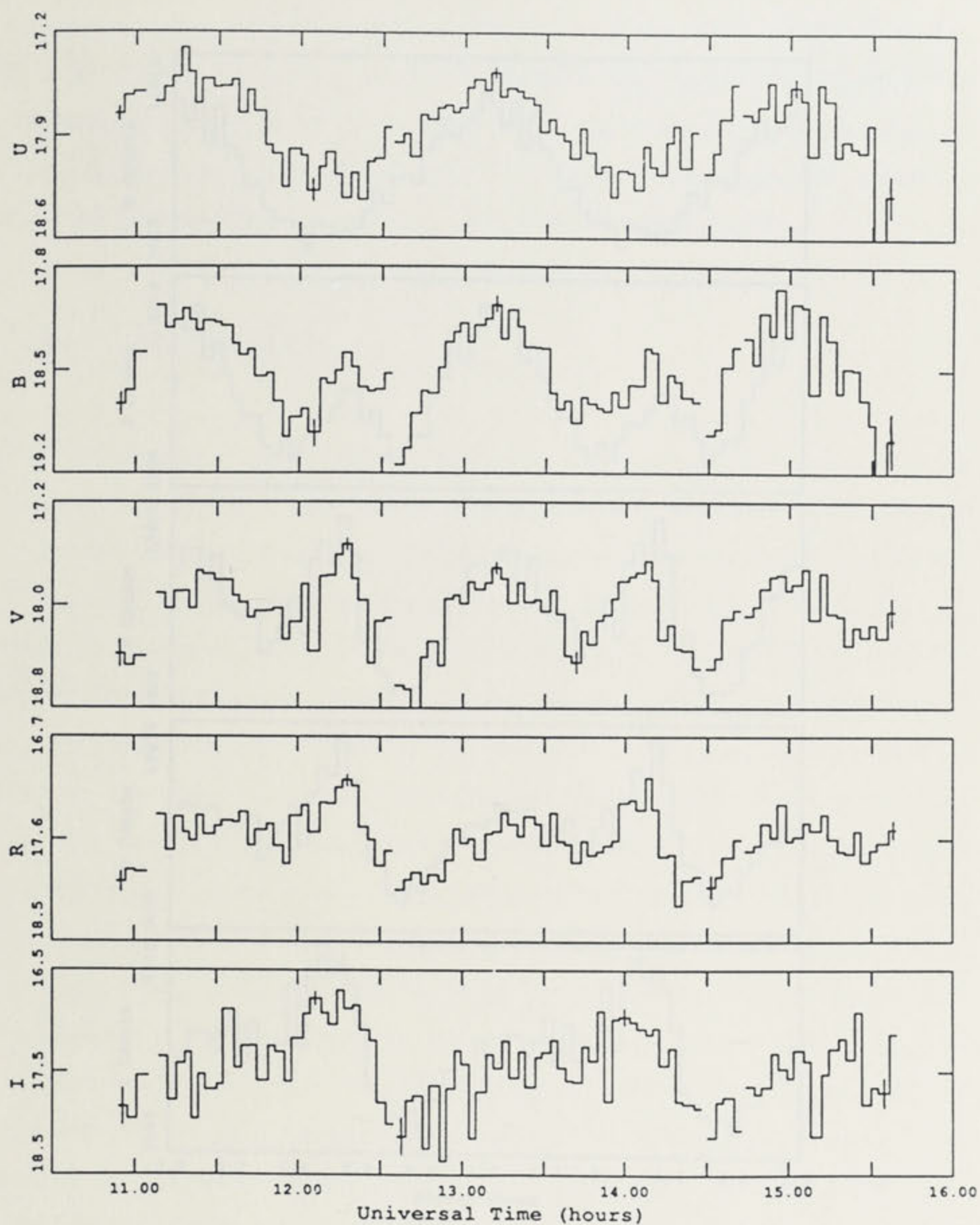


Figure 7.2: Calibrated *UBVRI* Light Curves
 Calibrated *UBVRI* light curves measured for Grus V1 on 1986 September 25 using the ANU 2.3 metre telescope and a GaAs photomultiplier. Representative $\pm 1\sigma$ Poisson error bars are plotted.

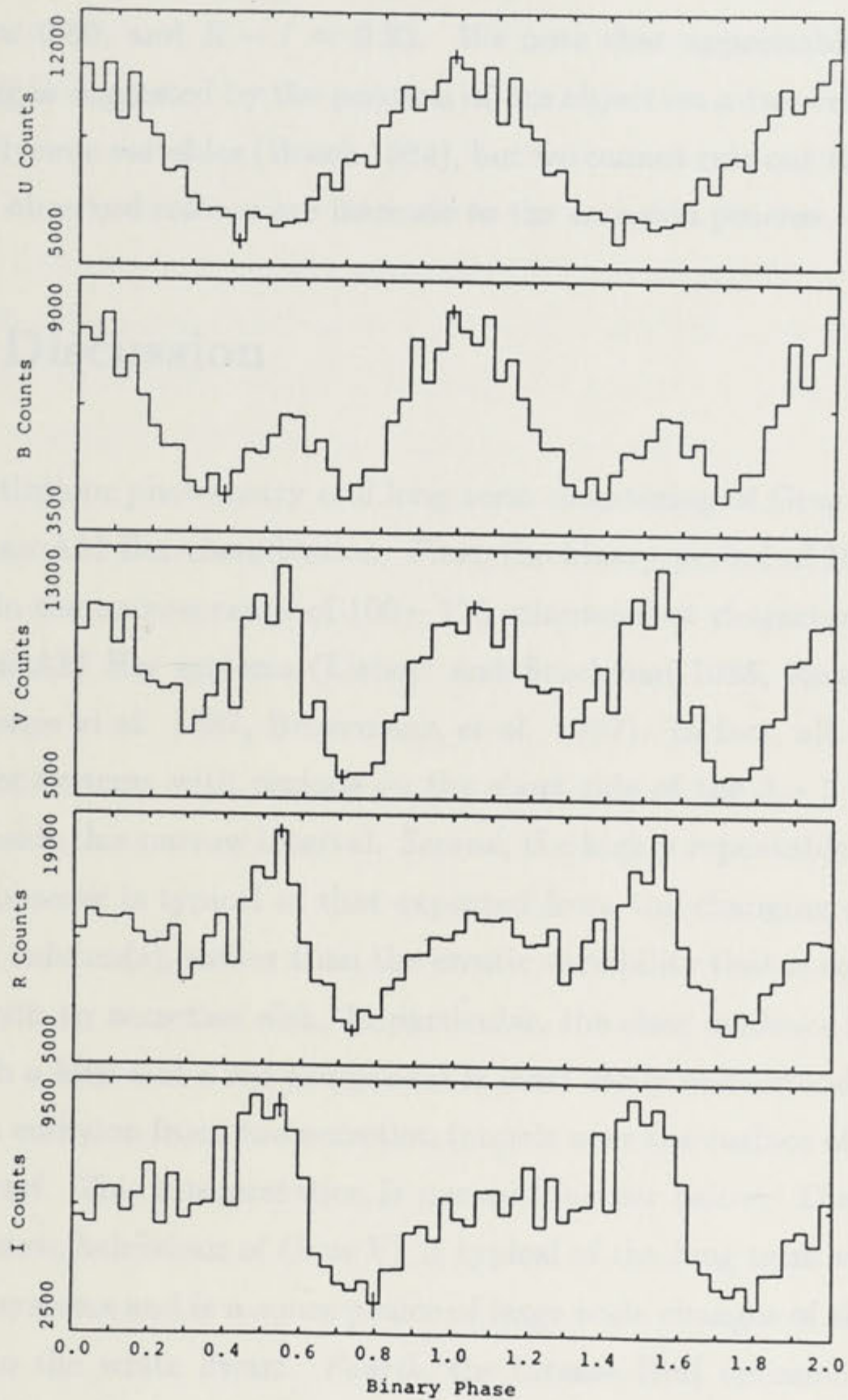


Figure 7.3: Average *UBVRI* Light Curves
 Average *UBVRI* light curves for Grus V1 produced by folding the data from September 25 and 26 at a period of 108.6 minutes. Two cycles of sky-subtracted counts are shown, together with representative $\pm\sigma$ Poisson error bars.

minute period are as follows: $B \approx 18.5$, $U - B \approx -0.64$, $B - V \approx 0.53$, $V - R \approx 0.50$, and $R - I \approx 0.32$. We note that appreciable interstellar reddening is suggested by the position of the object on a two-colour diagram for cataclysmic variables (Bruch 1984), but we cannot rule out the possibility that the observed colours are intrinsic to the emission process.

7.4 Discussion

Our multicolour photometry and long term monitoring of Grus V1 strongly indicate an AM Her classification. *First*, the binary period of 108.6 minutes lies within the narrow range of 100 – 115 minutes that characterizes 8 of the 13 known AM Her systems (Liebert and Stockman 1985, Remillard *et al.* 1986, Morris *et al.* 1987, Beuermann *et al.* 1987). In fact, all but 2 of the 9 AM Her systems with periods on the short side of the 2 – 3 hour period gap lie inside this narrow interval. *Second*, the highly repeatable modulation that we observe is typical of that expected from the changing aspect of an accretion column(s), rather than the erratic variability that is common for a system with an accretion disk. In particular, the clear evidence for emission from both a blue and a red component is most easily understood in terms of cyclotron emission from *two* accretion funnels near the surface of a magnetic white dwarf. This interpretation is pursued further below. *Third*, the high and low state behaviour of Grus V1 is typical of the long term variability of AM Her systems and is a consequence of large scale changes of the accretion rate on to the white dwarf. *Fourth*, the intense HeII emission relative to $H\beta$ (Hawkins 1983) is a common property of magnetic variables (*e.g.* Watts 1985).

We conclude therefore from the cumulative evidence that Grus V1 is almost certainly a new AM Her variable, but emphasize that polarimetry is necessary to confirm that the emission is predominantly cyclotron in origin, and that other variable sources of radiation are not significant (*e.g.* the

heated secondary). We remark that while soft X-ray emission is a well-known characteristic of AM Her variables, the absence of the source in the HEAO-A2 soft X-ray catalog (Nugent et al. 1983) is to be expected in view of the optical faintness of the system, even in the high state. For example, using our average V magnitude and a mean value of $F_x/F_{opt} \approx 32$ (derived from nine other AM Her variables in the units of Morris *et al.* 1987), combined with the IPC flux conversion ratio given in Vaiana *et al.* (1981), we obtain a rough prediction for the 0.2 – 4 keV flux of $F_x \approx 3 \times 10^{-12}$ ergs cm $^{-2}$ s $^{-1}$ (about an order of magnitude below the limit of the HEAO A-2 soft X-ray survey). Both the faintness of the source and the apparently reddened colours suggest that Grus V1 lies at a distance of at least a few hundred parsecs.

We turn now to an interpretation of the light curve behaviour of Grus V1 in terms of an AM Her model in which the observed radiation arises from *two* distinct (blue and red) regions on the surface of the white dwarf. The *blue* emission region has the well known characteristics of a cyclotron funnel that is viewed over a large range of angles θ to the magnetic field (cf. E1405–451; Bailey *et al.* 1983, Tuohy, Visvanathan, and Wickramasinghe 1985, Cropper, Menzies, and Tapia 1986). We identify the light minimum at $\phi = 0.5$ in the U -band as corresponding to the phase when the blue emission region is viewed at $\theta = \theta_{min}$, consistent with the reduced intensity of high harmonic cyclotron radiation at low angles to the field due to beaming. The phase delay with increasing wavelength noted earlier for the blue emission peak is most probably due to longitudinal density and temperature structure in an extended cyclotron region (*e.g.* Beuermann, Stella, and Patterson 1987, Wickramasinghe and Ferrario 1988). In any event, the blue region remains in the visible hemisphere of the white dwarf throughout the binary cycle ($\phi = 0.0 - 1.0$). The *red* region on the other hand is visible only between $\phi = 0.4 - 0.6$, and thus behaves as an eclipsing region which appears from behind the limb as the white dwarf rotates and is viewed at large angles to the field ($\theta \approx 80^\circ - 90^\circ$) over a narrow phase interval (cf. VV Puppis; Cropper and Warner 1986, Wickramasinghe and Meggitt 1982).

We have constructed a simplified point-source model for Grus V1 to illustrate the main characteristics. A possible viewing geometry consistent with the above picture is depicted in Figure 7.4 and is specified by the following parameters: orbital inclination $i = 40^\circ$, colatitude of the blue region $\Delta_b = 40^\circ$, and colatitude of the red region $\Delta_r = 125^\circ$. The blue and red regions share the same longitudinal great circle and are separated by 85° . We emphasize that there are other combinations of i , Δ_b , and Δ_r which can also satisfy the basic geometric constraints discussed earlier. At the same time however, it is clear that the two emission regions cannot be diametrically opposed, or else there would be no overlap in their visibility between $\phi \approx 0.4 - 0.6$. The overlap is especially evident in the R and I bands of Figure 7.3.

The radiation properties of the blue and red regions depicted in Figure 7.4 have been computed assuming point source models following Wickramasinghe and Meggitt (1985). The parameters for the two regions are as follows:

$$T_e = 20 \text{ keV}, \quad \Lambda = 1 \times 10^5, \quad B = 2 \times 10^7 \text{ G (blue region)}$$

and

$$T_e = 10 \text{ keV}, \quad \Lambda = 5 \times 10^6, \quad B = 2 \times 10^7 \text{ G (red region)}.$$

Here T_e is the electron temperature, Λ is the path length (opacity) parameter, and B is the magnetic field (assumed to be radial). We note that different electron temperatures for the two regions might arise as a consequence of unequal accretion rates. Figure 7.5 shows the resulting intensity and polarization curves averaged over the B and R bands. The two light curves are generally similar in appearance to the B and R data of Figure 7.3. Our preliminary model predicts a broad linear polarization pulse at $\phi = 0.0$ when the blue cyclotron region is viewed at $\theta \approx 80^\circ$, and two barely resolved pulses at $\phi = 0.4$ and $\phi = 0.6$ corresponding to the appearance and disappearance of the red accretion funnel as the white dwarf rotates (*i.e.* at $\theta = 90^\circ$). The circular polarization shows a reversal in sign between $\phi \approx 0.4 - 0.6$ when

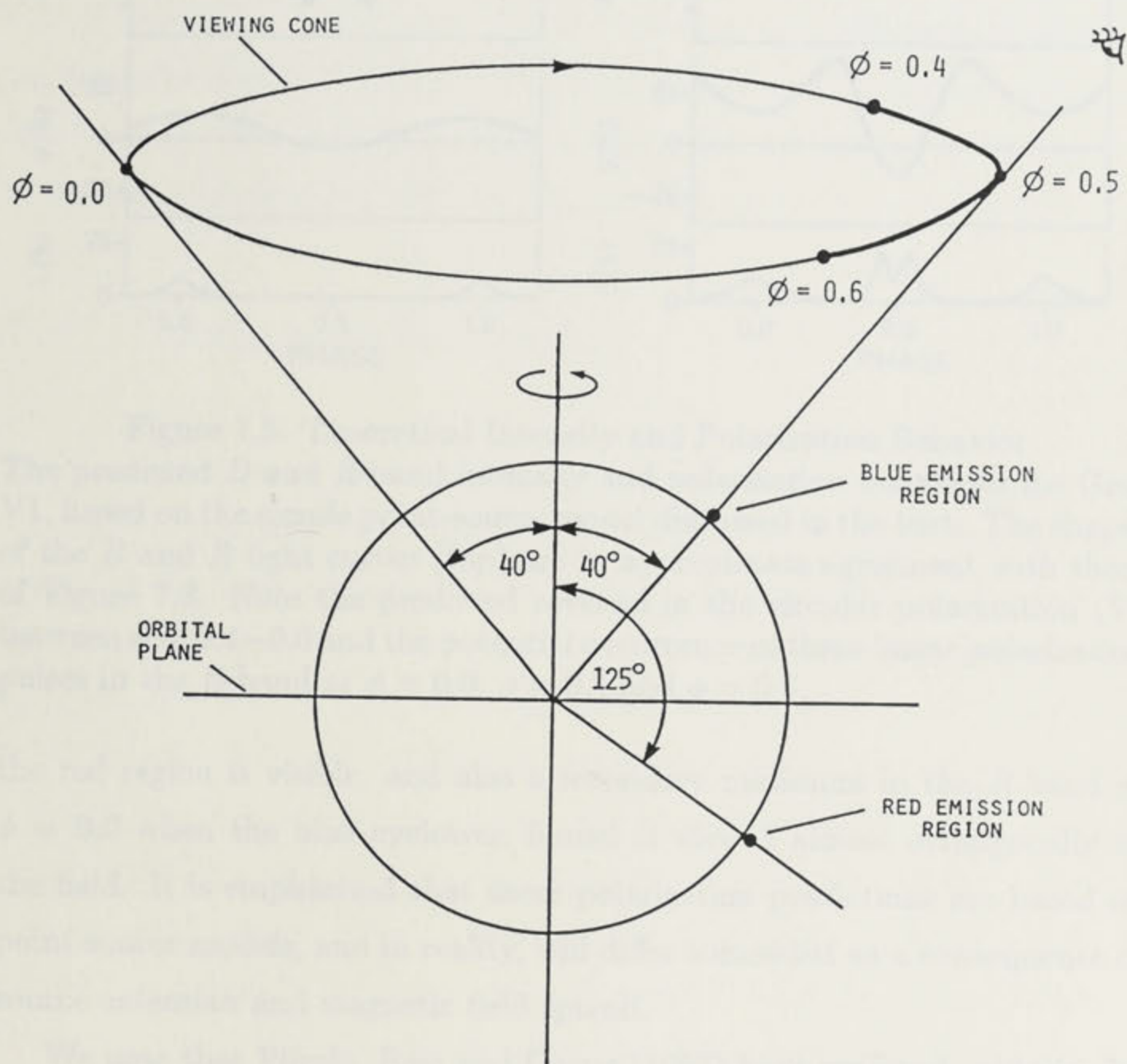


Figure 7.4: A Possible Geometry

A possible geometry for Grus V1, showing the location of the blue and red cyclotron emitting regions at colatitudes of 40° and 125° respectively. The viewing cone for an inclination angle of 40° is also depicted. Note that the blue region is never eclipsed and the viewing angle (θ) ranges between 0° – 80° , while the red region is only visible at viewing angles near 80° corresponding to $\phi \approx 0.4$ – 0.6 (the latter phase interval is indicated by the thickened section of the viewing cone).

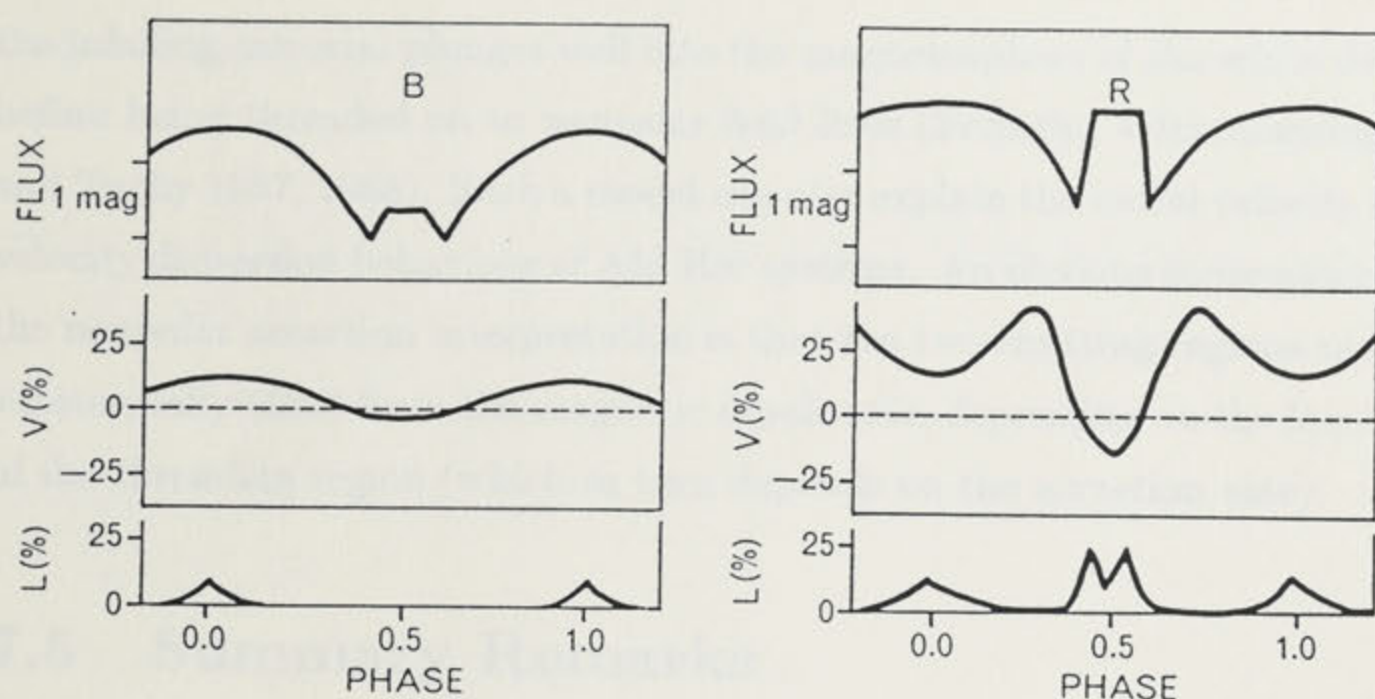


Figure 7.5: Theoretical Intensity and Polarization Behavior

The predicted *B* and *R*-band intensity and polarization behaviour for Grus V1, based on the simple point-source model discussed in the text. The shapes of the *B* and *R* light curves (top) are in approximate agreement with those of Figure 7.3. Note the predicted reversal in the circular polarization (*V*) between $\phi = 0.4-0.6$ and the potential occurrence of three linear polarization pulses in the *R*-band at $\phi = 0.0$, $\phi = 0.4$ and $\phi = 0.6$.

the red region is visible, and also a secondary minimum in the *R*-band at $\phi = 0.0$ when the blue cyclotron funnel is viewed almost orthogonally to the field. It is emphasized that these polarization predictions are based on point-source models, and in reality, will differ somewhat as a consequence of source extension and magnetic field spread.

We note that Pirola, Reiz and Coyne (1987) have reported evidence for two cyclotron emitting regions separated in latitude by $\approx 77^\circ$ in the AM Her system EF Eri. This separation angle is similar to that inferred in our model for Grus V1. In addition, Cropper (1987) can explain the light curve and polarization behaviour of BL Hyi in terms of emission from two accretion regions that are substantially less than 180° apart.

The occurrence of non-diametric cyclotron emitting regions in AM Her systems does not necessarily imply a complex magnetic field structure such as a quadrupole geometry. Instead we prefer an accretion model in which

the infalling material plunges well into the magnetosphere of the white dwarf before being threaded on to *nonpolar* field lines (Ferrario, Wickramasinghe, and Tuohy 1987, 1988). Such a model can also explain the radial velocity and velocity dispersion behaviour of AM Her systems. An obvious consequence of the nonpolar accretion interpretation is that the two emitting regions can be substantially offset from the magnetic dipole axis, depending on the location of the threading region (which in turn depends on the accretion rate).

7.5 Summary Remarks

To conclude, we have demonstrated from both observational and theoretical viewpoints that Grus V1 is most probably a new AM Herculis magnetic variable. It is the first to be selected on the basis of two-state optical variability, and is distinguished from other members of the class by showing convincing evidence for two cyclotron emitting regions which are not 180° apart and which are characterized by differing emission properties. We have developed a simple model that can account for the characteristics of the multicolour light curves and also predicts the polarization properties of the source as a function of binary phase. Circular and linear polarimetry to test these predictions is highly desirable, but will be difficult in view of the faintness of the system, even in the bright state (AAT polarimetry of the object was attempted in August 1987 but was impossible following a return to the faint state). Nevertheless, such measurements are needed to secure the AM Her classification, and to record the polarization behaviour with phase so that the emission geometry of the system can be refined.

We are grateful to the 2.3 metre telescope team and the ANU staff at Siding Spring Observatory for their excellent technical support. One of us (L.F.) acknowledges support from an ANU Postgraduate Research Scholarship.

7.6 References

- Bailey, J., Axon, D.J., Hough, J.H., Watts, D.J., Giles, A.B., and Greenhill, J.G. 1983 *M. N. R. A. S.*, **205**, 1P.
- Beuermann, K., Stella, L., and Patterson, J. 1987, *Ap. J.*, **316**, 360.
- Beuermann, K., Thomas, H.C., Giommi, P., and Tagliaferri, G. 1987, *Astr. Ap.*, **175**, L9.
- Bruch, A. 1984, *Astr. Ap. Suppl.*, **56**, 441.
- Cropper, M. 1987, *M. N. R. A. S.*, **228**, 389.
- Cropper, M., Menzies, J.W., and Tapia, S. 1986, *M. N. R. A. S.*, **218**, 201.
- Cropper, M., and Warner, B. 1986, *M. N. R. A. S.*, **220**, 633.
- Ferrario, L., Wickramasinghe, D.T., and Tuohy, I.R. 1987, *Proc. Astron. Soc. Aust.*, in press.
- Ferrario, L., Wickramasinghe, D.T., and Tuohy, I.R. 1988, *Ap. J.*, to be submitted
- Hawkins, M.R.S. 1981, *Nature*, **293**, 116.
- Hawkins, M.R.S. 1983, *Nature*, **301**, 688.
- Liebert, J., and Stockman, H.S. 1985, in *Cataclysmic Variables and Low-Mass X-ray Binaries*, Ed. D.Q. Lamb and J. Patterson, (Dordrecht: Reidel), p. 151.
- Morris, S.L., Schmidt, G.D., Liebert, J., Stocke, J., Gioia, I.M., and Maccacaro, T. 1987, *Ap. J.*, **314**, 641.
- Nugent, J.J. et al. 1983, *Ap. J. Suppl.* **51**, 1.
- Pirola, V., Reiz, A., and Coyne, G.V. 1987, *Astr. Ap.*, **186**, 120.
- Remillard, R.A., Bradt, H.V., McClintock, J.E., Patterson, J., Roberts, W., Schwartz, D.A., and Tapia, S. 1986, *Ap. J. (Letters)*, **302**, L11.

- Tuohy, I.R., Visvanathan, N., and Wickramasinghe, D.T. 1985, *Ap. J.*, **289**, 721.
- Tuohy, I.R., Buckley, D.A.H., Remillard, R.A., Bradt, H.V., and Schwartz, D.A. 1986, *Ap. J.*, **311**, 275.
- Vaiana G.S. et al. 1981, *Ap. J.*, **245**, 163.
- Watts, D. 1985, in *Recent Results on Cataclysmic Variables*, (ESA SP-236), p. 259.
- Wickramasinghe, D.T., and Ferrario, L. 1988, *Ap. J.*, **334**, 412.
- Wickramasinghe, D.T., and Meggitt, S. 1982, *M. N. R. A. S.*, **198**, 975.
- Wickramasinghe, D.T., and Meggitt, S. 1985, *M. N. R. A. S.*, **216**, 857.